

**Static, Dynamic, and Noise Characteristics of
Vertical-Cavity Surface-Emitting Lasers**

by

Joanne Y. Law

Submitted in Partial Fulfillment
of the
Requirements for the Degree
Doctor of Philosophy

Supervised by

Professor Govind P. Agrawal

The Institute of Optics
The College
School of Engineering and Applied Sciences

University of Rochester
Rochester, New York

1997

Curriculum Vitae

Joanne Y. Law was born in Hong Kong on 12th September, 1971. She received the B.S. degree in Engineering with distinction and honors from Brown University, Providence, Rhode Island in 1993, and the M.S.E.E. degree from Stanford University, Stanford, California in 1994. She was the recipient of the Faculty Scholar Award and the Roessler, Clark and Kornhauser Award at Brown University. She began her graduate studies at the University of Rochester in Fall 1994 and was awarded the Sproull Fellowship for two years. She pursued her research in vertical-cavity surface-emitting lasers under the supervision of Professor Govind P. Agrawal.

Publications

- J.Y. Law, G.P. Agrawal, and G.R. Gray, “Dynamic and noise characteristics of vertical-cavity surface-emitting lasers with phase-conjugate feedback,” Submitted to *Optics Communications*
- J.Y. Law and G.P. Agrawal, “Feedback-induced chaos and intensity-noise enhancement in vertical-cavity surface-emitting lasers,” *Journal of Optical Society B* (in press)
- J.Y. Law, G.H.M. van Tartwijk, and G.P. Agrawal, “Effects of transverse-mode competition on injection dynamics of vertical-cavity surface-emitting lasers,” *Quantum and Semiclassical Optics* (in press)
- J.Y. Law and G.P. Agrawal, “Optical feedback effects on vertical-cavity surface-emitting laser characteristics,” *Trends in Optics and Photonics Series: Advances in Vertical-Cavity Surface-Emitting Lasers* (in press)
- J.Y. Law and G.P. Agrawal, “Effects of optical feedback on static and dynamic characteristics of vertical-cavity surface-emitting lasers,” *Journal of Selected Topics in Quantum Electronics* **3**, 353-358 (1997)
- J.Y. Law and G.P. Agrawal, “Nonlinear spatio-temporal dynamics due to transverse-mode competition in gain-switched microcavity semiconductor lasers,” *Optics Communications* **138**, 95-98 (1997)
- J.Y. Law and G.P. Agrawal, “Mode-partition noise in vertical-cavity surface-emitting lasers,” *IEEE Photonics Technology Letters* **9**, 437-439 (1997)
- J.Y. Law and G.P. Agrawal, “Effects of spatial hole-burning on gain switching in vertical-cavity surface-emitting lasers,” *IEEE Journal of Quantum Electronics* **33**, 462-468 (1997)

Acknowledgments

I thank my advisor, Professor Govind Agrawal, for his guidance, his inspiration, and the many useful skills which he has taught me, including technical writing and critical thinking. His support and consideration during the tough times are especially appreciated.

I thank Professor Nabil Lawandy for first inspiring my interest in lasers in 1992. I am grateful to Professor Sumit Ghosh for his advice and encouragement regarding graduate studies. I thank Professor Carlos Stroud for his help in my re-application to the Institute in May 1994.

Among my colleagues, I thank in particular John Marciante for his generous help from macroscopic to microscopic matters. He has also patiently answered many questions which I raised. I thank Guido van Tartwijk for sharing his knowledge in his field of expertise with me. His sense of humor as well as his serious attitude towards his work have been inspiring at times. I thank my officemate Seungbum Woo for coming to my first two public talks. He has also been a sincere and supportive friend, whose company has provided a lot of fun.

Outside the Institute, I thank Daniel Tan for his loyal support, encouragement, and patience. He has been a constant source of momentum, and he is also my consultant on UNIX and windows, computer software, interview skills, and many other matters.

Most importantly, I thank my family for their care and support throughout the years. I thank my father for being my consistent and persistent sponsor from Brown, Stanford, to Rochester, for buying me a lovely little Ford Escort, and for his special thanksgiving visit during my freshman year. I thank my mother for sharing her wisdom with me. Her encouragement, understanding and love will always be very much appreciated.

Abstract

An important aspect of vertical-cavity surface-emitting lasers (VCSELs) that needs to be improved is its stable operation in a single transverse mode. Due to relatively large dimensions of VCSELs ($\sim 10 \mu\text{m}$ radius), spatial hole-burning and carrier diffusion affect device performance significantly, especially because VCSELs often operate in several transverse modes at high injection currents. In this thesis, a comprehensive numerical study of such spatial effects on the static, dynamic, and noise characteristics of VCSELs is presented. The computer model includes the spatial dependences of both the optical field and the carrier density. Device characteristics are analyzed under different operating conditions, including continuous-wave (CW) operation, gain-switched operation, optical feedback, and optical injection. Both single-mode and two-mode operations are analyzed.

Under CW operation, transverse-mode competition induced by spatial hole-burning is found to affect the static and noise characteristics significantly. In particular, transverse-mode competition affects the mode-partition noise. Under single-mode gain-switched operation, it is shown that by using an appropriate electrical contact, spatial hole-burning can be avoided and shorter pulses can be obtained. Under two-mode gain-switched operation, transverse-mode competition gives rise to rich nonlinear dynamics. The effect of external influence has also been studied. It is found that optical feedback or optical injection can force a two-mode VCSEL to operate in a single transverse mode under appropriate conditions. However, distant feedback or injection outside the locking region can destabilize the CW operation and lead to interesting nonlinear dynamics. The feedback strength and the injection power at which oscillations occur depend critically on the strength of intermodal coupling. In general, results indicate that strong intermodal coupling reduces the sensitivity of the VCSEL towards external influence.

Experiments have been conducted on a VCSEL to investigate the multiple-transverse-mode emission characteristics. Results show that multimode operation leads to considerable degradation of device performance, such as the distortion of light-current curves of the orthogonally polarized components, degradation of spatial beam quality, broadening of the optical spectrum, and modification of the mode-partition noise. Optical feedback effects on VCSEL characteristics have also been explored, and it is found that feedback leads to quasi-periodic oscillations.

List of Figures

2.1	<i>Schematic of an index-guided VCSEL.</i>	12
2.2	<i>Radial intensity profiles for the three lowest-order transverse modes.</i>	14
3.1	<i>L-I characteristics for three different contacts.</i>	32
3.2	<i>Radial carrier-density profiles at two times above threshold.</i>	33
3.3	<i>L-I characteristics with negligible diffusion for three different contacts.</i>	34
3.4	<i>Radial carrier-density profiles at two times above threshold with negligible diffusion.</i>	35
3.5	<i>Noise characteristics under single-mode operation.</i>	38
3.6	<i>RIN characteristics under two-mode operation with a ring contact.</i>	40
3.7	<i>RIN characteristics under two-mode operation with a 4-μm-wide disc contact.</i>	41
3.8	<i>FNS under two-mode operation.</i>	43
4.1	<i>Pulse shapes and frequency-shift profiles of gain-switched pulses under single-mode operation.</i>	47
4.2	<i>Variations of pulse width and frequency shift with modulation index with and without diffusion effects.</i>	49
4.3	<i>Radial carrier-density profiles with and without diffusion effects.</i>	50
4.4	<i>Variation of pulse width and frequency shift with disc-contact radius.</i>	51
4.5	<i>Radial carrier-density profiles at the peak of the gain-switched pulse for several disc-contact radii.</i>	51
4.6	<i>Radial carrier-density profiles and spatial intensity distributions of the LP_{01} and LP_{11} modes.</i>	53
4.7	<i>Gain-switched pulse trains at modulation frequencies of 2.5, 5 and 10 GHz under two-mode operation.</i>	54

4.8	<i>Bifurcation diagram as a function of modulation current for 10-GHz gain switching of a VCSEL operating in two modes.</i>	55
4.9	<i>Gain-switched pulse trains when the VCSEL operates in two modes under 10-GHz modulation.</i>	56
4.10	<i>Gain-switched pulse trains for three values of the nonlinear-gain parameter.</i>	57
5.1	<i>VCSEL in the presence of optical feedback.</i>	59
5.2	<i>Variations of mode power with the external-cavity length.</i>	62
5.3	<i>Variations of mode power with the external-mirror reflectivity.</i>	63
5.4	<i>Variations of mode power with the external-cavity length under out-of-phase condition.</i>	64
5.5	<i>Temporal evolution of the output power under single-mode operation for several feedback levels.</i>	66
5.6	<i>RIN spectra under single-mode operation.</i>	67
5.7	<i>Temporal evolution of the output power under two-mode operation with a 4-μm disc contact for several feedback values.</i>	69
5.8	<i>RIN spectra under two-mode operation with a 4-μm disc contact.</i>	70
5.9	<i>Temporal evolution of the output power under two-mode operation with a ring contact for several feedback levels.</i>	72
5.10	<i>RIN spectra under two-mode operation with a ring contact.</i>	73
5.11	<i>Bifurcation diagrams with respect to the feedback parameter F_{ext}.</i>	74
6.1	<i>Locking regime and stability boundaries in $(P_{inj}, \Delta\omega)$-space for an optically injected single-mode VCSEL.</i>	81
6.2	<i>Stable locking regions under injection conditions for single-mode and two-mode operations.</i>	83
6.3	<i>Change in quenching power with frequency detuning inside the stable locking region.</i>	84
6.4	<i>VCSEL dynamics in the non-locking region for a frequency detuning of -5 GHz.</i>	86
6.5	<i>VCSEL dynamics in the non-locking region for a frequency detuning of -3 GHz.</i>	87
6.6	<i>VCSEL dynamics in the unstable locking region.</i>	88
7.1	<i>Experimental setup for measuring VCSEL emission characteristics.</i>	90
7.2	<i>L-I characteristics.</i>	92

7.3	<i>Optical spectra for several values of the injection current.</i>	93
7.4	<i>Two-dimensional near-field profiles.</i>	94
7.5	<i>One-dimensional near-field profiles for several values of the injection current.</i>	95
7.6	<i>RIN spectra.</i>	96
7.7	<i>RIN spectra with optical feedback.</i>	98

List of Tables

2.1	<i>Device parameters used in simulations</i>	30
4.1	<i>Output pulse characteristics at different modulation frequencies.</i>	48
4.2	<i>Comparison of output pulse characteristics for the LP_{01} and LP_{11} modes under single-mode operation.</i>	52

Contents

Curriculum Vitae	ii
Publications	iii
Acknowledgments	iv
Abstract	v
List of Figures	vii
List of Tables	ix
1 Introduction	1
1.1 Historic Overview	1
1.2 VCSEL Characteristics	2
1.3 Goal of the Thesis	4
1.4 Outline of the Thesis	5
2 Rate-Equation Model	9
2.1 Maxwell's Equations	10
2.1.1 Laser-Cavity Modes	11
2.1.2 Gain and Loss in Laser Media	14
2.1.3 Semiconductor Laser Media	17
2.2 The Field Equation	19
2.3 The Carrier Rate Equation	23
2.4 Approximate Steady-State Characteristics	26
2.5 Computational Procedure	28
3 CW Operation	31
3.1 L-I Characteristics	31

3.1.1	Contact Geometry	31
3.1.2	Carrier Diffusion	34
3.2	Noise Characteristics	35
4	Gain Switching	45
4.1	Ultrashort Pulse Generation	45
4.1.1	Pulse Shape and Width	46
4.1.2	Contact Geometry	48
4.2	Nonlinear Dynamics	53
5	Optical Feedback Effects	59
5.1	Rate Equations with Optical Feedback	60
5.2	Short External Cavity	61
5.3	Long External Cavity	65
5.3.1	Single-Mode Operation	66
5.3.2	Two-Mode Operation	69
6	Optical Injection	77
6.1	Rate Equations with Optical Injection	78
6.2	Spatially Independent Single-Mode Model	78
6.3	Numerical Results	81
6.3.1	Stable Locking Region	82
6.3.2	Non-locking Region	85
6.3.3	Unstable Locking Region	87
7	Experimental Results	89
7.1	Experimental Setup	89
7.2	CW Operation without Feedback	91
7.2.1	L-I Characteristics	91
7.2.2	Spectral Characteristics	91
7.2.3	Near-Field Characteristics	93
7.2.4	RIN Characteristics	96

<i>CONTENTS</i>	xv
7.3 Effects of Optical Feedback	97
8 Summary	101
References	103

Chapter 1

Introduction

The vertical-cavity surface-emitting laser (VCSEL) has emerged rapidly as a new class of semiconductor lasers in recent years because of several advantages associated with its vertical-cavity geometry. As the name implies, a VCSEL is a microcavity laser with distributed Bragg reflectors on each side of a thin active region ($< 1 \mu\text{m}$) such that it emits light in a direction normal to the wafer surface. The direction of laser emission is orthogonal to that of conventional edge-emitting lasers, which emit light in the plane of the wafer surface. Currently, the most promising VCSEL structure employs an active region consisting of multiple quantum wells sandwiched between two epitaxially grown distributed Bragg reflectors. These reflectors are made up of 20–40 alternating quarter-wave layers of semiconductors with different compositions (typically $\text{Al}_x\text{Ga}_{1-x}\text{As}$). The difference in refractive indices between alternating layers results in reflectivities of larger than 99%. Such high reflectivities are required because of the thinness of the active layer ($\sim 10\text{--}100 \text{ nm}$) and a microscopic cavity length ($\sim 1 \mu\text{m}$). Layers of one mirror are p-doped while those of the other one are n-doped to allow injection of electric current through these Bragg reflectors by means of a metallic contact.

1.1 Historic Overview

VCSELs were first pursued in 1979 by Soda *et al.* of TIT in Japan. They employed a double heterostructure design with a GaInAsP active region and used metallic mirrors [1]. The device lased at $1.8 \mu\text{m}$ under pulsed operation at 77 K with a high threshold. Epitaxially grown mirrors were first used in 1983 but a thick active region was employed because of a low mirror reflectivity, which still resulted in relatively high thresholds. Advances in epitaxial technologies, in particular the development of semiconductor Bragg reflectors with extremely high reflectivities (~ 0.999) and the improvement in the control of thick-

ness and composition of epitaxial layers, led to the first demonstration of continuous-wave (CW), room-temperature operation of a low-threshold VCSEL with a single-quantum-well active region in 1989 [2]. Since then, rapid progress has been made in threshold reduction, two-dimensional-array fabrication [3], and the increase of output power [4] as well as efficiency [5]. Further improvements in the laser structure were made with the use of ion implants [6] and natural oxide [7],[8] to achieve small active regions ($< 5 \mu\text{m}$ radius). These improvements led to significant threshold reduction as well as better transverse-mode control. In addition, the range of operating wavelengths has been extended. While the most efficient VCSELs are being fabricated in the AlGaAs/GaAs and the InGaAs/GaAs material systems with emission in the $0.8\text{--}1 \mu\text{m}$ wavelength range, VCSELs with emission in the visible region ($\sim 0.7 \mu\text{m}$) [9] and the long-wavelength region ($1.3\text{--}1.6 \mu\text{m}$) [10], [11] have been recently fabricated.

1.2 VCSEL Characteristics

Due to their vertical-cavity geometry, VCSELs offer a number of significant advantages over edge-emitting lasers [12]. Since VCSELs have a relatively small active volume, very low threshold currents are attainable (μA range). Because of the symmetry in the wafer plane, the laser output is in the form of a narrow, low-divergence, circular beam, permitting high coupling efficiency to optical fibers with relaxed alignment tolerances, as well as easy focusing into a tight spot for optical storage applications. Furthermore, due to a microscopic cavity length, VCSELs inherently operate in a single longitudinal mode, and are thus suitable for high-bit-rate, fiber-optic data communications. Above all, VCSELs allow for a high packing density in the form of two-dimensional arrays and cost-effective fabrication and testing on a wafer level. Thus, VCSELs demonstrate the potential of being a low-cost, easily packaged, compact light source for use in high-volume applications related to optical communications, data storage, and optical interconnects.

Experimental studies have shown that VCSELs are practical in terms of other important device characteristics. Relative-intensity noise levels of -140 dB/Hz and -120 dB/Hz have been obtained under single-mode operation [13],[14] and multiple-transverse-mode operation with modulation [15], and such noise levels are low enough for most practical applications. However, similar to multiple-longitudinal-mode edge-emitters, mode-partition noise is present under multiple-transverse-mode operation [16]. Promising results including a small-signal bandwidth of 8 GHz [17] and an ultra-high relaxation-oscillation frequency of 71 GHz [18] indicate that VCSELs have the potential to operate at very high modulation speeds,

and 10-Gb/s operation of VCSELs has been demonstrated [19]. One application of high-speed modulation is the generation of short optical pulses of picosecond duration through gain-switching [20]–[22]. Optically gain-switched pulses of 4-ps duration [20] and electrically gain-switched pulses of duration below 25 ps [21] with a very low timing jitter (~ 100 fs) have been reported [22]. VCSEL performance under injection conditions has also been investigated, since it is well known that optical injection may improve the performance of semiconductor lasers including noise reduction and linewidth narrowing [23]. Experimental studies of optically injected VCSELs have demonstrated locking ranges as large as 80 GHz [24]. Outside the locking region, VCSELs exhibit rich nonlinear dynamics, such as four-wave mixing under single-mode operation [24] and polarization bistability under two-mode operation [25].

However, VCSELs also present a number of problems. These include multiple-transverse-mode operation, resistance heating, and uncontrollable polarization characteristics. Because of relatively large transverse dimensions of these devices (~ 10 μm radius), VCSELs typically operate in several transverse modes [26]–[28] especially at high injection currents because of spatial hole-burning [29],[30]. Numerical studies have shown that spatial hole-burning and multimode operation significantly affect the steady-state behavior [31],[32] and the turn-on transients [33] under solitary operation, and experimental studies support these predictions [34]–[36]. Several measures have been proposed to improve the transverse-mode control. These include (i) the use of native oxide to achieve very small active regions [7], (ii) the use of spatial filtering [36], (iii) the use of passive anti-guide regions surrounding the active region [37], (iv) the control of the gain-guided aperture size [38], and (v) the use of gain offset [39],[40]. Another concern is that resistance attributed to doped distributed Bragg reflectors is relatively high, resulting in heating and performance deterioration. By introducing large dopant concentrations near the interfaces of different semiconductor materials forming the distributed Bragg reflectors, the resistance can be reduced considerably [41]. Further, the polarization characteristics are found to be device dependent because of symmetry in the wafer plane. The fundamental mode is generally linearly polarized, but its polarization direction often varies with the injection current, and from one device to the other [26]. Various ways to control the polarization characteristics involve breaking the symmetry in the wafer plane, such as the use of intentional stress [42], anisotropic optical properties [43], or intentional gain anisotropy [44].

The issue of unintentional optical feedback is also extremely important. When light is focused onto an optical fiber or an optical disk, some light is invariably reflected back into the laser. It is well known that edge-emitting lasers are extremely sensitive to external optical feedback due to their low facet re-

flectivities, high gain, and the amplitude-phase-coupling effects in semiconductor materials. Despite the very high mirror reflectivities of VCSELs, experimental investigations and numerical simulations suggest that VCSELs are as sensitive to optical feedback as conventional edge-emitting lasers [45],[46] because of their high gain and short cavity length. Several aspects of the feedback problem have been addressed. Linewidth narrowing and broadening [47], coherence collapse, threshold change [48]-[50], mode-locking [51], and intensity-noise degradation [52] have been observed depending on the strength and phase of feedback.

1.3 Goal of the Thesis

Despite the large amount of experimental work devoted towards the development of VCSELs, their performance has not been completely understood. Several models capable of describing the operation characteristics of VCSELs have been discussed in the literature. Previous models typically neglect transverse variations and assume single-mode operation, so that their studies offer little insight to the important problem of multiple-transverse-mode operation as well as spatial hole-burning [45],[46],[53]. A number of new models which attempt a more comprehensive approach have been reported. Among the most comprehensive ones are the models proposed by Hadley *et al* [54] and Thode *et al* [55], which include fully time-dependent three-dimensional optical, carrier, and heat-transport effects. However, these relatively complicated models generally require tremendous computer resources, and so far their studies are limited to steady-state or CW operation. Several simpler models which describe the performance of index-guided VCSELs have proved quite useful [33],[56],[57]. These models assume that the spatial distribution of the optical field is governed by the time-independent index-guided modes supported by the passive laser cavity. Using these models, studies have been extended to treat different aspects of device behavior, such as the turn-on transients [33], VCSEL dynamics [56], and the modulation response [57].

The goal of this thesis is to provide a detailed numerical study of the multiple-transverse-mode characteristics of VCSELs while including the important spatial effects such as carrier diffusion and spatial hole-burning. Possible ways of improving stable single-transverse-mode operation through external control are also investigated. Because of the simplicity of our model, various operating conditions such as gain switching, optical injection, and optical feedback can be easily incorporated without stringent demand on computation time.

1.4 Outline of the Thesis

Chapter 2 describes the model employed to obtain the numerical results presented in subsequent chapters. We derive our model starting from Maxwell's equations and describe how transverse effects are included in the formulation, and we discuss the various assumptions used in our derivation. Our model consists of a field equation for each transverse mode and a carrier rate equation. The details of the computational procedure are also given.

Chapter 3 studies the simplest case of CW operation in the absence of external influence (solitary operation). We first investigate the steady-state characteristics without including spontaneous emission and study the effects of contact geometry and carrier diffusion. It is found that the steady-state multimode characteristics are significantly affected by spatial hole-burning. We also study the noise characteristics of VCSELs by including spontaneous emission. Mode-partition noise under two-mode operation is investigated, and we show that it depends strongly on the strength of intermodal coupling.

Chapter 4 considers the gain-switching operation of VCSELs, a common technique used to generate short pulses from semiconductor lasers. Under single-mode operation, we study the output pulse characteristics and show that spatial hole-burning places a limit on the minimum achievable pulse width. We also consider the case in which the laser operates simultaneously in two transverse modes and show that transverse-mode competition induced by spatial hole-burning leads to period-doubling oscillations and other interesting nonlinear behaviors. The spatio-temporal nature of gain switching is explored over a wide range of modulation currents and frequencies.

Chapter 5 analyzes the effect of optical feedback on the static, dynamic, and noise characteristics of VCSELs. For a short external cavity ($\sim 30 \mu\text{m}$), simulations show that feedback does not destabilize the CW operation, and we investigate the possibility of suppressing a higher-order transverse mode with feedback. For a relatively long external cavity ($\sim 1 \text{ cm}$), it is found that feedback can destabilize the CW operation, and we investigate the changes in nonlinear dynamics and the relative-intensity noise with feedback. The effect of intermodal coupling on feedback characteristics is also examined.

Chapter 6 considers the effects of optical injection, and VCSEL characteristics are explored over a wide range of frequency detunings and injection powers. It is found that strong intermodal coupling can reduce the sensitivity of VCSELs towards external injection in terms of both static (locking) and dynamic (non-locking) behaviors. Inside the locking region, we investigate the possibility of complete suppression

of a higher-order transverse mode by injecting the external field into the fundamental mode only. Outside the locking region, we explore the injection dynamics.

Chapter 7 discusses the results of several experiments performed on a VCSEL. We find that multiple-transverse-mode operation significantly affects several aspects of device performance, including static, spatial, spectral, and noise characteristics. Optical feedback effects on such characteristics are also investigated, and we find that optical feedback leads to quasi-periodic oscillations and a change in the relative-intensity-noise spectrum.

Chapter 8 summarizes the main results of this thesis and should be useful for a quick review of the research results.

Chapter 2

Rate-Equation Model

In this chapter we develop a theoretical model capable of predicting the static, dynamic, and noise characteristics of a VCSEL. In Section 2.1 we derive the wave equation governing the propagation of light in a semiconductor medium, and we obtain the spatial modes by solving the time-independent wave equation subject to boundary conditions imposed by a particular VCSEL structure. Since the dynamics of a semiconductor laser is adequately described by two variables, namely the complex amplitude of the optical field and the number of electron-hole pairs (or carriers) in the active region, the major components of our model include two coupled rate equations for the optical field and the carrier density. In Section 2.2 we derive the field equation describing wave propagation in a semiconductor laser starting from the wave equation obtained in Section 2.1. In Section 2.3 we present the carrier rate equation and discuss the physical origin of various terms. Our complete model incorporates the spatial and temporal dependences of both the carrier density and the optical field. In Section 2.4 we present an approximate steady-state solution obtained from spatially independent single-mode rate equations. Section 2.5 gives details of the computational procedure used to numerically integrate the field and carrier rate equations, as well as the parameter values used in our simulations.

2.1 Maxwell's Equations

Since all optical phenomena is governed by Maxwell's equations, we start our discussions by considering these equations, which in the MKS system of units are given by [58]

$$\nabla \times \mathcal{E} = -\frac{\partial \mathcal{B}}{\partial t}, \quad (2.1)$$

$$\nabla \times \mathcal{H} = \mathcal{J} + \frac{\partial \mathcal{D}}{\partial t}, \quad (2.2)$$

$$\nabla \cdot \mathcal{D} = \rho_f, \quad (2.3)$$

$$\nabla \cdot \mathcal{B} = 0, \quad (2.4)$$

where the current-density vector \mathcal{J} and the charge density ρ_f represent the sources for the electromagnetic field. \mathcal{E} and \mathcal{H} are the electric and magnetic field vectors, respectively, and \mathcal{D} and \mathcal{B} are the corresponding electric and magnetic flux densities. The fields \mathcal{D} and \mathcal{B} arise in response to the electric and magnetic fields \mathcal{E} and \mathcal{H} . For a non-magnetic dielectric medium, their relationship can be expressed in terms of the constitutive relations

$$\mathcal{D} = \epsilon_0 \mathcal{E} + \mathcal{P}, \quad (2.5)$$

$$\mathcal{B} = \mu_0 \mathcal{H}, \quad (2.6)$$

where ϵ_0 is the vacuum permittivity, μ_0 is the vacuum permeability, and \mathcal{P} is the induced electric polarization vector.

Using Maxwell's equations (2.1)–(2.4) together with the constitutive relations (2.5) and (2.6), we obtain the fundamental electromagnetic wave equation that describes the propagation of optical fields inside a dielectric medium:

$$\nabla^2 \mathcal{E} - \frac{1}{c^2} \frac{\partial^2 \mathcal{E}}{\partial t^2} = \frac{1}{\epsilon_0 c^2} \frac{\partial^2 \mathcal{P}}{\partial t^2} + \nabla(\nabla \cdot \mathcal{E}). \quad (2.7)$$

In the absence of free currents ($\mathcal{J} = 0$) and free charges ($\rho_f = 0$), $\nabla \cdot \mathcal{D} = 0$. Since the $\nabla \cdot \mathcal{P}$ term is negligible in most cases of practical interest [59], the $\nabla(\nabla \cdot \mathcal{E})$ term in Eq. (2.7) can often be neglected, and Eq. (2.7) becomes

$$\nabla^2 \mathcal{E} - \frac{1}{c^2} \frac{\partial^2 \mathcal{E}}{\partial t^2} = \frac{1}{\epsilon_0 c^2} \frac{\partial^2 \mathcal{P}}{\partial t^2}. \quad (2.8)$$

Since any time-dependent field can be decomposed into its Fourier components, we consider a single-frequency component and write it in cylindrical coordinates as

$$\mathcal{E}(r, \phi, z, t) = \frac{1}{2} \mathbf{E}(r, \phi, z, \omega) \exp(-i\omega t) + c.c., \quad (2.9)$$

$$\mathcal{P}(r, \phi, z, t) = \frac{1}{2} \mathbf{P}(r, \phi, z, \omega) \exp(-i\omega t) + c.c., \quad (2.10)$$

where ω is the angular frequency. The wave equation then becomes

$$\nabla^2 \mathbf{E} + k^2 \mathbf{E} = \frac{\omega^2}{\epsilon_0 c^2} \mathbf{P}, \quad (2.11)$$

where $k = \omega/c = 2\pi/\lambda$ is the vacuum wave number at the wavelength λ . Under steady-state conditions, the response of the medium to the electric field is governed by the susceptibility χ defined by

$$\mathbf{P} = \epsilon_0 \chi(\omega) \mathbf{E}. \quad (2.12)$$

In general χ is a second-rank tensor. For an isotropic medium χ is a scalar [58], a reasonable assumption for a VCSEL. In a passive semiconductor medium, the complex susceptibility can be written as

$$\chi(\omega) = \chi_0(\omega) = \chi_0' + i\chi_0'', \quad (2.13)$$

where the subscript 0 is used to denote the background susceptibility of the material. The time-independent wave equation (2.11) can then be written as

$$\nabla^2 \mathbf{E} + \epsilon(\omega)k^2 \mathbf{E} = 0, \quad (2.14)$$

which is known as the Helmholtz equation, and where $\epsilon(\omega)$ is the complex dielectric constant given by

$$\epsilon = \epsilon_b + i\chi_0'', \quad (2.15)$$

where $\epsilon_b(\omega) = 1 + \chi_0'$ is the background dielectric constant of the unpumped medium, and the term χ_0'' accounts for background material absorption.

2.1.1 Laser-Cavity Modes

The modes of the passive laser cavity are the solutions of the Helmholtz equation (2.14) with ϵ given by Eq. (2.15). An understanding of the field distribution of the modes is especially important for multimode control in VCSELs, since the laser cavity supports several transverse modes because of relatively large

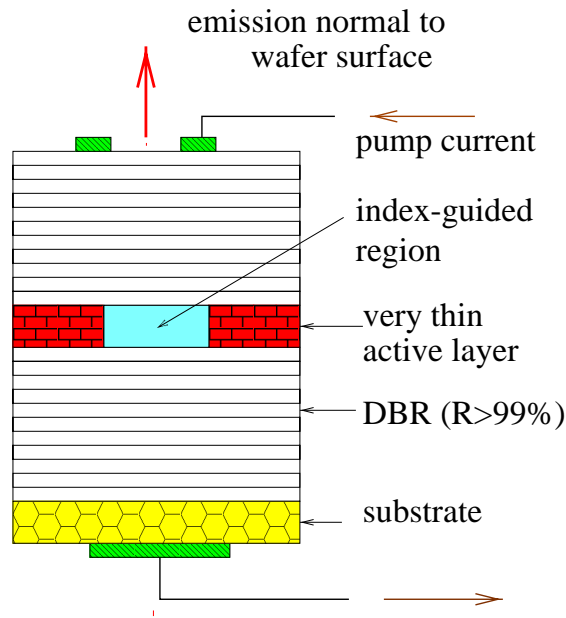


Figure 2.1: Schematic of an index-guided VCSEL.

transverse dimensions compared with the wavelength λ . In this thesis we consider an index-guided VC-SEL in a cylindrical form, a longitudinal cross section of which is shown in Fig. 2.1. The laser cavity with length L is formed by two highly reflective mirrors in the longitudinal direction and an index-guided step in the radial direction. In such a structure, ϵ_b is a real function of r only, given by

$$\epsilon_b(r) = \begin{cases} \epsilon_1 & \text{for } r \leq a \\ \epsilon_2 & \text{for } r > a \end{cases} \quad (2.16)$$

Here a is the radius of the index-guided region, and ϵ_1 and ϵ_2 are the dielectric constants inside and outside the index-guided region.

To obtain the spatial modes, we assume the Fourier component of the field in Eq. (2.9) to be of the form

$$\mathbf{E}(r, \phi, z, \omega) = \hat{\mathbf{e}}\psi(r, \phi)F(z), \quad (2.17)$$

where $\hat{\mathbf{e}}$ is the polarization unit vector. Substituting Eq. (2.17) into the Helmholtz equation (2.14) and using $\epsilon \approx \epsilon_b$ (since $\chi_0'' \ll \epsilon_b$), we obtain

$$\frac{1}{\psi(r, \phi)} \left\{ \nabla_T^2 \psi(r, \phi) + \epsilon_b \frac{\omega^2}{c^2} \psi(r, \phi) \right\} + \frac{1}{F(z)} \left\{ \frac{d^2 F(z)}{dz^2} \right\} = 0, \quad (2.18)$$

where ∇_T^2 represents the transverse Laplacian, and ϵ_b is given by Eq. (2.16). Since the first part involves only the transverse variations in r and ϕ , and the second part only the longitudinal variation in z , they can be individually equated to a constant such that their sum is zero. The resulting equations can be written as

$$\frac{d^2 F(z)}{dz^2} + \beta^2 F(z) = 0, \quad (2.19)$$

$$\nabla_T^2 \psi(r, \phi) + \left(\epsilon_b \frac{\omega^2}{c^2} - \beta^2 \right) \psi(r, \phi) = 0, \quad (2.20)$$

where β is a constant to be determined. The general solution of Eq. (2.19) is

$$F(z) = A \sin(\beta z) + B \cos(\beta z), \quad (2.21)$$

where A and B are integration constants. Imposing the boundary conditions $F(0) = 0$ and $F(L) = 0$ corresponding to high-reflectivity mirrors at the two ends of the laser cavity, we obtain the longitudinal modes given by

$$F(z) = A \sin(\beta z), \quad (2.22)$$

where the wave number β can take on any of the values

$$\beta = \beta_q = q\pi/L, \quad (2.23)$$

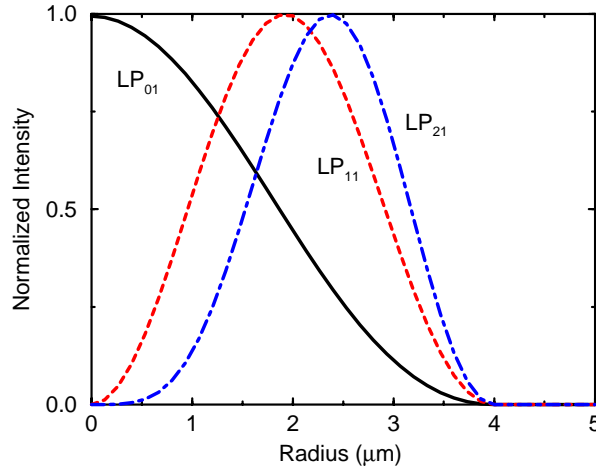


Figure 2.2: Radial intensity profiles for the three lowest-order transverse modes. Solid, dotted and dashed lines correspond to the LP_{01} , LP_{11} , and LP_{21} transverse modes, respectively.

and q is an integer. Each mode (with label q) is characterized by a distinct wave number β_q and is referred to as a longitudinal mode. Using a plane-wave approximation ($\beta_q = 2\pi\bar{n}\nu_q/c$), the frequency of the q -th longitudinal mode is

$$\nu_q = q(c/2\bar{n}L), \quad (2.24)$$

where \bar{n} is the mode index for a given mode $\psi(r, \phi)$ and will be introduced later. Since VCSELs have a microscopic cavity length ($\sim 1 \mu\text{m}$), the separation between adjacent longitudinal modes $\Delta\nu = c/2\bar{n}L$ is so large ($\sim 40 \text{ THz}$) that only one longitudinal fits under the gain spectrum of a semiconductor laser medium, resulting in single-longitudinal-mode operation. In contrast, several modes reside under the gain spectrum for edge-emitters due to a relatively long cavity length ($\sim 100 \mu\text{m}$), leading to multiple-longitudinal-mode operation.

Using Eq. (2.16) for ϵ_b in Eq. (2.20), the solutions $\psi(r, \phi)$ are found to be the linearly polarized LP_{mn} modes, which are well known in the context of optical fibers [60]. The $\psi(r, \phi)$'s are known as transverse modes since they have different transverse spatial distributions. Due to waveguide dispersion, the operating frequencies of different transverse modes are slightly different, and can be obtained by solving the standard waveguide dispersion relation [60]. Typical frequency separation between two adjacent transverse modes is $\sim 100 \text{ GHz}$. For simplicity, we consider only the three lowest-order transverse modes in our analysis. Their radial intensity distributions are shown in Fig. 2.2.

2.1.2 Gain and Loss in Laser Media

The dielectric constant given by Eq. (2.15) is valid only inside an unpumped semiconductor medium. In this section we discuss how pumping or gain modifies the dielectric constant and develop a more complete description of the material response of a laser medium in terms of a complex refractive index. We also consider the additional loss mechanisms in a laser medium and introduce the appropriate absorption coefficients to account for their effects.

In the presence of pumping, χ in Eq. (2.12) can be decomposed into two parts as

$$\chi(\omega) = \chi_0(\omega) + \chi_p(\omega), \quad (2.25)$$

where χ_0 given by Eq. (2.13) is the medium susceptibility in the absence of external pumping, and $\chi_p = \chi_p' + i\chi_p''$ is the additional contribution caused by external pumping. The complex dielectric function $\epsilon(\omega)$ in the Helmholtz equation (2.14) then becomes

$$\epsilon = \epsilon_b + \chi_p' + i(\chi_p'' + \chi_0''). \quad (2.26)$$

To account for the effects of various loss mechanisms present in a laser medium such as output coupling and internal losses, we consider light propagation in a semiconductor laser. Instead of using the complex dielectric constant given by Eq. (2.26), we describe the propagation characteristics in terms of two optical constants, the index of refraction n and the absorption coefficient α_{abs} . Assuming that pumping does not affect the transverse modes of the VCSEL cavity and noting that $F(z)$ in Eq. (2.22) represents a standing wave, we write $F(z)$ as a superposition of forward and backward waves whose propagation constant is modified by pumping. For the forward propagating wave,

$$F_f = F_0 \exp(i\tilde{\beta}z), \quad (2.27)$$

where F_0 is the constant amplitude. The complex propagation constant $\tilde{\beta}$ is determined from $\tilde{\beta}^2 = \epsilon\omega^2/c^2$ and is given by

$$\tilde{\beta} = k\sqrt{\epsilon} = k\tilde{n}, \quad (2.28)$$

where \tilde{n} is the complex index of refraction given by

$$\tilde{n} = n + i\frac{\alpha_{abs}}{2k}, \quad (2.29)$$

where n is the refractive index of the medium, and α_{abs} is the power-absorption coefficient accounting for material absorption and pumping only. In semiconductors, usually $\alpha_{abs} \ll nk$. Using Eq. (2.26) for ϵ

and Eq. (2.29) for \tilde{n} , we equate the real and imaginary parts of $\epsilon = \tilde{n}^2$ and obtain

$$n = \sqrt{\epsilon_b + \chi_p'}, \quad (2.30)$$

$$\alpha_{abs} = \frac{k}{n} (\chi_0'' + \chi_p''). \quad (2.31)$$

These equations explicitly show how n and α_{abs} are affected by the external pumping of the semiconductor medium through χ_p . Generally, $\chi_p' \ll \epsilon_b$, and Eq. (2.30) can be approximated by

$$n \approx n_b + \Delta n_p = n_b + \frac{\chi_p'}{2n_b}, \quad (2.32)$$

where $n_b = \sqrt{\epsilon_b}$ is the background refractive index of the unpumped material, and Δn_p is the amount by which it changes in the presence of pumping. Even though the change in the refractive index is often less than 1%, it significantly affects the characteristics of a semiconductor laser [59].

External pumping also reduces the absorption coefficient through χ_p'' as seen in Eq. (2.31). The term χ_0'' accounts for the unpumped material absorption. If χ_p'' is negative and its magnitude exceeds χ_0'' , α_{abs} can be negative. It is common to introduce the material gain as

$$g = -\frac{k}{n} (\chi_0'' + \chi_p'') = -\alpha_{abs}. \quad (2.33)$$

When external pumping compensates for the material loss so that $g = \alpha_{abs} = 0$, the medium is said to be transparent. However, for lasing action to occur, the losses at the mirrors occurring on each round trip have to be overcome. To obtain the threshold condition, we require that the optical field [Eq. (2.27)] reproduces itself every round trip under CW operating conditions. If R_1 and R_2 are the facet reflectivities at the two ends and L is the length of the laser cavity, the net change in the amplitude after one round trip is unity at laser threshold, i.e.

$$\sqrt{R_1 R_2} \exp(2i\tilde{\beta}L) \exp(-\alpha_{int}L) = 1. \quad (2.34)$$

An additional term $\exp(-\alpha_{int}L)$ is introduced phenomenologically to account for internal losses due to various mechanisms, such as free-carrier absorption and scattering at the interfaces, and α_{int} is the associated power-absorption coefficient. Equating the magnitude of the two sides of Eq. (2.34) and using Eqs. (2.28) and (2.29), we obtain

$$\sqrt{R_1 R_2} \exp\{-(\alpha_{abs} + \alpha_{int})L\} = 1. \quad (2.35)$$

Using $g = -\alpha_{abs}$ [Eq. (2.33)] in Eq. (2.35), we obtain the following threshold gain condition for lasing:

$$g = \alpha_m + \alpha_{int}, \quad (2.36)$$

where the distributed mirror loss α_m is defined as

$$\alpha_m = \frac{1}{2L} \ln \left(\frac{1}{R_1 R_2} \right). \quad (2.37)$$

The internal loss α_{int} and the mirror loss α_m will be introduced phenomenologically into the field equation later.

2.1.3 Semiconductor Laser Media

In semiclassical laser theory, the field is obtained using Maxwell's equations (classical approach), but the medium response is calculated using quantum mechanics. The medium response is governed by the polarization \mathcal{P} induced by the optical field \mathcal{E} and leads to the susceptibility χ_p defined in Eq. (2.12). To complete our formulation, it is necessary to specify how χ_p depends on external pumping [59]. Since a first-principle analysis for semiconductor lasers is extremely complex, a phenomenological approach is generally used for describing a semiconductor laser and has proved to be extremely successful [61]. It is based on the empirical observation that the gain varies almost linearly with the injected carrier density N in a semiconductor material, and the material gain g can be approximated as [59]

$$g(N) = a_0(N - N_T), \quad (2.38)$$

where $a_0 = (\partial g / \partial N)_{N=N_T}$ is the gain coefficient, and N_T is the carrier density at transparency [$g(N_T) = 0$]. Note that $a_0 N_T$ accounts for material absorption and is related to χ_0'' in Eq. (2.33). Since the carriers usually spread beyond the region where the optical mode is confined, the optical mode sees only part of the material gain. Confinement factors are usually used to account for this difference. Rather than explicitly introducing a confinement factor at this point, we choose to work with a spatially dependent gain $g(r, \phi, z)$ and a spatially dependent field, and we will see that the appropriate confinement factor will appear naturally in the course of our derivation.

To complete the phenomenological description, the refractive index is also assumed to vary linearly with the carrier density, i.e. Δn_p in Eq. (2.32) can be written as

$$\Delta n_p = b_0 N, \quad (2.39)$$

where $b_0 = (\partial n / \partial N)_{N=N_T}$. Comparing Eqs. (2.38) and (2.39) with Eqs. (2.32) and (2.33), we obtain an explicit expression for χ_p which is linearly dependent on N :

$$\chi_p(N) = 2n_b \left(b_0 - i \frac{a_0}{2k} \right) N. \quad (2.40)$$

A very important and useful parameter is the ratio of the real and imaginary parts of χ_p and is given by

$$\alpha = \frac{\chi_p'}{\chi_p''} = -2k \frac{b_0}{a_0} = -2k \left(\frac{\partial n / \partial N}{\partial g / \partial N} \right)_{N=N_T}. \quad (2.41)$$

Because $b_0 < 0$ in a semiconductor, α is a positive dimensionless number. It is commonly referred to as the linewidth-enhancement factor or the α -parameter [59], and it relates the change in refractive index to the change in gain induced by pumping.

Summarizing our results so far, the complex refractive index and the dielectric susceptibility in a semiconductor laser medium can be written as

$$\tilde{n} = n_b + \Delta\tilde{n}, \quad (2.42)$$

$$\epsilon \approx n_b^2 + 2n_b\Delta\tilde{n}, \quad (2.43)$$

where $\Delta\tilde{n}$ is given by

$$\Delta\tilde{n} = \Delta n_p - i \frac{g}{2k}, \quad (2.44)$$

where g and Δn_p are given by Eqs. (2.38) and (2.39), respectively. Note that $\Delta\tilde{n}$ is spatially dependent since it depends on the material gain $g(r, \phi, z)$. We will use ϵ in the form given by Eq. (2.43) together with Eq. (2.44) in the derivation of the field equation.

2.2 The Field Equation

Since the electromagnetic field inside the laser cavity satisfies Maxwell's equations, the starting point to obtain the field equation is the wave equation (2.8). In general, the dynamics of the semiconductor material should be taken into account to obtain the induced polarization \mathcal{P} . However, the material response governed by the intraband scattering processes is relatively fast (\sim fs) compared to other time scales of interest (such as the photon lifetime and the carrier recombination time) so that we can assume that Eq. (2.12) holds. It should be kept in mind that the use of Eq. (2.12) is justified only for a fast-responding semiconductor. In general, Eq. (2.8) should be used with the induced polarization given by calculations from quantum mechanics [59].

The following analysis is based on the separability of the spatial and temporal dependences of the electric field. Since carrier-induced changes in the refractive index are typically two orders of magnitude smaller than the built-in refractive index difference of ~ 0.1 responsible for index guiding ($\Delta n_p \ll n_b$), waveguiding properties of an index-guided VCSEL are not significantly affected by temporal changes

in the carrier density, and the spatial dependences of the optical field are given by the transverse mode $\psi(r, \phi)$ and longitudinal mode $F(z)$ derived in Section 2.1.1. For the simple case of single-transverse-mode operation, the electric field can be written as

$$\mathcal{E}(r, \phi, z, t) = \frac{1}{2} \hat{\mathbf{e}} U(r, \phi, z, t) \exp(-i\omega_0 t) + c.c., \quad (2.45)$$

where $\omega_0 = 2\pi\nu_{\hat{q}}$ is the resonant frequency corresponding to a longitudinal mode \hat{q} of the unpumped laser cavity, and $U(r, \phi, z, t)$ is given by

$$U(r, \phi, z, t) = E(t) \psi(r, \phi) A \sin(\beta z), \quad (2.46)$$

where A is a normalization constant, and $\beta = \hat{q}\pi/L$ is the wave number determined by the cavity-resonance condition (2.23). The complex field $E(t)$ accounts for both the amplitude and phase variations with time, and is assumed to be slowly varying compared with an optical-period time scale. Although we choose to work in the reference frame ω_0 , any other optical frequency can also be used in place of ω_0 in Eq. (2.45). $\psi(r, \phi)$ and $A \sin(\beta z)$ are normalized such that $|\mathcal{E}(r, \phi, z, t)|^2$ is the photon density and $|E(t)|^2$ is the photon number when used with the appropriate carrier rate equation presented in the next section. The appropriate normalization conditions are

$$\int_0^{2\pi} \int_0^R |\psi(r, \phi)|^2 r dr d\phi = 1, \quad (2.47)$$

$$\int_0^L |A \sin(\beta z)|^2 dz = 1, \quad (2.48)$$

where L is the length of the laser cavity, R is the radius of the device, and $A = \sqrt{2\beta/L}$. It follows from the above choices of normalization constants that

$$\int_0^L \int_0^{2\pi} \int_0^R |\mathcal{E}(r, \phi, z, t)|^2 r dr d\phi dz = |E(t)|^2. \quad (2.49)$$

To obtain the wave equation for the slowly-varying complex amplitude $E(t)$, it is more convenient to work in the Fourier domain. The Fourier transform $\tilde{U}(r, \phi, z, \omega - \omega_0)$, defined by

$$\tilde{U}(r, \phi, z, \omega - \omega_0) = \int_{-\infty}^{\infty} U(r, \phi, z, t) \exp[i(\omega - \omega_0)t] dt, \quad (2.50)$$

is found to satisfy the Helmholtz equation (2.14) with $k = \omega/c$ and ϵ given by Eq. (2.43). Using Eq. (2.46), the transform in Eq. (2.50) can be written as

$$\tilde{U}(r, \phi, z, \omega - \omega_0) = \tilde{E}(\omega - \omega_0) \psi(r, \phi) A \sin(\beta z). \quad (2.51)$$

Since $E(t)$ is slowly varying compared with an optical period, the response of the medium can be assumed to be nondispersive, i.e. $\chi_0(\omega) \approx \chi_0(\omega_0)$ and $\chi_p(\omega) \approx \chi_p(\omega_0)$ in Eq. (2.26). Substituting Eq. (2.51) into the Helmholtz equation (2.14) and using the relations $\epsilon(\omega) \approx \epsilon(\omega_0)$ and $\omega^2 \approx \omega_0^2 + 2\omega_0(\omega - \omega_0)$, we obtain

$$\left\{ \nabla_T^2 \psi + n_b^2 \frac{\omega_0^2}{c^2} \psi \right\} \tilde{E} A \sin(\beta z) + \left\{ n_b \frac{2\omega_0(\omega - \omega_0)}{c^2} + 2\Delta\tilde{n} \frac{\omega^2}{c^2} \right\} \tilde{E} \psi A \sin(\beta z) = 0, \quad (2.52)$$

where \tilde{E} denotes $\tilde{E}(\omega - \omega_0)$. Note that we have replaced ω by ω_0 in the second term since, since $\psi(r, \phi)$ is relatively unaffected by the small change in the refractive index. Although the term $\Delta\tilde{n}$ in Eq. (2.52) carries a temporal dependence through the term $g(t)$, it does not violate the nondispersive assumption, since $g(t)$ varies slowly compared with an optical period. Since $\psi(r, \phi)$ is a transverse mode of the laser cavity, the first group of terms enclosed by curly brackets in Eq. (2.52) is zero. To eliminate the spatial dependence, we multiply the second group of terms by $\psi^*(r, \phi) A \sin(\beta z)$ and integrate over the device dimensions. Substituting Eq. (2.44) for $\Delta\tilde{n}$, we obtain

$$-i(\omega - \omega_0)\tilde{E} = \frac{1}{2}(1 - i\alpha)G(t)\tilde{E} + i\frac{\omega_0}{\bar{n}}\Gamma_L b_0 \hat{N}_T \tilde{E}, \quad (2.53)$$

where $G(t)$ is the modal gain, \hat{N}_T is the carrier number at transparency, and \bar{n} is the mode index. It is given by

$$\bar{n} = \int_0^{2\pi} \int_0^R n_b(r, \phi) |\psi(r, \phi)|^2 r dr d\phi, \quad (2.54)$$

Assuming that the carrier density is uniform in the z direction (justified in the next section), the modal gain $G(t)$ in Eq. (2.53) is given by

$$G(t) = \Gamma_L v_g \int_0^{2\pi} \int_0^{R_a} g(r, \phi, t) |\psi(r, \phi)|^2 r dr d\phi, \quad (2.55)$$

where $v_g = c/\bar{n}$ is the group velocity, R_a is the radius of the active region, and $\psi(r, \phi)$ is assumed to be normalized according to Eq. (2.47). The material gain g is given by

$$g(r, \phi, t) = a_0 \{N(r, \phi, t) - N_T\}, \quad (2.56)$$

and Γ_L is the longitudinal confinement factor

$$\Gamma_L = \int_0^d |A \sin(\beta z)|^2 dz, \quad (2.57)$$

where d is the thickness of the active region, and $A \sin(\beta z)$ is assumed to be normalized according to Eq. (2.48). The integrals in Eqs. (2.55) and (2.57) account for the fact that the optical field sees gain only in the region where carriers are present.

The temporal dependence of the field $E_i(t)$ can be obtained by performing an inverse Fourier transform of Eq. (2.53). The result is

$$\frac{dE}{dt} = \frac{1}{2}[(1 - i\alpha)G(t) - \gamma]E + i\frac{\omega_0}{\tilde{n}}\Gamma_L b_0 \hat{N}_T E, \quad (2.58)$$

where the cavity loss is included phenomenologically by the cavity decay rate $\gamma = v_g(\alpha_m + \alpha_{int})$. Note that Eq. (2.58) is written for the field with the temporal part given by $\mathcal{E}(t) = E(t) \exp(-i\omega_0 t)$. As a consistency check, note that the imaginary part on the right side of Eq. (2.58) is zero when the medium is unpumped ($N = 0$), which means that $E(t)$ is real and the total field $\mathcal{E}(t)$ is indeed oscillating at the angular frequency ω_0 . It is often convenient to work in reference frames other than ω_0 . A constant frequency shift then shows up in Eq. (2.58) as a constant imaginary term. Of particular interest are the operation frequencies ω_T at transparency [$G(N_T) = 0$] and ω_{th} at threshold [$G(N_{th}) = \gamma$]. Using Eq. (2.58), we obtain expressions relating ω_0 , ω_T , and ω_{th} , which can be written as

$$\omega_T = \omega_0 - \Gamma_L b_0 \hat{N}_T \frac{\omega_0}{\tilde{n}}, \quad (2.59)$$

$$\omega_{th} = \omega_T + \frac{1}{2}\alpha\gamma. \quad (2.60)$$

We recall that $b_0 < 0$, and therefore $\omega_0 < \omega_T < \omega_{th}$. The linear relation between different operation frequencies follows directly from the assumption of a linear dependence of the complex refractive index $\tilde{n}(N)$ on the carrier density.

Writing the temporal part of the total field in the form $\mathcal{E}(t) = E(t) \exp(-i\omega_T t)$, the field equation is obtained by a simple linear transformation of Eq. (2.58). The result is

$$\frac{dE}{dt} = \frac{1}{2}[(1 - i\alpha)G(t) - \gamma]E. \quad (2.61)$$

For $\mathcal{E}(t) = E(t) \exp(-i\omega_{th} t)$, the field equation becomes

$$\frac{dE}{dt} = \frac{1}{2}(1 - i\alpha)[G(t) - \gamma]E \quad (2.62)$$

and is widely used in the literature. We will use the field equation in this form in the following chapters.

It is straightforward to generalize the above formalism for the single-mode case to the multimode case. Assuming that the VCSEL can operate in several transverse modes simultaneously, the total electric field can be expressed as

$$\mathcal{E}(r, \phi, z, t) = \frac{1}{2} \sum_{i=1}^p \hat{\mathbf{e}}_i E_i(t) \psi_i(r, \phi) A \sin(\beta z) \exp(-i\omega_i t) + c.c., \quad (2.63)$$

where i is the label for each transverse mode, and p is the total number of transverse modes under consideration. The $\psi_i(r, \phi)$'s and $A \sin(\beta z)$ are normalized according to Eqs. (2.47) and (2.48), respectively, and $|E_i|^2$ corresponds to the photon number in the i -th mode. The polarization unit vector \hat{e}_i is allowed to be different for different modes. The wave number $\beta = \hat{q}\pi/L$ is the same for all transverse modes because all transverse modes correspond to the same longitudinal mode for a VCSEL. Since the spatial distributions of the transverse modes are orthogonal to each other, we can easily obtain a set of equations for the complex mode amplitude $E_i(t)$ for each mode i by projecting the Helmholtz equation into the corresponding space $[\psi_i^*(r, \phi) \sin(\beta z)]$. Writing the temporal part of i -th mode as $\mathcal{E}_i(t) = E_i(t) \exp(-i\omega_{th,i}t)$, the equation governing the dynamics of the field $E_i(t)$ can be written as

$$\frac{dE_i}{dt} = \frac{1}{2}(1 - i\alpha)[G_i(t) - \gamma_i]E_i, \quad (2.64)$$

where $G_i(t)$ and γ_i are the gain and cavity loss for the i -th mode. Since both the modal gain and the refractive index depend on the carrier density N in the VCSEL cavity, a complete description of the laser characteristics requires the knowledge of the carrier dynamics.

2.3 The Carrier Rate Equation

When a voltage is applied across a semiconductor laser, charge carriers (electrons and holes) are injected into the thin active region, where they recombine through radiative or nonradiative mechanisms. Radiative recombination occurs when an electron in the conduction band recombines with a hole in the valence band and the excess energy is emitted in the form of a photon. Two recombination processes are spontaneous emission and stimulated emission. Nonradiative recombination of an electron-hole pair is characterized by the absence of an emitted photon during the recombination process. The rate equation governing the dynamics of the carrier density $N(r, \phi, z, t)$ can be written as [59]

$$\frac{\partial N(r, \phi, z, t)}{\partial t} = D\nabla^2 N + \frac{J(r, \phi)}{qL} - \frac{N}{\tau_e} - BN^2 - v_g g(r, \phi, z, t)|\mathcal{E}(r, \phi, z, t)|^2. \quad (2.65)$$

The first term on the right side accounts for carrier diffusion, where D is the diffusion coefficient. The second term accounts for the generation of carriers as a result of applying the injection current; $J(r, \phi)$ is the current density (per unit area) whose spatial distribution is determined by the shape and size of metallic contacts deposited on the two mirrors, and q is the electron charge. By setting the injection current to zero outside the contact area, current spreading effects are neglected. Such effects must be

included for a realistic comparison of the numerical results with the experiments [38]. However, since the qualitative nature of the results are not expected to change with the inclusion of current spreading effects, we neglect such effects in our study. The third term is due to nonradiative carrier recombination at defects or impurities, and τ_e is the effective carrier lifetime. The fourth term is due to spontaneous radiative recombination, and B is the spontaneous recombination coefficient. The last term in Eq. (2.65) accounts for carrier loss through stimulated emission, whose rate depends on the photon density $|\mathcal{E}|^2$ and the material gain $g(r, \phi, z, t)$ given by Eq. (2.38).

In the absence of diffusion ($D = 0$), the carrier spatial distribution is governed by $J(r, \phi)$ and often exhibits a dip where the field is most intense (spatial hole-burning). However, diffusion nearly eliminates spatial hole-burning resulting from the longitudinal standing-wave pattern (z direction). For a lasing wavelength of $\lambda_0 = 0.8 \mu\text{m}$, the period of the standing-wave pattern in the semiconductor laser medium (assuming a refractive index of $n = 3.5$) is $\lambda_m = \lambda_0/n \approx 0.2 \mu\text{m}$. For a typical diffusion coefficient of $D = 30 \text{ cm}^2/\text{s}$ and an effective carrier lifetime of $T_1 = \tau_e(1 + B\tau_e N_{th})^{-1} \approx 2 \text{ ns}$, the diffusion length is $L_d = \sqrt{DT_1} \approx 2 \mu\text{m}$. Since the diffusion length is much larger than the period of the longitudinal standing wave ($L_d \gg \lambda_m$), longitudinal variations in the carrier density are effectively washed out by diffusion, and we can assume that the carrier density is uniform in the longitudinal (z) direction, i.e. $N(r, \phi, t)$. However, transverse spatial hole-burning effects cannot be neglected, since the transverse dimension of a VCSEL ($\sim 10 \mu\text{m}$ radius) is typically much larger than the diffusion length. For this reason, the term $\nabla^2 N$ in Eq. (2.65) can be replaced by $\nabla_T^2 N$, where ∇_T^2 is the transverse part of the Laplacian operator ∇^2 . Substituting the total field given by Eq. (2.63) into the carrier rate equation (2.65) and integrating in z over the length L of the laser cavity, we obtain

$$\begin{aligned} \frac{\partial N(r, \phi, t)}{\partial t} = & D\nabla_T^2 N + \frac{J(r, \phi)}{qd} - \frac{N}{\tau_e} - BN^2 - \frac{1}{d}\Gamma_L v_g g(r, \phi, t) \times \\ & \left\{ \sum_{i=1}^p |E_i \psi_i|^2 + \sum_{i \neq j} (\hat{\mathbf{e}}_i E_i \psi_i) \cdot (\hat{\mathbf{e}}_j E_j \psi_j)^* \exp\{-i(\omega_i - \omega_j)t\} \right\}, \end{aligned} \quad (2.66)$$

where $g(r, \phi, t)$ is given by Eq. (2.56), and the longitudinal confinement factor Γ_L results from spatial averaging of the field over z and is given by Eq. (2.57). The $1/d$ coefficient appears in front of the stimulated emission term due to the fact that the carriers N are present only in the active region (with thickness d). In general, the interference term represented by the last term in Eq. (2.66) should be included. However,

since the frequency difference between transverse modes $\omega_i - \omega_j$ is on the order of 100 GHz due to waveguide dispersion, the beating terms fluctuate on a picosecond time scale. As long as $(\omega_i - \omega_j)T_1 \gg 1$, the carrier density cannot respond on such a fast time scale and such terms can be neglected. Dropping the interference terms, we arrive at the following simplified form for the carrier-density rate equation:

$$\frac{\partial N(r, \phi, t)}{\partial t} = D\nabla_T^2 N + \frac{J(r, \phi)}{qd} - \frac{N}{\tau_e} - BN^2 - \frac{1}{d}\Gamma_L v_g g(r, \phi, t) \sum_{i=1}^p |E_i(t)\psi_i(r, \phi)|^2. \quad (2.67)$$

Although we have eliminated the longitudinal variations in Eq. (2.67), the important transverse effects are included.

It follows from Eq. (2.67) that the quantity $|E_i|^2$ is the photon number in the i -th mode. However, the quantity of interest in many cases is not the intracavity photon number, but the power emitted from a facet. The power P_{out} emitted from each facet is related to the intracavity photon number $|E|^2$ by the relation

$$P_{out} = \frac{1}{2}h\nu v_g \alpha_m |E|^2, \quad (2.68)$$

where the factor of $\frac{1}{2}$ is due to the assumption of equal facet reflectivities.

One fine tuning worth mentioning is the intensity dependence of the gain. Although gain saturation due to interband transitions is incorporated in Eq. (2.67), at high intracavity powers, the gain can also be saturated due to a finite relaxation time of the intraband scattering processes (\sim fs). The gain is experimentally observed to saturate at high intensities because of phenomena such as carrier heating, free-carrier absorption, and spectral hole-burning. There is considerable discussion on the functional form of $G_i(P)$ since it depends on the underlying process responsible for gain saturation. Fortunately, the nonlinear reduction in gain is usually sufficiently weak in practice because of relatively low power emitted by VCSELs, and gain saturation is small and can be neglected. However, when the laser undergoes large-amplitude oscillations or operates far above threshold, the inclusion of gain saturation may be necessary. In that case, we use the following functional form:

$$G_i(P) = \frac{G_i}{1 + (\epsilon_{NL}/V_m)|E_i|^2}, \quad (2.69)$$

where V_m is the mode volume, and ϵ_{NL} is the nonlinear-gain parameter with a typical value of $\epsilon_{NL} = 1 \times 10^{-17} \text{ cm}^3$. We will consider the effect of nonlinear gain in the following chapters when necessary.

The complete model is given by the field equation (2.64) and the carrier-density rate equation (2.67). In the presence of external influence, it is possible to consider the rate equations for the laser cavity alone,

and the field equation (2.61) should be modified by including terms which account for the contribution of the external influence. These modifications will be discussed in subsequent chapters.

2.4 Approximate Steady-State Characteristics

The complete model given by Eqs. (2.64) and (2.67) can be used to obtain the emission characteristics of a VCSEL numerically. However, considerable insight can be gained by considering the CW characteristics of a single-mode VCSEL using simplifications that allow for an approximate analytic solution. In this section we neglect carrier diffusion ($D = 0$) and assume a spatially uniform carrier density N . We also assume a constant, carrier-independent lifetime T_1 . Under single-mode operation, we write the optical field in the form

$$E(t) = \sqrt{P(t)} \exp\{-i\varphi(t)\}, \quad (2.70)$$

where $P(t)$ is the intracavity photon number and $\varphi(t)$ is the optical phase. Substituting Eq. (2.70) into Eqs. (2.64) and (2.67), we obtain the following set of spatially independent rate equations:

$$\frac{dP}{dt} = [G_N(N - N_T) - \gamma]P, \quad (2.71)$$

$$\frac{dN}{dt} = \frac{J}{qd} - \frac{N}{T_1} - \frac{1}{V_m}[G_N(N - N_T)]P, \quad (2.72)$$

$$\frac{d\varphi}{dt} = \frac{1}{2}\alpha[G_N(N - N_T) - \gamma], \quad (2.73)$$

where $N(t)$ is the spatially uniform carrier density, $G_N = \Gamma_L a_0 v_g$ is the differential gain, V_m is the mode volume of the field, and J is the injection current density. The CW solutions are characterized by a fixed photon number P_0 , a fixed carrier density N_0 , and a constant angular frequency shift $\Delta\omega = \omega - \omega_{th} = d\varphi/dt$ from the threshold frequency ω_{th} . These solutions are obtained by solving Eqs. (2.71)–(2.73) with $dP/dt = dN/dt = 0$. The threshold is defined as the condition when the modal gain balances the losses ($G = \gamma$), and the carrier density N_{th} and injection current density J_{th} at threshold are given by

$$N_{th} = \frac{\gamma}{G_N} + N_T, \quad (2.74)$$

$$J_{th} = qd \frac{N_{th}}{T_1}. \quad (2.75)$$

For $J < J_{th}$, the steady-state solutions are

$$P_0 = 0, \quad (2.76)$$

$$\Delta\omega = \frac{1}{2}\alpha G_N \frac{1}{qd} T_1 (J - J_{th}), \quad (2.77)$$

$$N_0 = \frac{J}{qd}T_1. \quad (2.78)$$

For $J > J_{th}$, the carrier density and the frequency shift are clamped (fixed), and the photon number is proportional to the current density J :

$$P_0 = \frac{1}{qd\gamma}(J - J_{th})V_m, \quad (2.79)$$

$$\Delta\omega = 0, \quad (2.80)$$

$$N_0 = N_{th}. \quad (2.81)$$

Assuming that the current is uniformly injected over an area A_p and using Eq. (2.68), the output power (light) can be related to the injection current I by

$$P_{out} = \frac{1}{2}h\nu v_g \alpha_m \left\{ \frac{1}{qd\gamma}(I - I_{th}) \frac{V_m}{A_p} \right\}. \quad (2.82)$$

The variation of P_{out} with I is known as the light-current (L-I) curve, and $I_{th} = J_{th}A_p$ is the threshold current. Under single-mode operation, the L-I curve shows a linear relation for all injection currents. However, we will see in Chapter 3 that multiple-transverse-mode operation can affect the L-I curves considerably.

2.5 Computational Procedure

The carrier and field equations [Eqs. (2.64) and (2.67)] are integrated numerically using a finite-difference method in both the temporal and spatial domains. The temporal domain is discretized into uniform steps of 0.1 ps duration. To ensure that transients have died out, data for the steady-state characteristics are collected after numerically integrating the rate equations using a first-order finite-difference method over a temporal window of duration 5–8 ns, which is much larger than the damping time of relaxation oscillations. The initial conditions can be chosen quite arbitrarily (within reason). First, the initial conditions corresponding to spontaneous noise are used to find the threshold current density J_{th} . The threshold is found by simulating CW operation for a total duration of 5 ns at various current levels. The current is increased through steps of 0.1 mA and simulations are repeated until the output power first exceeds $1 \mu\text{W}$, which is defined as the threshold condition. For fast convergence to the steady-state solution, the field at threshold (or above threshold) can then be used as the initial conditions for simulations under different operating conditions.

The carrier equation requires an implicit solution in the radial direction due to coupling introduced by the diffusion term. To solve for $N(r)$ at any given point in time, the spatial domain is divided evenly into $K = 100$ steps. Our radial mesh runs from δr to $R = K\delta r$, where $\delta r = 0.1 \mu\text{m}$ is the spatial resolution, and $R = 10 \mu\text{m}$ is the radius of the device. The point $r = 0$ is excluded because of the singularity associated with the Laplacian term. The boundary conditions $N(0) = N(\delta r)$ and $N(R) = 0$ are used. Since the diffusion term involves a second-order derivative of $N(r)$, each $N(r)$ is coupled only to its nearest neighbors $N(r + \delta r)$ and $N(r - \delta r)$. Therefore, provided that the gain is a linear function of $N(r)$, the carrier equation can be casted into the form of a tridiagonal matrix, which can be easily inverted to obtain a solution for $N(r)$. In spite of the matrix inversion involved, the computer code is reasonably fast. A typical run takes less than 5 minutes on a Sparc 5 workstation.

Parameters

An index-guided GaAs VCSEL with cylindrical geometry (index guiding over $4\text{-}\mu\text{m}$ radius) is chosen for this study. The active region consists of three 8-nm quantum wells. The radius of the device corresponds to the radius of the active region, which is taken to be $10 \mu\text{m}$. In such a structure, the optical field is effectively confined within the index-guided region, whereas the carriers can diffuse out of the index-guided region. For a typical GaAs VCSEL, the diffusion coefficient is about $30 \text{ cm}^2/\text{s}$. A ring or disc contact supplies current to the active region. Both the shape and dimension of the metallic contact through which the current is injected are adjustable through the term $J(r, \phi)/(qd)$ in the carrier rate equation (2.67). Single-mode operation can be realized by using a narrow disc contact such that current is injected only over a small central part of the VCSEL top area. The fundamental LP_{01} mode is then preferentially excited. For multimode operation, different transverse modes can be excited by a ring or wide disc contact. We assume that $\gamma_i = \gamma$ for all modes, since different transverse modes experience nearly the same loss in practice. Other device parameters used in simulations are shown in Table 2.1.

Table 2.1: *Device parameters used in simulations*

Cavity length L_{eff}	$2 \mu\text{m}$
Active-region thickness d (3 QWs)	$3 \times 8 \text{ nm}$
Radius of device R	$10 \mu\text{m}$
Radius of index-guiding region a	$4 \mu\text{m}$
Diffusion constant D	$30 \text{ cm}^2/\text{s}$
Non-radiative recombination time τ_e	5 ns
Bimolecular recombination coefficient B	$1 \times 10^{-10} \text{ cm}^3/\text{s}$
Refractive index inside index-guided region n_1	3.5
Refractive index outside index-guided region n_2	3.4
Group index n_g	3.5
Wavelength λ	$0.875 \mu\text{m}$
Gain cross-section a_0	$2.0 \times 10^{-16} \text{ cm}^2$
Carrier density at transparency N_T	$2.2 \times 10^{18} \text{ cm}^{-3}$
Linewidth enhancement factor α	3
Mirror reflectivities R_1, R_2	0.995
Internal loss α_{int}	20 cm^{-1}
Longitudinal confinement factor Γ_L	0.012

Chapter 3

CW Operation

We first discuss the simplest case in which a VCSEL operates continuously when a constant current is applied to it. We study the static (Section 3.1) and noise (Section 3.2) characteristics under CW operation. In particular, we investigate the effects of contact geometry and carrier diffusion on multimode characteristics. At low injection currents, the fundamental mode consumes carriers mostly near the peak of its intensity profile, which results in the formation of a central dip in the carrier-density profile. This process is known as spatial hole-burning, and results in a local depletion of carriers and the onset of higher-order transverse modes at higher injection currents. Since different transverse modes have different spatial distributions, the shape and size of the current contact plays an important role in determining the number and types of transverse modes excited. Diffusion also plays an important role by spreading out the carriers and partly filling the spatial holes, thus counteracting the effects of spatial hole-burning.

3.1 L-I Characteristics

The L-I characteristics under CW operation are obtained from Eqs. (2.64) and (2.67). They are calculated by numerically integrating these equations for a temporal window of 5 ns to eliminate the transients.

3.1.1 Contact Geometry

To investigate the effect of contact geometry, three different geometries are considered: (a) 2- μm disc; (b) 4- μm disc; (c) 1.8-2.8 μm ring. The L-I characteristics for these three cases are shown in Fig. 3.1, where the dashed, solid, and dot-dashed lines represent the LP₀₁, LP₁₁, and LP₂₁ modes, respectively. Clearly, the number and types of transverse modes excited are significantly affected by the contact geometry. For current injection over a 2- μm -radius contact, the LP₀₁ mode is selectively excited, since carriers are injected near the peak of the intensity profile of the LP₀₁ mode (Fig. 3.1a). Under single-

mode operation, the L-I curve shows a linear relation, as predicted by single-mode spatially independent rate equations discussed in Section 2.4. However, for a 4- μm disc, the VCSEL operates in one or two modes depending on the injection current (Fig. 3.1b). At low currents (3.7–4.7 mA), the VCSEL operates in a single transverse mode, which is the fundamental LP_{01} mode. As the current is increased, spatial hole-burning results in the onset of the first-order LP_{11} transverse mode at 4.7 mA. The turn-on of the LP_{11} mode is possible in this case since a wide disc contact also supplies gain to this mode. Further, Fig. 3.1b shows that the slope efficiency of the LP_{01} mode changes abruptly when the second mode turns on. This decrease in slope efficiency is attributed to weak mode competition due to sharing of charge carriers, since the LP_{11} mode consumes some of the carriers that are originally used by the LP_{01} mode.

Fig. 3.1c shows that a ring contact selectively excites the LP_{11} and LP_{21} modes. The change in the slope efficiency of the LP_{11} mode after the turn-on of the LP_{21} mode is even more drastic than that occurring in Fig. 3.1b. This behavior can be understood by considering the radial intensity distributions shown in Fig. 2.2. Since spatial overlap between these two modes is strong, spatial hole-burning in the region where the two modes overlap leads to severe carrier competition. Therefore, an increase in the power of the LP_{21} mode leads to a simultaneous suppression of the LP_{11} mode.

The carrier-density profiles for the three contact geometries in Fig. 3.1 are plotted in Fig. 3.2 for operation at $J = 2J_{th}$. In Fig. 3.2a, no spatial hole is formed because diffusion effectively smoothes out

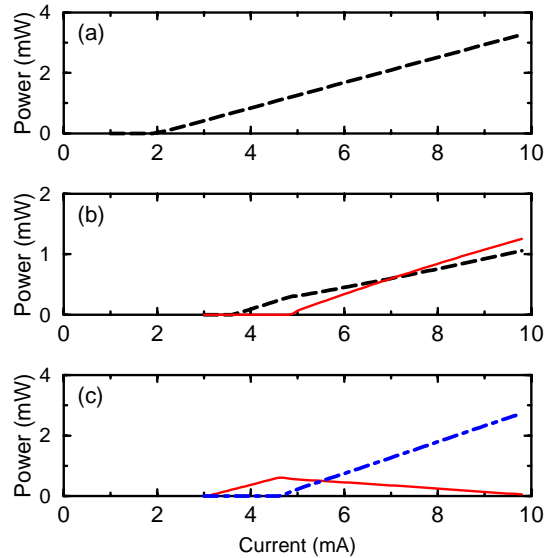


Figure 3.1: L-I characteristics for three different contact geometries. (a) 2- μm disc, (b) 4- μm disc, and (c) 1.8-2.8 μm ring. Dashed, solid, and dot-dashed lines correspond to the LP_{01} , LP_{11} , and LP_{21} transverse modes, respectively.

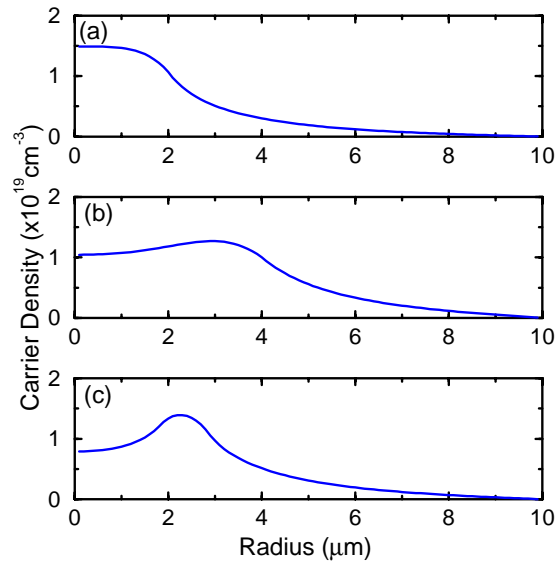


Figure 3.2: Radial carrier-density profiles at two times above threshold corresponding to the three contacts used in Figs. 3.1a–c.

any inhomogeneities over the small contact radius of $2 \mu\text{m}$ (estimated diffusion length $\sim 2 \mu\text{m}$). The small disc contact also provides better mode discrimination by supplying carriers primarily to the LP_{01} so that the higher-order transverse modes see negligible gain. However, in Fig. 3.2b, a wide spatial hole is burnt in the carrier profile because of gain saturation of the fundamental LP_{01} mode and is responsible for the onset of the LP_{11} mode. In Fig. 3.2c, the carriers peak near a radius of $2\text{--}3 \mu\text{m}$, since current is supplied over a quite narrow ring. Clearly, current injection in the region where two strongly overlapping modes peak results in strong carrier competition.

3.1.2 Carrier Diffusion

From the above discussion, it is clear that the overlap between the spatial profiles of the injected carriers and transverse modes play important roles in determining the L-I characteristics of VCSELs. Since the spatial distribution of the carriers can be controlled to some extent by controlling the size and shape of the current contact, it is possible to control the excitation of different transverse modes. However, the control is not as easy to implement as one wants partly due to carrier diffusion, which is responsible for an inherent tendency for confined carriers to spread. The strength of diffusion is governed by the diffusion coefficient in our model in Eq. (2.67). To study the effects of transverse diffusion, calculations are repeated with negligible transverse diffusion ($D = 1 \text{ cm}^2/\text{s}$).

Fig. 3.3 shows the change in L-I characteristics for the three contact geometries used in Figs. 3.1a–c.

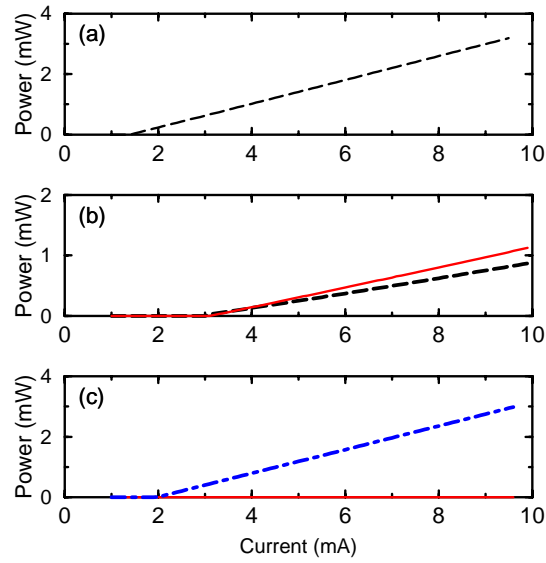


Figure 3.3: L - I characteristics with negligible diffusion ($D = 1 \text{ cm}^2/\text{s}$) for three different contact geometries. (a) $2\text{-}\mu\text{m}$ disc, (b) $4\text{-}\mu\text{m}$ disc, and (c) $1.8\text{-}2.8 \mu\text{m}$ ring. Dashed, solid, and dot-dashed lines correspond to the LP_{01} , LP_{11} , and LP_{21} transverse modes, respectively.

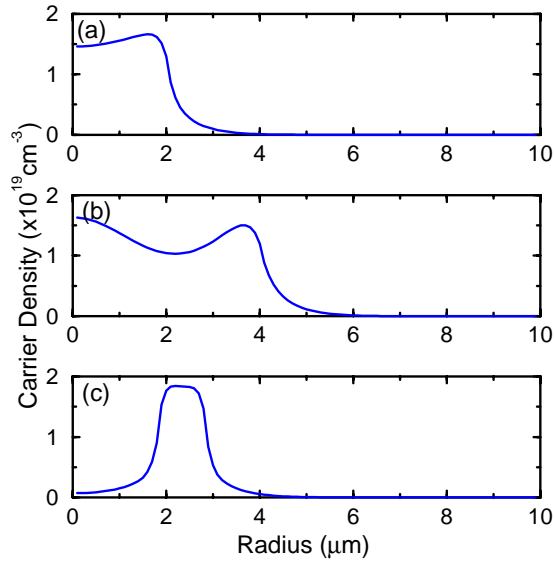


Figure 3.4: Radial carrier-density profiles at two times above threshold corresponding to the three contacts used in Figs. 3.3a–c where diffusion effects are neglected.

The corresponding carrier-density profiles at two times above threshold are shown in Fig. 3.4. Compared with Fig. 3.2, the carrier-density distributions are highly inhomogeneous with negligible diffusion, since diffusion spreads out the carriers. In particular, Fig. 3.4a shows that a spatial hole is burnt in the carrier profile even for a $2\text{-}\mu\text{m}$ -radius contact. Diffusion also increases the threshold under single-mode operation because it reduces the overlap between the fundamental LP_{01} mode and the carrier-density profile

by spreading out the carriers (compare Fig. 3.2a and Fig. 3.4a). For the case of two weakly overlapping modes, a comparison of Fig. 3.1b and 3.3b reveals that diffusion raises the threshold for the LP₁₁ mode. Since diffusion partly refills the spatial hole burnt by the LP₀₁ mode and thus reduces the gain-saturation effect due to the local depletion of carriers, the turn-on of the LP₁₁ mode is delayed to much higher currents compared with the case of negligible diffusion. For two strongly overlapping modes, diffusion reduces mode competition by supplying carriers over a wider region so that two-mode operation is possible in the presence of diffusion (Fig. 3.1c), whereas single-mode (LP₂₁) operation is observed up to 10 mA when diffusion effects are neglected (Fig. 3.3c).

3.2 Noise Characteristics

So far we have neglected the effect of spontaneous emission, and the laser power and frequency are assumed to remain constant in time once the steady state has been reached. In reality, the laser output exhibits intensity as well as phase fluctuations. At the most fundamental level, these fluctuations arise from the process of spontaneous emission which has a quantum-mechanical origin and can be incorporated into the rate equations via the Langevin noise sources [62]. By representing the optical field as

$$\mathcal{E}(t) = \sqrt{P(t)} \exp[-i(\omega_0 t + \varphi)], \quad (3.1)$$

a spontaneous-emission event is described as an increase in the photon number P by unity and an accompanying random change in the phase φ of the optical field occurring at random time intervals. Assuming that different events are uncorrelated, the time dependence of the complex amplitude of the field $E(t) = \sqrt{P(t)} \exp(-i\varphi)$ is given by

$$\frac{\partial E}{\partial t} = F(t), \quad (3.2)$$

where $F(t)$ is a Langevin force describing a Markoffian Gaussian process with zero mean and δ -function correlation such that [63]

$$\langle F(t) \rangle = 0, \quad (3.3)$$

$$\langle F(t_1)F^*(t_2) \rangle = R_{sp}\delta(t_1 - t_2), \quad (3.4)$$

where $R_{sp} = n_{sp}\gamma$ is the average rate of spontaneous emissions into the laser mode, and n_{sp} is the spontaneous emission factor related to the degree of population inversion [59]. For semiconductor lasers, an appropriate value of n_{sp} is 1.8. To include the effect of spontaneous emission, the field rate equation

(2.64) is modified by simply adding the stochastic Langevin noise term on the right side:

$$\frac{dE_i}{dt} = \frac{1}{2}(1 - i\alpha)[G_i(t) - \gamma_i]E_i + F_i(t), \quad (3.5)$$

where $F_i(t)$ is the Langevin noise term.

In the presence of spontaneous emission, the laser output power fluctuates around its steady-state value. The spectrum of such power fluctuations is referred to as the intensity-noise spectrum. The intensity noise at a given frequency ω is characterized by the relative-intensity noise (RIN):

$$RIN = \frac{S_p(\omega)}{\bar{P}^2}, \quad (3.6)$$

where \bar{P} is the average steady-state power in the presence of noise, and the spectral power density is given by

$$S_p(\omega) = \int_{-\infty}^{+\infty} \langle \delta P(t + \tau) \delta P(t) \rangle \exp(-i\omega\tau) d\tau, \quad (3.7)$$

where the angle brackets denote an ensemble average, and $\delta P(t)$ is the small perturbation around the average power \bar{P} . The spectral power density $S_p(\omega)$ can be related to the Fourier transform $\delta \tilde{P}(\omega)$ by the following relation:

$$S_p(\omega) = \langle |\delta \tilde{P}(\omega)|^2 \rangle. \quad (3.8)$$

Since each spontaneously emitted photon changes the optical phase by a random amount, spontaneous emission also leads to phase fluctuations, which results in a frequency shift:

$$\delta\omega = \delta\dot{\varphi}, \quad (3.9)$$

where $\dot{\varphi}$ denotes the time derivative of φ . The frequency or phase noise is of interest in evaluating the performance of coherent communication systems. The spectral density of the frequency noise or the frequency-noise spectrum (FNS) is defined similar to the intensity-noise case [Eq. (3.7)] and is given by

$$S_{\dot{\varphi}} = \int_{-\infty}^{+\infty} \langle \delta\dot{\varphi}(t + \tau) \delta\dot{\varphi}(t) \rangle \exp(-i\omega\tau) d\tau, \quad (3.10)$$

It is related to $\delta\tilde{\varphi}(\omega)$ by

$$S_{\dot{\varphi}} = \langle |\omega \delta\tilde{\varphi}(\omega)|^2 \rangle. \quad (3.11)$$

The noise characteristics are obtained by numerically integrating Eqs. (3.5) and (2.67) and averaging over 30 trajectories, each of duration 26 ns, resulting in a resolution of 38 MHz over a 20-GHz frequency range. The RIN spectrum and FNS are calculated using Eqs. (3.6) and (3.10), respectively. To reduce

the impact of performing an ensemble average over a finite number of trajectories, the noise spectra are slightly smoothed by performing a 20-point running average.

Single-Mode Operation

We first consider the case in which the VCSEL operates in a single transverse mode (LP_{01}) by using a disc contact of $2\text{-}\mu\text{m}$ radius. The RIN spectrum at two times above threshold is shown as a solid line in Fig. 3.5a, corresponding to an output power of about 0.9 mW . The resonance peak near 6 GHz corresponds to the well-known relaxation-oscillation frequency [59]. The peak value of about -125 dB/Hz is of the same order of magnitude as that observed in edge-emitting lasers [59]. The FNS shows a similar resonance peak near 6 GHz (solid line in Fig. 3.5b) because power fluctuations are related to fluctuations

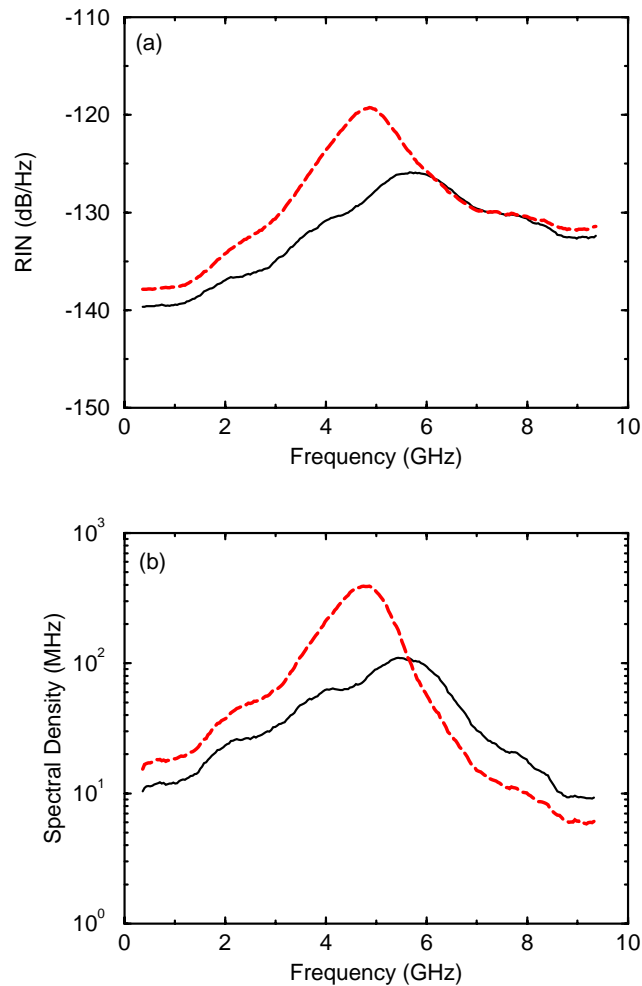


Figure 3.5: Noise characteristics under single-mode operation at two times above threshold. (a) RIN; (b) FNS. Solid and dashed traces correspond to diffusion constants of 30 and $1\text{ cm}^2/\text{s}$, respectively.

in the carrier population, which in turn leads to a phase change. The proportionality between the gain and index changes is provided by α [Eq. (2.41)].

To investigate the effects of transverse carrier diffusion on noise characteristics, we have repeated the calculations for the case of negligible transverse diffusion by setting $D = 1 \text{ cm}^2/\text{s}$. The RIN and FNS spectra are illustrated by the dashed lines in Figs. 3.5a and 3.5b, respectively. Transverse carrier diffusion is found to affect the RIN and FNS considerably. Our results show a 20-25% increase in the relaxation-oscillation frequency and a reduction by a factor of 5 in the peak height because of carrier diffusion, indicating its beneficial effects in VCSELs.

It has been shown that the linewidth of a semiconductor laser is given by the spectral density of the FNS at $\omega = 0$ [59]. According to Fig. 3.8, the linewidth of the VCSEL is about 16 MHz when diffusion effects are neglected (dashed line). With the inclusion of diffusion, the linewidth (11 MHz) is reduced by about 50%. Referring to Figs. 3.1a and 3.3a, we find that the output powers at two times above threshold are 0.9 mW and 0.6 mW respectively for $D = 30 \text{ cm}^2/\text{s}$ (significant diffusion) and $1 \text{ cm}^2/\text{s}$ (negligible diffusion). Since the linewidth is inversely proportional to the output power [59], the linewidth is narrower in the presence of diffusion due to a higher output power at two times above threshold.

Two-Mode Operation

Next, we study the noise characteristics under two-mode operation. To investigate the effects of different transverse modes, the contact geometries corresponding to those used in Figs. 3.1b (4- μm disc) and 3.1c (1.8-2.8 μm ring) are used to excite the LP_{01} and LP_{11} modes and the LP_{11} and LP_{21} modes, respectively.

The RIN spectra shown in Fig. 3.6a for the case of a ring contact correspond to 6-mA current (two times above threshold of the LP_{11} mode), for which the powers in the LP_{11} and LP_{21} modes are about 0.4 and 0.8 mW, respectively. Clearly, power fluctuations in individual transverse modes are larger by up to a factor of 100 (20-dB enhancement) than those of the total power for frequencies up to 4 GHz. This low-frequency-noise enhancement is known as mode-partition noise [59]. It arises when the two modes fluctuate in such a way as to leave the total power relatively constant due to the fact that the same carrier population provides gain for both modes. The LP_{11} mode exhibits larger fluctuations because of its lower average power. A random increase in the power of one mode induces a simultaneous decrease in the power of the other mode, which lasts a few nanoseconds because of relaxation oscillations. Mode-partition noise

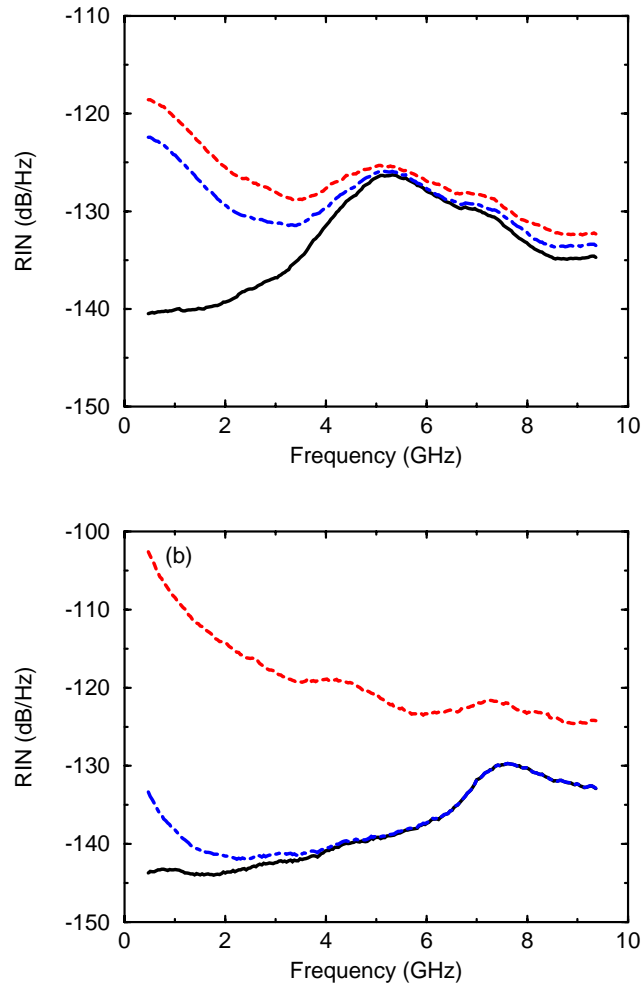


Figure 3.6: RIN characteristics under two-mode operation with a ring contact with injection current set at (a) 2 and (b) 3 times above threshold. Solid, dashed, and dot-dashed traces correspond to noise for the total power, the LP_{11} , and LP_{21} transverse modes, respectively.

has been experimentally observed in both VCSELs and edge-emitting lasers [16]. In the case of VCSELs, transverse effects such as carrier diffusion and spatial hole-burning can affect the mode-partition noise dramatically, as will become clear in what follows.

Consider first the impact of the relative powers in each mode on the mode-partition noise. Since the spatial distributions of the LP_{11} and LP_{21} modes overlap significantly, as the current is increased, one mode becomes dominant while the other mode is suppressed due to carrier competition induced by spatial hole-burning [31] (refer to the L-I curves in Fig. 3.1c). Fig. 3.6b shows the RIN spectra under conditions identical to those of Fig. 3.6a except at three times above threshold, corresponding to powers of 0.1 and 2.3 mW in the LP_{11} and LP_{21} modes, respectively. The weak LP_{11} mode shows much higher

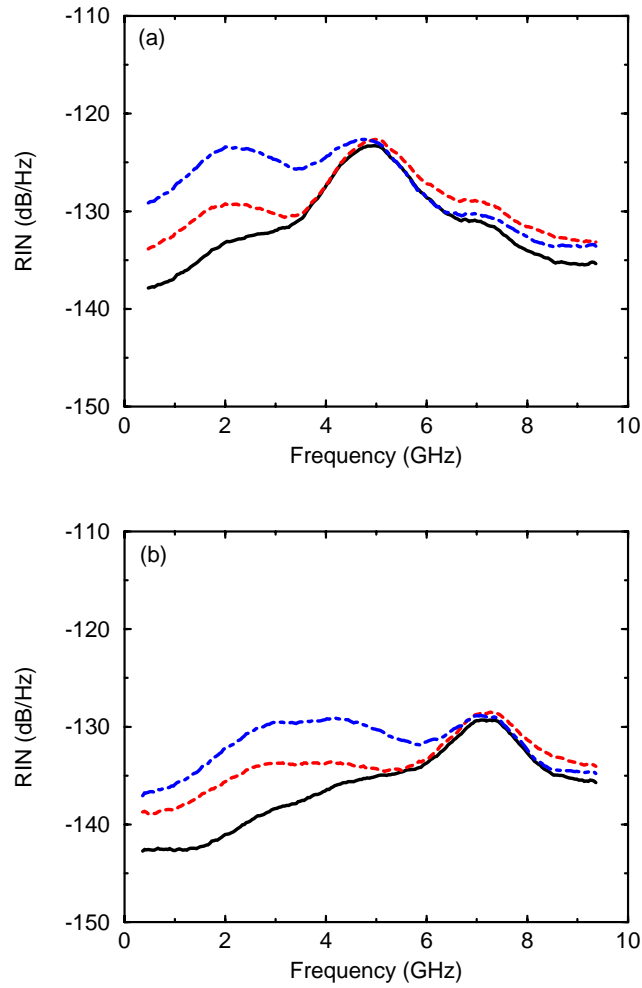


Figure 3.7: RIN characteristics under two-mode operation with a $4\text{-}\mu\text{m}$ -wide disc contact with injection current set at (a) 2 and (b) 3 times above threshold. Solid, dashed, and dot-dashed traces correspond to noise for the total power, the LP_{01} and the LP_{11} transverse modes, respectively.

RIN because of its lower average power, and the dominant LP_{21} mode exhibits RIN enhancement over a smaller frequency range (0–1 GHz).

To further investigate the effect of spatial hole-burning, the RIN spectra for the case of a disc contact ($4\text{-}\mu\text{m}$ radius) are shown in Fig. 3.7a. The current is two times above threshold for the LP_{01} mode, and the mode powers are nearly equal (about 0.7 mW). The low-frequency enhancement of the RIN for individual modes is reduced by a factor of 10 compared with the case shown in Fig. 3.6a, even though the VCSEL operates in two modes in both cases. The same device parameters are used, except for a disc contact which excites the LP_{01} and LP_{11} modes while the ring contact excites the LP_{11} and LP_{21} modes. These results can be understood from the mode profiles shown in Fig. 2.2. The LP_{01} and LP_{11} modes have a

smaller region of overlap, carrier competition is less intense for a disc contact, despite the fact that the two modes carry the same amount of power. At three times above threshold, mode-partition noise is found to be reduced so much that the low-frequency noise is lower than that occurring at the relaxation-oscillation peak (Fig. 3.7b). Thus, contrary to relatively high mode-partition noise in edge-emitting lasers operating in several longitudinal modes but in a single transverse mode, multiple-transverse-mode VCSELs can be made with reduced mode-partition noise through the use of an appropriate pumping geometry.

An interesting feature of Fig. 3.7a is the appearance of a second peak near 2 GHz in addition to the relaxation-oscillation peak at 5 GHz. Such a peak has never been observed in the RIN spectra of edge-emitting lasers, and its presence is solely due to multiple-transverse-mode operation. Its absence in Fig. 3.6 suggests that its origin lies in the disc-contact geometry. The LP_{01} and LP_{11} modes excited in such a VCSEL peak at $r = 0$ and $r \approx 2 \mu\text{m}$, as seen in Fig. 2.2. In contrast, the ring-contact geometry excites the LP_{11} and LP_{21} modes, both of which peak near $r = 2 \mu\text{m}$. A spatial hole is burnt in the carrier-density profile at the location where the mode intensity peaks. Clearly, two distinct spatial holes are burnt in the case of Fig. 3.6, whereas a single hole is burnt in the case of Fig. 3.7. As a result, carrier diffusion is much more effective in filling the spatial holes (and therefore reducing mode competition) in the case of a disc contact. For a diffusion constant of $30 \text{ cm}^2/\text{s}$ and a carrier recombination time of $T_1 \approx 2 \text{ ns}$, the effective diffusion rate is estimated to be about 2-3 GHz. Therefore, RIN enhancement is reduced due to diffusion effects for frequencies below 2 GHz but not in the frequency range 2-4 GHz, resulting in a shallow peak near 2 GHz. The inclusion of nonlinear gain reduces the peak values in Figs. 3.6 and 3.7 by about 2 dB, but the qualitative behavior remains unaffected.

The FNS at two times above threshold are shown in Figs. 3.8a-b for the two cases of two-mode operation with a disc and ring contact, respectively. Due to amplitude-phase coupling, the FNS show a relaxation-oscillation peak near 5 GHz similar to that observed in the RIN spectra in Figs. 3.6 and 3.7. However, the low-frequency-noise enhancement is much smaller than that occurring in the RIN spectrum. In Figs. 3.8a-b, the linewidths of individual modes (value of FNS for $\omega \rightarrow 0$) under two-mode operation are considerably larger than the linewidth of 11 MHz under single-mode operation. Because of carrier sharing between the two modes, the power carried by each mode is reduced. This reduction of mode powers leads to an increase in linewidth, which is inversely proportional to the output power [59]. For two-mode operation with a disc contact (Fig. 3.8a), the linewidths of the two modes are nearly equal (17 MHz) due to the fact that the two weakly coupled modes carry about the equal amount of power (0.7 mW). For

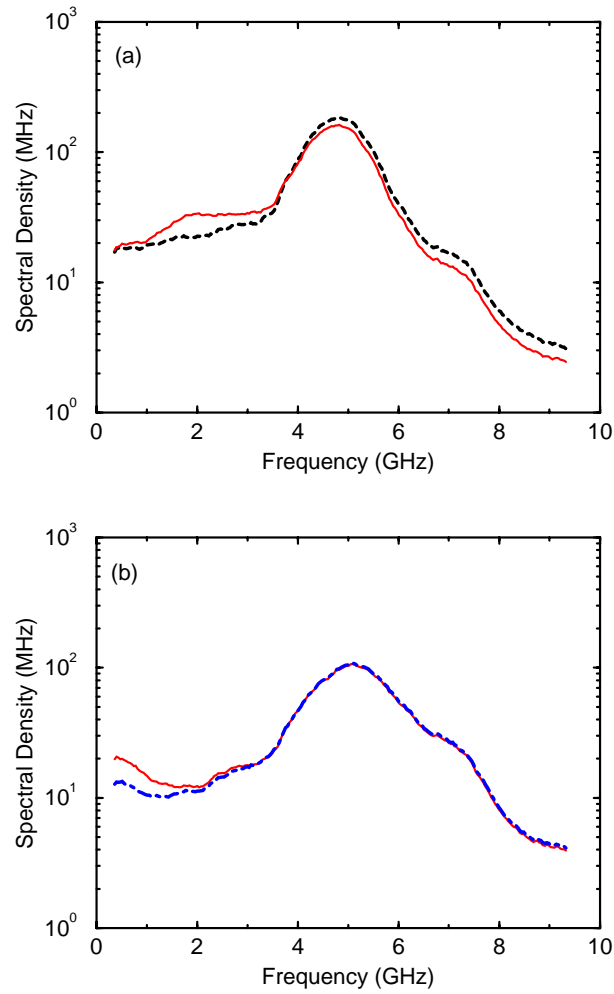


Figure 3.8: FNS under two-mode operation at 2 times above threshold with a (a) disc contact and (b) ring contact. Dashed, solid, and dot-dashed traces correspond to the LP_{01} , LP_{11} , and LP_{21} modes, respectively.

two-mode operation with a ring contact (Fig. 3.8b), the linewidths of the LP_{11} and the LP_{21} modes are 20 MHz and 14 MHz, corresponding to output powers of 0.4 mW and 0.8 mW, respectively. The LP_{11} mode has a larger linewidth because of its lower average power.

Chapter 4

Gain Switching

For applications in optical communication systems, the high-speed modulation characteristics of VCSELs are quite important. In this chapter we consider the mechanism of gain switching for generating picosecond pulses from a VCSEL. Section 4.1 investigates the effects of spatial hole-burning, carrier diffusion and contact geometry on ultrashort pulse generation under single-mode operation. Section 4.2 considers two-mode gain-switching operation and explores the change in nonlinear dynamics with the modulation frequency and current.

4.1 Ultrashort Pulse Generation

Gain switching involves biasing the laser below threshold and switching the modulation current periodically high above threshold. Each time the current swings above threshold, the laser responds with a series of relaxation oscillations. If the current is switched off before the onset of the second relaxation oscillation, a series of narrow pulses of picosecond duration can be generated. Obviously, the relaxation-oscillation frequency intrinsically limits the shortest attainable pulse duration. Although any shape of the current pulse can be studied using our model, we consider here the case of sinusoidal current modulation and assume the injected current density in Eq. (2.67) of the form

$$J(r, t) = \begin{cases} J_b + J_m \sin(2\pi f_m t) & \text{if } r_o < r < r_a \\ 0 & \text{otherwise} \end{cases} \quad (4.1)$$

where J_b is the bias current density, J_m is the modulation current density, f_m is the modulation frequency, and r_o and r_a are the inner and outer radii of the contact over which the current is injected. The bias is set at $J_b = 0.95J_{th}$ to ensure that the carrier density does not fall too far below the value needed to reach the threshold [64].

Table 4.1: *Output pulse characteristics at different modulation frequencies.*

Modulation frequency f_m (GHz)	2	3	4
Optimal value of J_m/J_{th}	8.0	12.4	17.8
Minimum pulse width (ps)	7.0	6.3	5.7
Peak power (mW)	111	138	173
Range of frequency shift (GHz)	232	270	288

4.1.1 Pulse Shape and Width

We first consider the practical case of ultrashort pulse generation under single-mode operation through gain switching. The effects of modulation frequency and modulation current on the characteristics of gain-switched pulses are studied. The threshold current density J_{th} is first obtained by using the procedure outlined in Chapter 2. Output pulse trains were obtained by setting $J_b/J_{th} = 0.95$ and $f_m = 2.5$ GHz in Eq. (4.1) for several values of modulation indices J_m/J_{th} . We consider the range of values of the modulation index J_m/J_{th} for which the device produces stable, regular gain-switched pulses at the modulation frequency. For small values of the modulation index, the device cannot respond fast enough, and the output power oscillates at a subharmonic of the modulation frequency [65]. By contrast, for large values of the modulation index, multiple relaxation-oscillation peaks are excited by a single current pulse. Numerical simulations show that the range $7 \leq J_m/J_{th} \leq 11$ corresponds to stable operation at the modulation frequency.

Fig. 4.1a shows the shape of gain-switched pulses for modulation indices $J_m/J_{th} = 8-11$ at a modulation frequency of $f_m = 2.5$ GHz and a bias of $J_b/J_{th} = 0.95$. The current pulse shape is also shown for comparison by a dashed line. As J_m/J_{th} increases, carrier density builds up faster. As a result, the output pulse shortens, and the delay between the current pulse and the output pulse decreases. Eventually, the delay becomes so short that a second relaxation-oscillation peak appears, as seen in Fig. 4.1a for $J_m/J_{th} = 11$. There exists an optimal value of J_m/J_{th} at which the pulse width is minimum. For the parameters used in Fig. 4.1a, the minimum pulse width of about 6 ps occurs for $J_m/J_{th} \approx 10$.

Direct current modulation also leads to the dynamic shift of the lasing frequency from its steady-state value over a wide range during each modulation cycle. This frequency shift has its origin in the

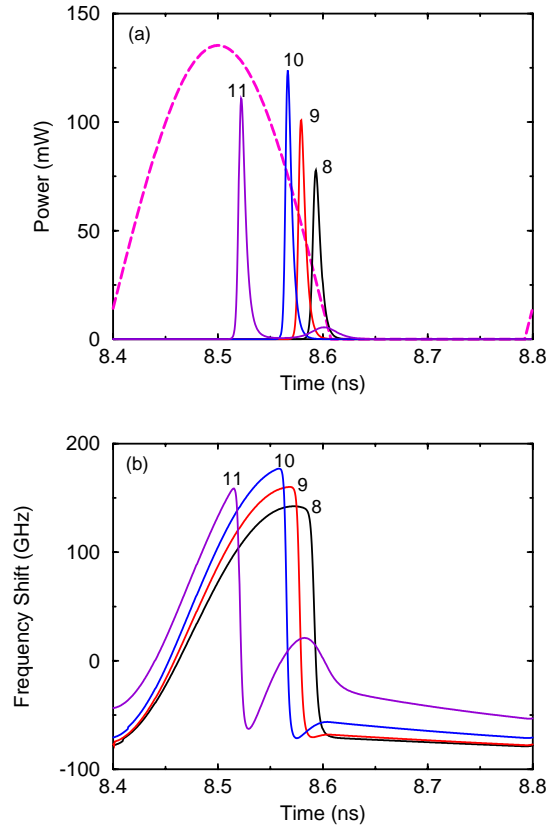


Figure 4.1: (a) Pulse shapes and (b) frequency-shift profiles of gain-switched pulses obtained through 2.5-GHz sinusoidal modulation of a VCSEL biased at $J_b/J_{th} = 0.95$. Dashed line shows the current pulse for comparison. The values of J_m/J_{th} are indicated next to each trace. Other parameter values are given in Table 2.1.

carrier-induced index change that accompanies any gain change in semiconductor lasers and leads to a significant dispersion penalty in optical communication systems. Fig. 4.1b shows the frequency shift $\Delta\nu = (1/2\pi)(d\varphi/dt)$ as a function of time corresponding to the pulse shapes of Fig. 4.1a, where φ is the optical phase defined in Eq. (2.70). As the pulse width decreases and the peak power increases at higher values of J_m , the frequency shift is expected to increase, since high peak powers and small pulse widths are associated with a higher rate of change of photon density. The most noteworthy feature of Fig. 4.1b is a large and sudden change (~ 200 GHz) in the carrier frequency occurring near the pulse peak. The magnitude of the jump increases with the modulation index. Since the lasing frequency shifts dynamically over a wide range during each modulation cycle, frequency shifting results in a dynamic broadening of the pulse spectrum compared with that of a transform-limited pulse (about 70 GHz for a pulse with duration of 6 ps).

Gain-switching characteristics for $f_m = 2\text{--}4$ GHz are shown in Table 4.1. As shown, the optimal modulation index J_m/J_{th} is observed to increase with the modulation frequency. This behavior can be understood by noting that the bandwidth of a VCSEL is limited by the relaxation-oscillation frequency, which increases with an increase in average input power. Therefore, higher modulation currents are required at higher modulation frequencies. It is also found that as the modulation frequency increases, the minimum pulse width decreases. This is a desirable feature, but it is accompanied by a larger range of frequency shift.

4.1.2 Contact Geometry

Disc Contact

We first consider the case in which the VCSEL operates in a single transverse mode (LP_{01}) throughout the gain-switching process by using a disc contact of $2\text{-}\mu\text{m}$ radius. We fix the modulation frequency at 2.5 GHz, and we examine the effects of carrier diffusion, pumping geometry and multiple-transverse-mode operation. Spatial hole-burning is included in all numerical simulations since it is found to affect the gain-switching dynamics considerably.

The effect of transverse carrier diffusion is studied by comparing the results obtained by using diffusion constants of $30\text{ cm}^2/\text{s}$ and $1\text{ cm}^2/\text{s}$ respectively. The injected current follows Eq. (4.1) with $r_o = 0, r_a = 2\text{ }\mu\text{m}$ and $f_m = 2.5$ GHz. The changes in the pulse width and the frequency shift with modulation index J_m/J_{th} are plotted in Fig. 4.2. Results are shown for the range of modulation indices which corresponds to the regime of stable output pulse trains (one pulse per modulation cycle) as discussed in the previous section. It is found that the main effect of transverse diffusion is to shift the optimal modulation index to lower values. In fact, for a given value of J_m/J_{th} , shorter pulses are obtained when carrier diffusion is taken into account. In short, diffusion facilitates pulsing operation.

To understand the physical origin of this somewhat surprising result, the carrier-density profiles at the peaks of the gain-switched pulses are plotted in Fig. 4.3 for $D = 1$ (dashed) and $30\text{ cm}^2/\text{s}$ (solid). No spatial hole is observed for $D = 30\text{ cm}^2/\text{s}$, whereas a deep spatial hole appears when carrier diffusion is negligible ($D = 1\text{ cm}^2/\text{s}$). This feature suggests that spatial hole-burning affects the gain-switching dynamics. The deep spatial hole for the case of $D = 1\text{ cm}^2/\text{s}$ reduces the overlap between the fundamental LP_{01} mode and the carrier profile. Consequently, the mode sees effectively less gain at a given modulation index for $D = 1\text{ cm}^2/\text{s}$ than for $D = 30\text{ cm}^2/\text{s}$. This feature explains the shift to higher modulation

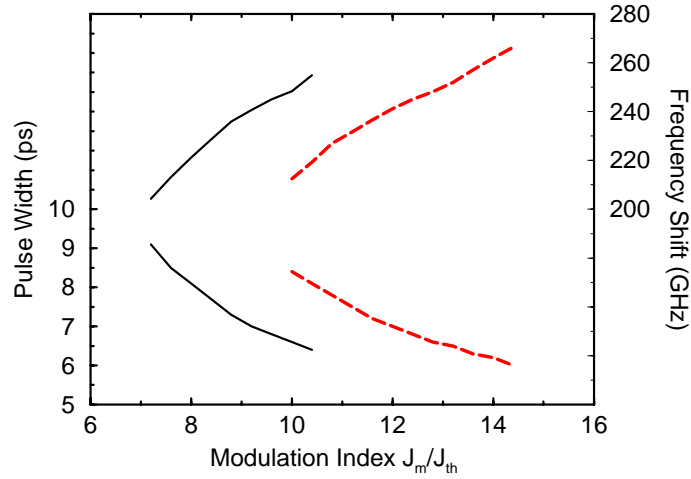


Figure 4.2: Variations of pulse width (lower traces) and frequency shift (upper traces) with modulation index J_m/J_{th} for $D = 30 \text{ cm}^2/\text{s}$ (solid) and $D = 1 \text{ cm}^2/\text{s}$ (dashed). The modulation frequency is 2.5 GHz.

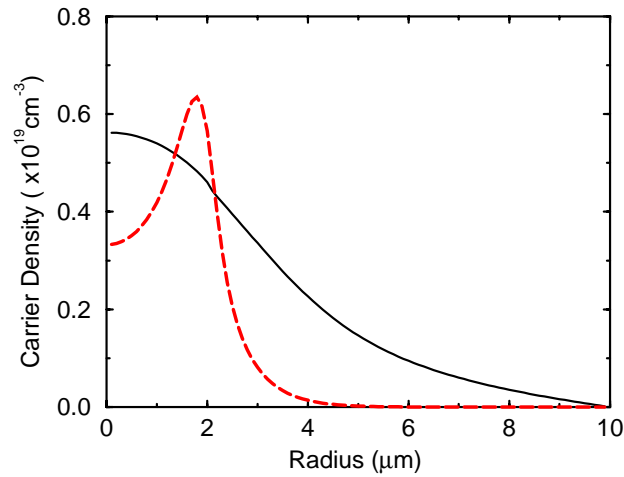


Figure 4.3: Radial carrier-density profiles for $D = 30 \text{ cm}^2/\text{s}$ (solid) and $D = 1 \text{ cm}^2/\text{s}$ (dashed) at the peak of gain-switched pulses. The value of J_m/J_{th} is 10.

indices in the former relative to the latter case. It also illustrates that spatial and temporal effects are coupled in VCSELs through gain saturation, and this spatio-temporal coupling plays an important role in VCSEL dynamics.

Because of the importance of carrier diffusion, the size of the disc contact is likely to be important. Devices with disc-contact radii ranging from 0.5 to 3.5 μm were simulated to answer this question. In all cases, the modulation frequency is fixed at 2.5 GHz, and the modulation index is optimized to produce the shortest pulse. The minimum attainable pulse width and the corresponding frequency shift are plotted in

Fig. 4.4 as a function of the disc-contact radius. A shallow minimum occurs for contact radius in the range 1–2 μm . The optimum range of the contact radius is likely to depend on the size of the index-guiding region, which controls the mode diameter.

To understand the origin of the pulse-width minimum seen in Fig. 4.4, the carrier-density profiles at the peak of the gain-switched pulse are calculated and plotted in Fig. 4.5 for contact radii 0.5–3.5 μm . The results show that the size of the spatial hole burnt in the carrier-density distribution through gain saturation can be controlled by the size of the disc contact. Indeed, there is *no* spatial hole for contact radii 1–2 μm ,

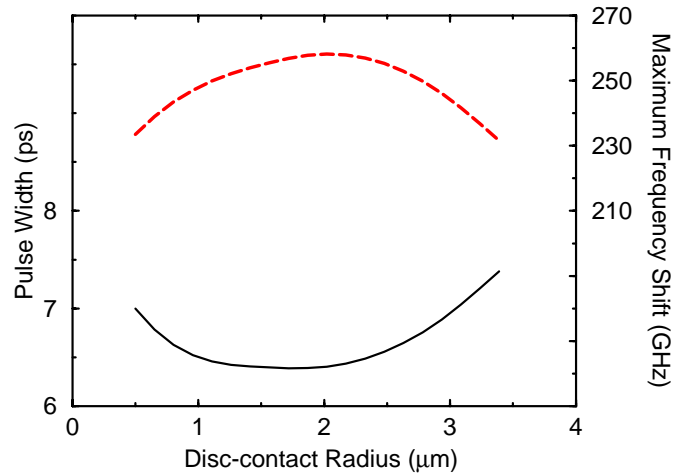


Figure 4.4: Variation of pulse width (solid) and frequency shift (dashed) with disc-contact radius. In all cases, the modulation current is optimized to produce the shortest pulse.

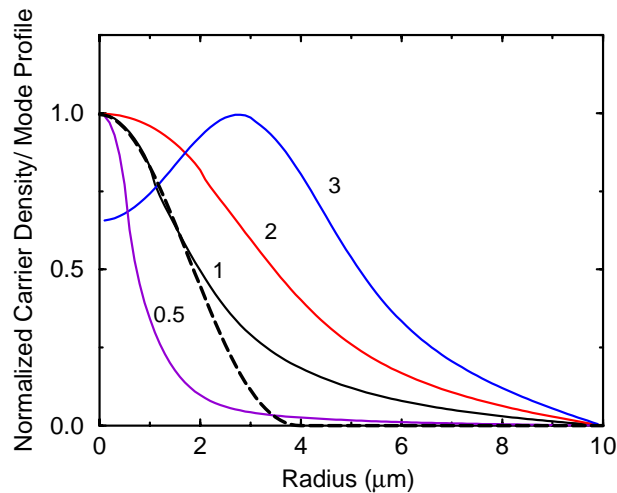


Figure 4.5: Radial carrier-density profiles at the peak of the gain-switched pulse for several disc-contact radii (shown in μm). The dashed line corresponds to the spatial distribution of the LP_{01} mode. The modulation parameters are $f_m = 2.5 \text{ GHz}$, $J_b/J_{th} = 0.95$, and $J_m/J_{th} = 10$.

the range that corresponds to the regime of minimum pulse widths in Fig. 4.4. The spatial distribution of the LP_{01} mode is illustrated by the dashed line in Fig. 4.5. Clearly, the spatial overlap between the mode and the carrier-density profiles is maximized for a contact radius of about $1 \mu\text{m}$. Consequently, carriers are utilized most efficiently, and gain-switching produces the shortest pulse. Although there is no spatial hole for $r_a < 1 \mu\text{m}$, the pulse width increases because of a reduction in overlap.

To conclude, the above results suggest that by reducing the disc-contact area, the effect of spatial hole-burning is reduced. Further, by maximizing the overlap between the mode and carrier-density profiles, the shortest possible pulses are obtained from VCSELs.

Ring Contact

A ring contact is often used in practice to facilitate the emission of laser output from the top mirror. However, its use excites higher-order modes which saturate the gain differently than the fundamental LP_{01} mode, resulting in a different spatial profile for the carrier density. This section discusses how gain-switching characteristics is affected by the use of a ring contact.

A ring contact of an inner radius of $2 \mu\text{m}$ and an outer radius of $4 \mu\text{m}$ is used in numerical calculations. Such a contact preferentially excites the first-order transverse mode. Table 4.2 compares the pulse characteristics such as the minimum width, the corresponding peak power and frequency shift for the two cases of a $2\text{-}\mu\text{m}$ -disc and ring, which correspond to the excitation of LP_{01} and LP_{11} modes, respectively. The modulation index is optimized to give the shortest pulse in both cases. The main feature is that the

Table 4.2: *Comparison of output pulse characteristics for the LP_{01} and LP_{11} modes under single-mode operation.*

Parameter	LP_{01}	LP_{11}
Pumping geometry	0-2 μm disc	2-4 μm ring
Optimal value of J_m/J_{th}	10.4	8.2
Minimum pulse width (ps)	6.4	9.3
Peak power (mW)	132	104
Range of frequency shift (GHz)	254	181

minimum pulse width is larger by about 50% when the LP_{11} mode is the dominant VCSEL mode.

The two transverse modes show significantly different gain-switched output characteristics. This is due to a combination of spatial effects introduced through different pumping geometries (contact areas), and different spatial distributions of the two modes. To understand the difference, the carrier-density and mode-intensity profiles are plotted in Fig. 4.6 for each of the two cases. The optimal modulation index is used in each case. Clearly, the LP_{01} mode has a much better overlap with the carrier-density profile than the LP_{11} mode. This results in gain-switched pulses with a much shorter pulse width.

4.2 Nonlinear Dynamics

Since VCSELs can operate in several transverse modes simultaneously when a wide disc-shaped contact is used, it is interesting to study how the dynamics of gain-switching is affected by mode competition induced by spatial hole-burning. In this section, a $4\text{-}\mu\text{m}$ -radius disc contact is used to excite the LP_{01} and LP_{11} transverse modes. We show through numerical simulations that under two-mode operation, gain-switched VCSELs exhibit complicated nonlinear dynamics, whose origin lies in transverse-mode competition induced by spatial effects, namely spatial hole-burning and carrier diffusion. Similar to the previous section, we investigate the effects of modulation frequency and modulation current.

Gain-switched pulses at modulation frequencies of 2.5, 5 and 10 GHz are shown in Fig. 4.7, and the

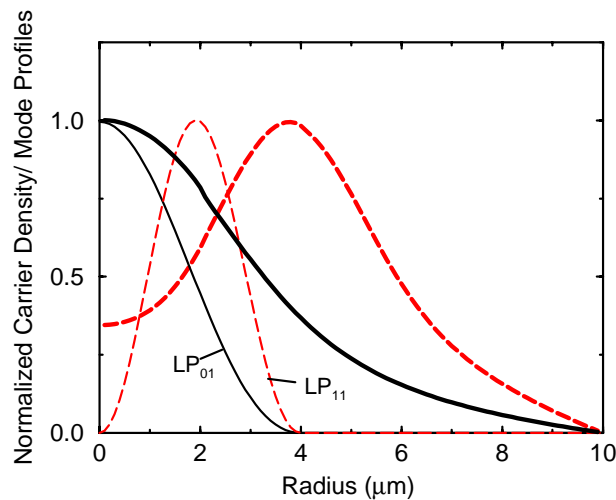


Figure 4.6: Radial carrier-density profiles (bold lines) and spatial intensity distributions (lighter lines) of the modes. The solid lines correspond to the case of a $2\text{-}\mu\text{m}$ radius disc contact, and the dashed lines correspond to that of a $2\text{-}\mu\text{m}$ ring contact with inner and outer radii of 2 and $4\text{ }\mu\text{m}$. The optimal value of modulation index is used in each case.

modulation current is set at $J_m/J_{th} = 15$. Evidently, the details of nonlinear dynamics are strongly dependent on the modulation frequency. The device exhibits period-two oscillations for $f_m = 2.5$ and 10 GHz, and period-six oscillations for $f_m = 5$ GHz. The two transverse modes show quite different dynamics for $f_m = 2.5$ and 5 GHz. The origin of this surprising behavior lies in spatial hole-burning and carrier diffusion. The fundamental LP_{01} mode reaches threshold when the carrier density has recovered fully. However, the spatial hole burnt by it does not get filled completely over the modulation cycle of 0.4 ns at 2.5 GHz, resulting in the excitation of the LP_{11} mode. Since the LP_{11} mode peaks near $r = 2 \mu\text{m}$, its hole burning helps to recover the carrier density near $r = 0$. As a result, the LP_{01} mode is excited during the next modulation cycle, and the process repeats. However, for $f_m = 10$ GHz, output pulses for the two modes exhibit similar period-two dynamics, although the oscillations are 180 degrees out of phase. This anti-phase nature can be understood by noting that each mode burns its own hole in the carrier-density profile which cannot be refilled over a short modulation period of 100 ps. Moreover, the hole burnt by one mode helps to fill the hole burnt by the other mode in the previous modulation cycle, resulting in period-two oscillations.

To investigate the role of transverse-mode competition, we have constructed the bifurcation diagram for the case of 10-GHz gain switching under two-mode operation using J_m/J_{th} as a bifurcation parameter, and the results are shown in Fig. 4.8. The dots (LP_{01}) and crosses (LP_{11}) represent the sampled output peak powers respectively for the two modes at a given value of J_m/J_{th} (Poincaré map). To con-

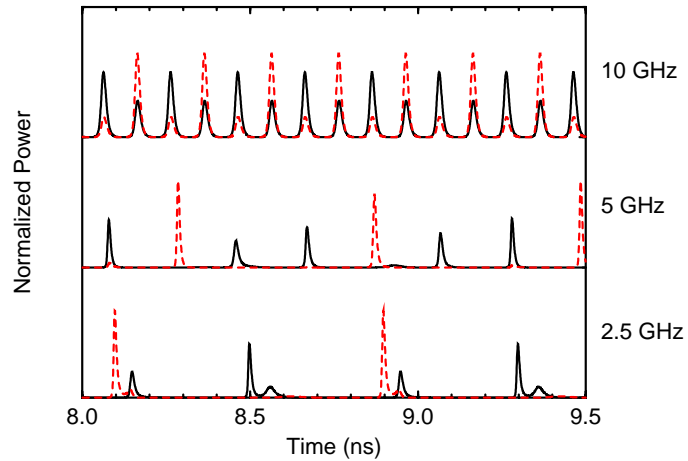


Figure 4.7: Gain-switched pulse trains at modulation frequencies of 2.5, 5 and 10 GHz for a VCSEL operating simultaneously in the LP_{01} (solid trace) and LP_{11} (dashed trace) transverse modes. In all cases, $J_b/J_{th} = 0.95$ and $J_m/J_{th} = 15$.

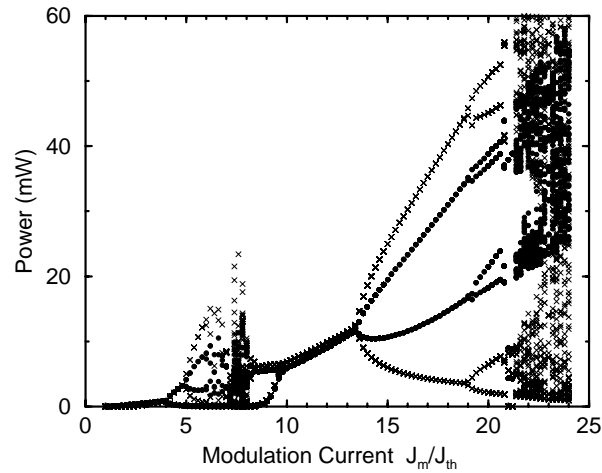


Figure 4.8: Bifurcation diagram as a function of modulation current J_m/J_{th} for 10-GHz gain switching of a VCSEL operating simultaneously in two transverse modes. Dots and crosses correspond to the LP_{01} and LP_{11} modes, respectively.

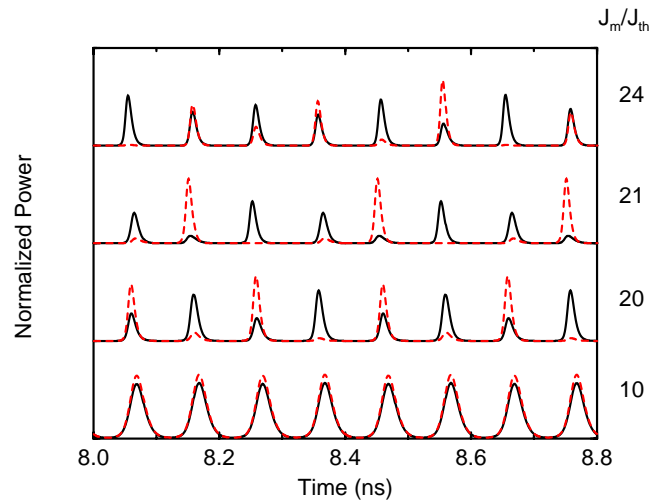


Figure 4.9: Gain-switched pulse trains for four different values of J_m/J_{th} (shown on right margin). Solid and dashed traces correspond to the LP_{01} and LP_{11} modes, respectively.

firm that the origin of chaos is indeed transverse-mode competition, numerical simulations were repeated using the same set of parameters except for a disc-contact radius of $2 \mu\text{m}$, which selectively excites the fundamental LP_{01} mode only. No chaos were observed under identical operating conditions when the VCSEL operates in a single transverse mode.

Pulse trains for 10-GHz modulation for specific values of J_m/J_{th} are shown in Fig. 4.9. For $J_m/J_{th} < 9$, the relaxation-oscillation frequency is smaller than the modulation frequency, resulting in period-doubling behavior and chaos, which are known to occur under such conditions [65]. In the range $9 <$

$J_m/J_{th} < 14$, the two modes oscillate independently with a regular periodic pattern, an example of which is shown for $J_m/J_{th} = 10$ in Fig. 4.9. This regime of operation may find applications in optical data recording, since the two pulse trains can be focused to different spots because of their different spatial patterns. This regime is also useful for optical communications since the two modes are often orthogonally polarized, and therefore can be easily discriminated at the detector. As the modulation current is increased beyond $J_m/J_{th} = 14$, both modes undergo period doubling, as seen in Fig 4.9 for $J_m/J_{th} = 20$. However, the two modes do not oscillate independently and exhibit anti-phase oscillations because of strong mode competition. Eventually, mode competition becomes so strong that chaotic behavior is observed following a period-doubling route. We also observe period-three oscillations, an example of which is shown in Fig. 4.9 for $J_m/J_{th} = 21$.

Since it is known that the nonlinear gain can affect the nonlinear dynamics significantly [66], simulations have been performed for several different values of the nonlinear-gain parameter ϵ_{NL} . Although the single-mode results shown in Figs. 4.1–4.6 remain qualitatively the same, the nonlinear dynamics change considerably with ϵ_{NL} . The variations of output power with time under two-mode operation for three values of ϵ_{NL} are shown in Fig. 4.10. The values of modulation frequency and current are chosen to be $f_m = 10$ GHz and $J_m = 20J_{th}$, respectively. For relatively small values of $\epsilon_{NL} < 0.1 \times 10^{-17} \text{ cm}^3$, the laser output shows period-doubling behaviors, as seen in Fig. 4.10a ($\epsilon_{NL} = 0.01 \times 10^{-17} \text{ cm}^3$) and Fig. 4.10b ($\epsilon_{NL} = 0.1 \times 10^{-17} \text{ cm}^3$). However, the peak powers of the output pulses are reduced as ϵ_{NL}

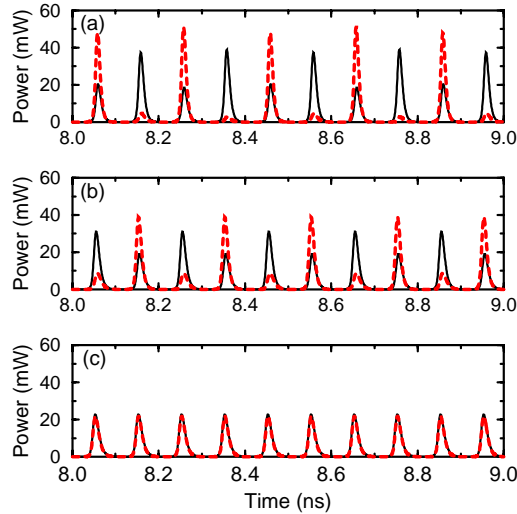


Figure 4.10: Gain-switched pulse trains when the VCSEL operates in two modes under 10-GHz modulation for three different values of ϵ_{NL} : (a) $0.01 \times 10^{-17} \text{ cm}^3$, (b) $0.1 \times 10^{-17} \text{ cm}^3$, and (c) $0.2 \times 10^{-17} \text{ cm}^3$. Solid and dashed traces correspond to the LP_{01} and LP_{11} modes, respectively.

is increased because of gain reduction due to nonlinear-gain-saturation effects. When ϵ_{NL} exceeds a critical value of $\sim 0.1 \times 10^{-17} \text{ cm}^3$, the period-doubling behavior disappears. Fig. 4.10c shows that the laser output consists of regular, periodic pulses at 10 GHz for $\epsilon_{NL} = 0.2 \times 10^{-17} \text{ cm}^3$, and no period-doubling behavior is observed.

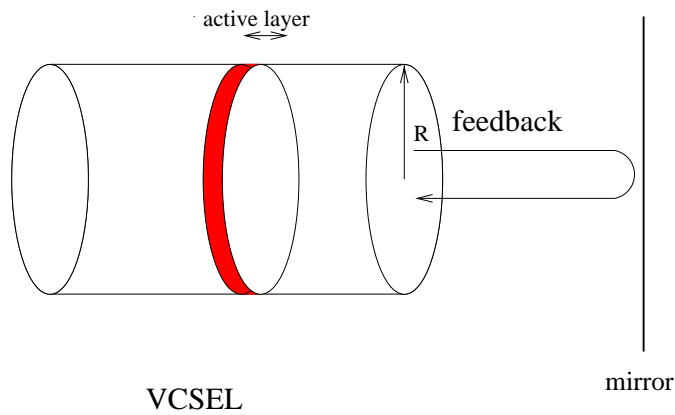


Figure 5.1: *VCSEL in the presence of optical feedback.*

Chapter 5

Optical Feedback Effects

In this Chapter we explore the static and dynamic characteristics of a VCSEL in the presence of optical feedback. We study separately the two cases of a short ($\sim 30 \mu\text{m}$) and long ($\sim 1 \text{ cm}$) external cavity. Section 5.1 presents the rate equations describing the dynamics of a VCSEL with feedback. Section 5.2 considers the practical case of relatively weak feedback such as reflection from a fiber tip or an optical disc for a short external cavity. Section 5.3 studies the change in nonlinear dynamics as well as the associated RIN enhancement for a wide range of feedback values for a long external cavity.

5.1 Rate Equations with Optical Feedback

When light from a VCSEL is focused onto a target such as an optical disc or an optical fiber, some light is invariably reflected back into the laser. Fig. 5.1 shows a VCSEL in the presence of optical feedback, where light is reflected back into the laser by an external mirror. Assuming that the VCSEL can operate in two transverse modes simultaneously ($i = 1, 2$), the modified rate equation describing the evolution of

the field in the presence of optical feedback is given by

$$\frac{dE_i}{dt} = \frac{1}{2}(1 - i\alpha)[G_i(t) - \gamma]E_i + \sum_{m=1}^M \kappa_m E_i(t - m\tau)e^{im\omega_i\tau}. \quad (5.1)$$

The carrier equation is unmodified and is given by Eq. (2.67). Optical feedback through multiple round trips is taken into account by the summation in the last term on the right side of Eq. (5.1) [67]. ω_i is the frequency of the i -th mode under solitary operation, κ_m is the feedback parameter after m external-cavity round trips each of duration τ , and M is the total number of round trips included in the model. In general, cross coupling among different transverse modes should be included. However, cross coupling can be neglected for the two-mode case studied here since the two modes generally have orthogonal polarizations [26]. The parameter κ_m has a form similar to that for edge-emitting lasers [68] and is given by

$$\kappa_m = \frac{1}{\tau_L} \frac{1 - R_2}{R_2} (-1)^{m-1} (\sqrt{R_2 R_{ext}})^m \sqrt{\eta_c}, \quad (5.2)$$

where R_2 and R_{ext} are the output-mirror and external-mirror reflectivities, τ_L is the solitary-laser round-trip time, and η_c is the coupling efficiency of the returned light to the intracavity optical field. In general, η_c can be different for different modes. In this study, the feedback light is assumed to form a one-to-one image of the VCSEL aperture so that $\eta_c = 1$.

Because of high reflectivities of VCSEL mirrors ($R_2 > 99\%$), it is essential to include multiple round trips in the external cavity even for $R_{ext} \sim 1\%$, in contrast with the case of edge-emitting lasers. The number of external-cavity round trips M used in simulations is chosen to be the smallest integer for which $\kappa_M/\kappa_1 < 0.1$. This approximation neglects feedback terms whose power is smaller than 1% of the dominant feedback term. It is useful to define a feedback parameter F_{ext} that corresponds to a single round trip in the external cavity as

$$F_{ext} = \frac{1 - R_2}{R_2} \sqrt{R_2 R_{ext}}. \quad (5.3)$$

We will use this parameter while discussing our numerical results.

The inclusion of the feedback term requires careful reconsideration of the numerical simulation procedure. First, since the optical fields are stored and recalled every external-cavity round trip, the temporal resolution δt cannot be larger than the external-cavity round-trip time τ . It should also be smaller than the desired resolution of 0.1 ps. Further, it must be chosen such that $\tau = s\delta t$ for some integer s , especially for a very short external cavity ($L_{ext} \sim 30 \mu\text{m}$) for which $\tau \sim 0.1$ ps. Second, since feedback is a form

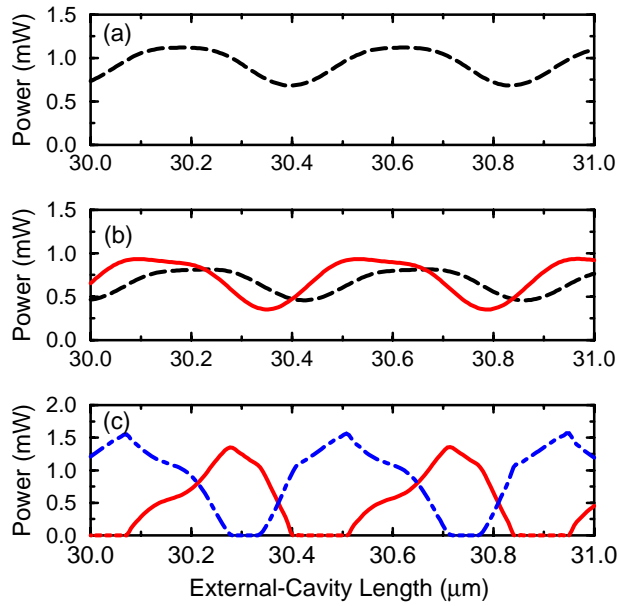


Figure 5.2: Variations of mode power with the external-cavity length. (a) Single-mode operation; two-mode operation with a (b) disc and (c) ring contact. Dashed, solid and dot-dashed traces correspond to the LP_{01} , LP_{11} and LP_{21} modes, respectively.

of memory, the initial conditions should be chosen carefully. For distant reflections ($\tau \gg 1$ ns), the initial conditions can be chosen quite arbitrarily similar to the case of no feedback, since the laser reaches the solitary steady state before any reflected light reaches the laser. However, for near reflections ($\tau \ll 1$ ns), the appropriate initial conditions corresponding to spontaneous noise should be used. In general, it takes longer for the transients to die out under optical feedback conditions, and therefore a longer temporal window of 10 ns is chosen for the following numerical study involving feedback.

5.2 Short External Cavity

In this section we focus on a short external cavity. In practice, this situation corresponds to the case in which a VCSEL is butt-coupled to an optical fiber with a small air gap (~ 10 μm) between the fiber and the VCSEL. We take R_{ext} to be 4%, the typical value of reflectivity from the tip of an optical fiber. Because of 99.5% reflectivity of VCSEL mirrors ($R_2 = 99.5\%$), Eq. (5.3) results in a relatively weak feedback ($F_{ext} \sim 10^{-3}$) even for $R_{ext} = 4\%$. Numerical simulations show that feedback does not destabilize the CW operation of VCSELs for such short external cavities. However, feedback does affect the output powers considerably.

Fig. 5.2a shows the change of CW power with external-cavity length L_{ext} for single-mode (LP_{01})

operation by choosing $R_{ext} = 4\%$ and $\eta_c = 1$. Depending on the feedback phase, the returning field interferes constructively or destructively with the field in the laser cavity, resulting in a periodic change in power with external-cavity length on a wavelength scale. Feedback-induced power variations can exceed 20% of the CW power without feedback.

Results for two-mode operation excited by a disc contact are shown in Fig. 5.2b. At two times above threshold, the output powers without feedback are 0.7 mW for both modes. Mode powers follow a periodic pattern similar to that of the single-mode case, but power variations of the two modes are neither in phase ($\sim 90^\circ$ phase difference) nor sinusoidal. Since the frequency difference between the LP_{01} and LP_{11} transverse modes (~ 150 GHz) corresponds to a small round-trip phase difference of about 10° for $L_{ext} \approx 30 \mu\text{m}$, the phase shift observed in Fig. 5.2b cannot be completely attributed to it. Instead, the origin of the phase difference lies in mode coupling induced by spatial hole-burning. When the power in the one mode is enhanced by feedback, the power in the other mode is slightly reduced due to spatial hole-burning. Since the overlap between the spatial distributions of the LP_{01} and LP_{11} is relatively small, the effects of spatial hole-burning are not very strong. Therefore, the magnitude of change in power is roughly the same as that for the single-mode case.

To study the strong mode-coupling case, calculations are repeated for the case of a ring contact, and results are shown in Fig. 5.2c. Since the spatial distributions of the LP_{11} and LP_{21} overlap strongly, mode competition induced by spatial hole-burning is severe. The enhancement of one mode leads to simultaneous suppression of the other mode to such an extent that the two modes are forced to be out of phase, and this behavior is relatively independent of the absolute value of the feedback phase. Strong mode-coupling also results in a larger change in mode powers compared with the case of single-mode operation (Fig. 5.2a). In particular, one mode can be completely extinguished when the other mode has maximum power. This behavior can be useful in practice since it can be used to select a single transverse mode even though the VCSEL is operating in two transverse modes. By the same token, it suggests that the fiber tip position should remain fixed to a tolerance level below $0.1 \mu\text{m}$ if the objective is to avoid feedback-induced power variations.

To further investigate the effects of spatial hole-burning, the mode powers are calculated for different values of the external reflectivities R_{ext} for two fixed external-cavity lengths. Results for the two cases of $L_{ext} = 30.45 \mu\text{m}$ (left column) and $30.6 \mu\text{m}$ (right column) are plotted in Figs. 5.3, where R_{ext} is varied in the range 0.1%—10%. As expected, the magnitude of power variations increases with the

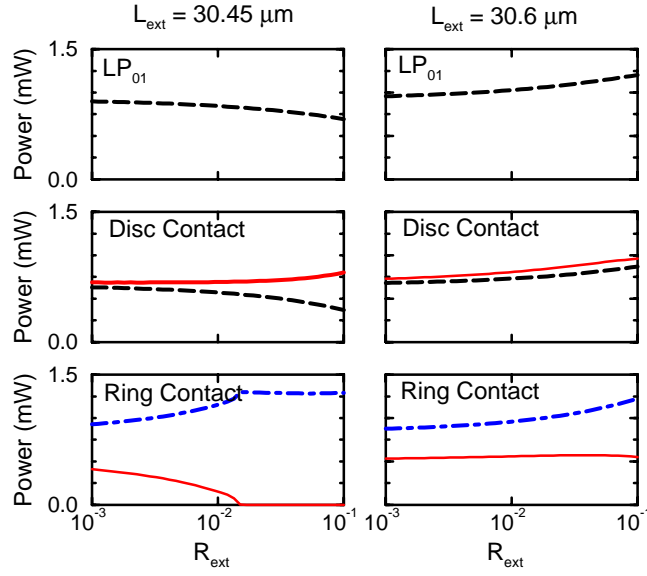


Figure 5.3: Variations of mode power with the external-mirror reflectivity R_{ext} for two different external-cavity lengths. Left column: $L_{ext} = 30.45 \mu m$. Right column: $L_{ext} = 30.6 \mu m$. Dashed, solid and dot-dashed traces correspond to the LP_{01} , LP_{11} and LP_{21} modes, respectively.

amount of feedback. In the absence of mode coupling, both modes are expected to show an identical dependence on R_{ext} as given by the single-mode case (top row of Fig. 5.3) apart from a small phase difference. For two-mode operation, the direction as well as the magnitude of change in power are quite different from those of the single-mode case due to mode coupling induced by spatial hole-burning. This difference is especially pronounced for large feedback values. In particular, for the case of a ring contact, powers in the two modes generally change in different directions as the feedback is increased because of increased mode competition induced by spatial hole-burning. Complete turn-off of the LP_{11} mode occurs for $R_{ext} \geq 3\%$ (lower left of Fig. 5.3).

It is evident from the above discussion that mode competition can lead to an improvement of modal discrimination under appropriate feedback conditions. By utilizing the feedback-phase difference between different transverse modes, the improvement can be enhanced. To investigate this possibility, we have repeated our calculation for the case of two-mode operation under the condition for which the feedback fields of the two modes are out-of-phase after traversing a round trip in the external cavity. This condition can be realized by choosing the external-cavity length according to the following condition (assuming two-mode operation):

$$2\pi\Delta\nu\tau = (2r + 1)\pi, \quad (5.4)$$

where the external-cavity round-trip time is given by $\tau = 2L_{ext}/c$, $\Delta\nu$ is the frequency difference between the two lasing modes, and r is an integer. $\Delta\nu$ is calculated using the standard dispersion relations for a cylindrical step-index waveguide [60]. In the following, the minimum external-cavity length which nearly satisfies Eq. (5.4) is chosen with values $L_{ext} = 500 \mu\text{m}$ ($\Delta\nu \approx 150 \text{ GHz}$) and $380 \mu\text{m}$ ($\Delta\nu \approx 200 \text{ GHz}$) for two-mode operation with a disc and ring contact, respectively. The variations in output power with L_{ext} on a wavelength scale close to these parameter values are shown in Figs. 5.4a and 5.4b, respectively. As expected, the power variations of the two modes with L_{ext} are out-of-phase. However, for the weak-coupling case, the maximum change in power is significantly increased compared with the case of $L_{ext} = 30 \mu\text{m}$ in Fig. 5.2b, and complete suppression of one mode is possible despite the fact that the two modes are only weakly coupled. For the strong-coupling case, mode competition results in single-mode operation over wider intervals of L_{ext} with Fig. 5.2c. These results demonstrate that by choosing an appropriate external-cavity length, feedback can force a two-mode VCSEL to operate in a single transverse mode under both weak-coupling and strong-coupling conditions.

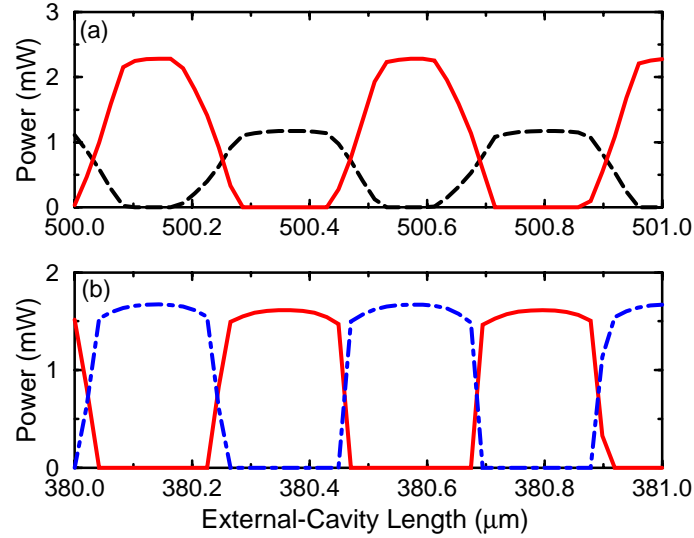


Figure 5.4: Variations of mode power with the external-cavity length under two-mode operation with a (a) disc and (b) ring contact. The feedback phase is chosen according to the out-of-phase condition (5.4). Dashed, solid and dot-dashed traces correspond to the LP_{01} , LP_{11} and LP_{21} modes, respectively.

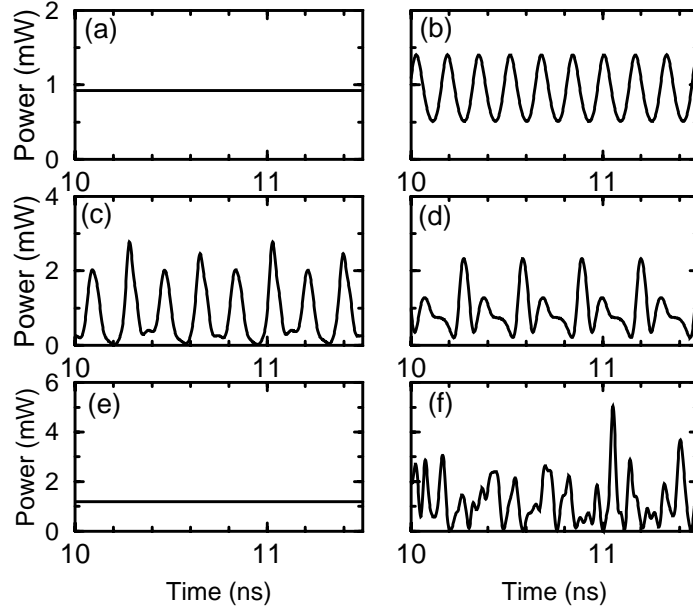


Figure 5.5: Temporal evolution of the output power under single-mode operation for several feedback levels. (a) $F_{ext} = 0$, (b) $F_{ext} = 1.6 \times 10^{-4}$, (c) $F_{ext} = 5 \times 10^{-4}$, (d) $F_{ext} = 8.9 \times 10^{-4}$, (e) $F_{ext} = 1.6 \times 10^{-3}$, and (f) $F_{ext} = 2.8 \times 10^{-3}$.

5.3 Long External Cavity

Since distant reflections can affect the dynamics of semiconductor lasers differently compared with the case of near reflections [59], it is interesting to study the case where the external cavity is relatively long. In practice, this case corresponds to the configuration where the VCSEL light is focused onto a target by a lens. We choose $L_{ext} = 1$ cm and investigate the change in VCSEL dynamics and RIN characteristics associated with the feedback strength F_{ext} . Since the nonlinear dynamics is known to be affected significantly by the nonlinear gain [66], we have included its effect by taking $\epsilon_{NL} = 1 \times 10^{-17}$ cm³.

5.3.1 Single-Mode Operation

This section considers a VCSEL forced to operate in a single transverse mode by using a 2- μ m-radius disc contact. A series of temporal traces showing the output power as a function of time in a 1.5-ns temporal window are shown in Fig. 5.5 for six different values of the feedback parameter. The corresponding the RIN spectra (bold lines) are shown in Fig. 5.6. The temporal traces are obtained with the Langevin noise term left out (no spontaneous emission) to show the feedback-induced nonlinear dynamics without

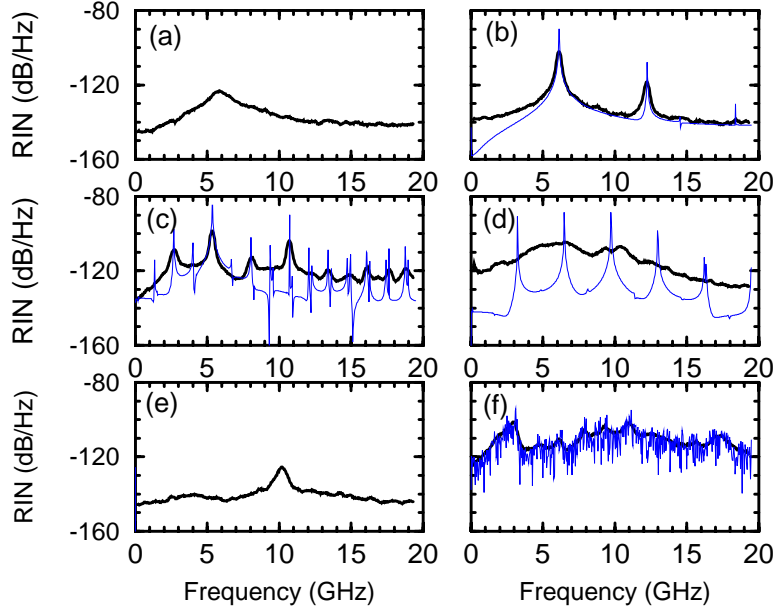


Figure 5.6: RIN spectra (bold lines) under single-mode operation for several feedback parameters corresponding to those used in Fig. 5.5. The light solid lines show the relative-power spectra corresponding to the temporal traces shown in Fig. 5.5 when spontaneous emission is neglected. The feedback levels used are: (a) $F_{ext} = 0$, (b) $F_{ext} = 1.6 \times 10^{-4}$, (c) $F_{ext} = 5 \times 10^{-4}$, (d) $F_{ext} = 8.9 \times 10^{-4}$, (e) $F_{ext} = 1.6 \times 10^{-3}$, and (f) $F_{ext} = 2.8 \times 10^{-3}$.

fluctuations induced by the spontaneous emission noise. The corresponding relative-power spectra are also shown as light traces in Fig. 5.6 for comparison. In Fig. 5.6a and Fig. 5.6e, the relative-power spectrum (without noise) contains only a DC component, and hence the light lines are not visible. Fig. 5.6a shows the RIN spectrum in the absence of feedback ($F_{ext} = 0$). The peak near 6 GHz corresponds to the well-known relaxation-oscillation frequency.

Under weak feedback conditions ($F_{ext} < 1.3 \times 10^{-4}$), the laser retains the stable CW operation, and the RIN spectrum is relatively unchanged, although both the position and the amplitude of the relaxation-oscillation peak change. The increase in the relaxation-oscillation peak amplitude indicates that the optical feedback affects the damping of the relaxation oscillations. Eventually, as the feedback increases, the relaxation oscillations would become undamped at a certain feedback level, and the laser would cease to operate continuously. This scenario is indeed what is found to occur in our numerical simulation. For the VCSEL parameters used in our numerical simulations, the CW state becomes unstable for $F_{ext} > 1.3 \times 10^{-4}$. At $F_{ext} = 1.6 \times 10^{-4}$, the laser exhibits feedback-induced self-pulsations (see Fig. 5.5b) at the relaxation-oscillation frequency. The RIN spectrum therefore shows peaks at the self-

pulsing frequency and its harmonics. With a further increase in F_{ext} , the VCSEL output becomes chaotic following a period-doubling route. As an example, Fig. 5.5c shows period-four oscillations. Interestingly enough, when spontaneous noise is included in the calculations, the RIN spectrum shown as bold lines in Fig. 5.6c corresponds to a period-doubling bifurcation. This result suggests that spontaneous-emission noise does not simply broaden the peaks, but can affect the deterministic nonlinear dynamics significantly. Nonetheless, it is found that the feedback eventually forces the laser to enter the chaotic regime following a period-doubling route. The laser output becomes chaotic for $F_{ext} > 5.5 \times 10^{-4}$.

It is well known that a nonlinear chaotic system may have “windows” in the parameter space in which the chaotic behavior is replaced by periodic or even CW operation. The VCSEL under external feedback is found to be such a nonlinear system. The chaos abruptly ends for $F_{ext} > 8.8 \times 10^{-4}$ and the VCSEL makes a transition to a new CW state. Our results indicate that spontaneous emission affects both the location and the width of the chaotic window. Just after the laser exits the chaotic regime, period-two oscillations with a highly distorted waveform are observed at $F_{ext} = 8.9 \times 10^{-4}$ in the absence of spontaneous emission (see Fig. 5.5d). Although the relative-power spectrum without noise shows a series of peaks at the dominant frequency (about 4 GHz) and its harmonics, a broadly-peaked RIN spectrum is observed with the inclusion of noise (Fig. 5.6d). These results suggest that the inclusion of spontaneous noise changes the dynamics observed in Fig. 5.5d such that the power variations are no longer periodic with time, and the chaotic regime is extended to a larger range of feedback values. Since chaos are known to show sensitive dependence on the initial conditions, it is not surprising that stochastic noise can change the behavior of the laser considerably when operating close to the boundaries of the chaotic regime.

Under strong feedback conditions, it is found that stable CW operation of the VCSEL is possible for a small range of feedback values. Fig. 5.5e shows the CW output occurring at $F_{ext} = 1.6 \times 10^{-3}$. The corresponding RIN spectrum in Fig. 5.6e shows that the relaxation-oscillation frequency is increased by 4 GHz relative to the case of no feedback in this regime. It is not obvious what leads to such a large change in the relaxation-oscillation frequency, since the power increases by only about 30% in Fig. 5.5e, an increase too small to explain the large shift in the frequency. Furthermore, a weak frequency component appears near 4 GHz. The CW state becomes unstable again when F_{ext} exceeds 2.3×10^{-3} and the laser output becomes chaotic as seen in Fig. 5.6f. However, it is found that the laser output enters the chaotic regime via a quasi-periodic route due to the presence of two different frequencies in the system, in contrast with the period-doubling route observed in the first onset of chaos. The mixing and beating of

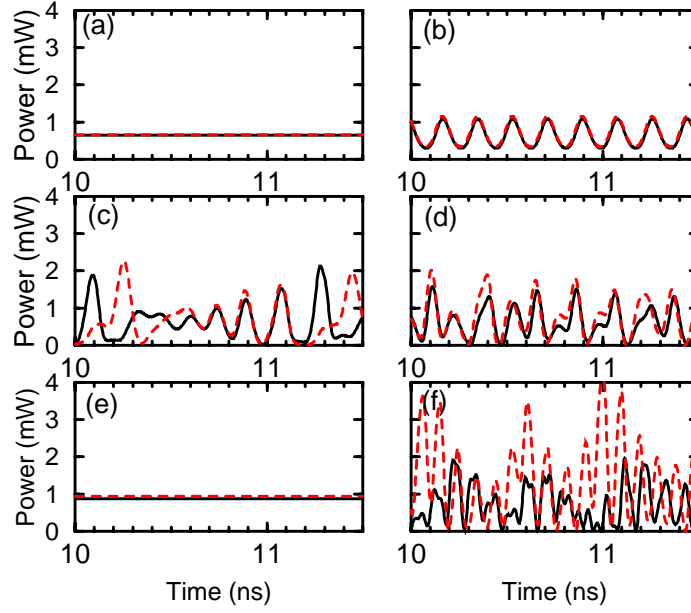


Figure 5.7: Temporal evolution of the output power under two-mode operation with a $4\text{-}\mu\text{m}$ disc contact (weak coupling) for several feedback levels. Solid and dashed lines represent the LP_{01} and LP_{11} modes, respectively. (a) $F_{ext} = 0$, (b) $F_{ext} = 1.6 \times 10^{-4}$, (c) $F_{ext} = 5 \times 10^{-4}$, (d) $F_{ext} = 8.9 \times 10^{-4}$, (e) $F_{ext} = 1.6 \times 10^{-3}$, and (f) $F_{ext} = 2.8 \times 10^{-3}$.

the two frequency components lead to self-pulsations and eventually to chaos. The transition to chaos is responsible for the drastic increase (by > 20 dB) in the RIN seen in Fig. 5.6f. Comparing Figs. 5.6e and 5.6f, we can conclude that the RIN enhancement in this case is solely due to deterministic chaos. Similar RIN enhancements under optical feedback conditions have been observed in edge-emitting lasers [68].

5.3.2 Two-Mode Operation

Weak-Coupling Case

We first consider the weak-coupling case of two-mode operation realized with a $4\text{-}\mu\text{m}$ disc contact. Since the LP_{01} and LP_{11} modes overlap little spatially, they obtain most of the gain from the carrier density at different locations, resulting in weak coupling with nearly the same mode powers. The temporal evolution of the LP_{01} and LP_{11} mode powers are shown by the solid and dashed lines in Fig. 5.7, and the corresponding RIN spectra of the total power are shown in Fig. 5.8. Under weak feedback conditions, the changes in the RIN spectrum with feedback are qualitatively similar to those of the single-mode case. More specifically, an increase in the relaxation-oscillation peak of about 10 dB is observed for $F_{ext} < 1 \times 10^{-4}$. As F_{ext} is increased, feedback results in undamped relaxation oscillations and leads

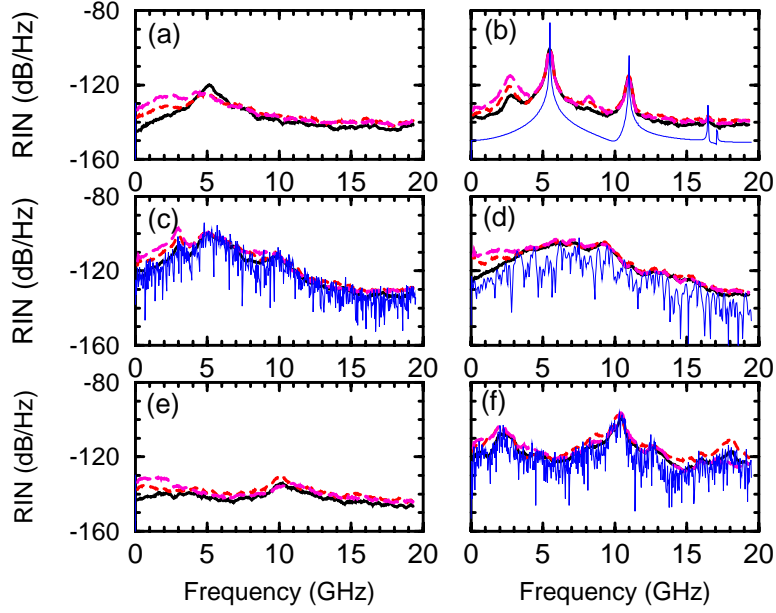


Figure 5.8: RIN spectra for the total power (bold lines), the LP_{01} (short-dashed), and the LP_{11} (long-dashed) under two-mode operation with a $4\text{-}\mu\text{m}$ disc contact. The light solid lines show the relative power spectra corresponding to the temporal traces shown in Fig. 5.7 when spontaneous emission is neglected. The feedback levels used are: (a) $F_{ext} = 0$, (b) $F_{ext} = 1.6 \times 10^{-4}$, (c) $F_{ext} = 5 \times 10^{-4}$, (d) $F_{ext} = 8.9 \times 10^{-4}$, (e) $F_{ext} = 1.6 \times 10^{-3}$, and (f) $F_{ext} = 2.8 \times 10^{-3}$.

to chaos following a period-doubling route. As seen in Fig. 5.7b, both modes oscillate in-phase when the laser enters the self-pulsing regime. However, Fig. 5.7c shows that the chaotic pattern for the two modes are not synchronized. This is not surprising in view of the weak coupling between the two modes, since they can operate independently. A comparison of Fig. 5.5c and Fig. 5.7c shows that weak intermodal coupling leads to an early onset of deterministic chaos, resulting in significant RIN enhancement at a lower feedback level of only $F_{ext} \sim 5 \times 10^{-4}$ compared with the single-mode case. This early onset of chaos is contrary to the lower degree of sensitivity towards feedback for multimode edge-emitting lasers [68]. The difference can be understood in view of the strong coupling among the longitudinal modes in an edge-emitting laser, since these modes generally have identical spatial distributions. These results suggest that the strength of intermodal coupling plays a major role in determining feedback-induced dynamics and the extent of the RIN enhancement. These results for the strong-coupling case discussed below support this conclusion.

Under strong feedback conditions, the VCSEL can enter the CW regime (see Fig. 5.7e), and the RIN spectrum seen in Fig. 5.8e exhibits a relaxation-oscillation frequency near 10 GHz similar to the single-

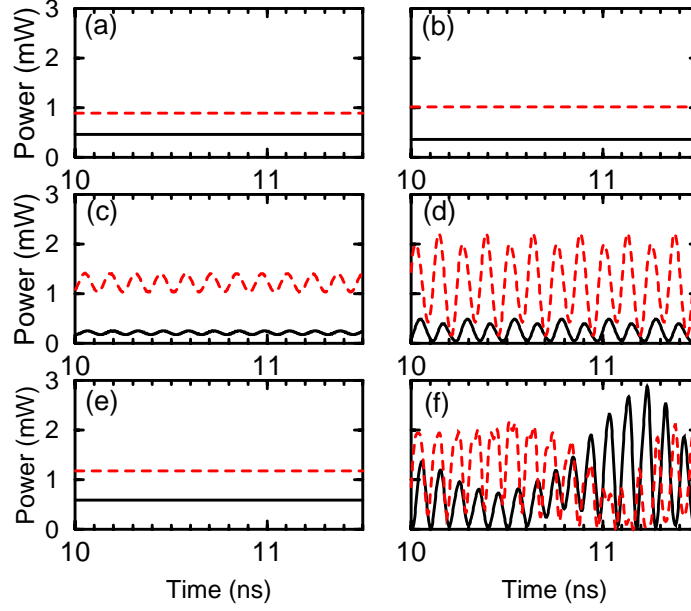


Figure 5.9: Temporal evolution of the output power under two-mode operation with a ring contact (strong coupling) for several feedback levels. Solid and dashed lines represent the LP_{11} and LP_{21} modes, respectively. (a) $F_{ext} = 0$, (b) $F_{ext} = 1.6 \times 10^{-4}$, (c) $F_{ext} = 5 \times 10^{-4}$, (d) $F_{ext} = 8.9 \times 10^{-4}$, (e) $F_{ext} = 1.6 \times 10^{-3}$, and (f) $F_{ext} = 2.8 \times 10^{-3}$.

mode case. Further increase in F_{ext} destabilizes the CW state once again and leads to chaos (Fig. 5.7f). Similar to the single-mode case, the laser enters this second chaotic regime through a quasi-periodic route. The corresponding RIN spectrum shown in Fig. 5.8f exhibits a peak near 2 GHz together with other peaks resulting from the beating of 2-GHz and 10-GHz components. It appears that the 4-GHz peak seen in the single-mode case has been shifted to 2 GHz when the VCSEL operates in two transverse modes.

We have also investigated the effect of optical feedback on the mode-partition noise. The RIN spectra of the LP_{01} and LP_{11} modes are shown in Fig. 5.8 as short-dashed and long-dashed lines for comparison with those of the total power (bold lines). Clearly, mode-partition noise occurs at relatively low frequencies (< 5 GHz) in Figs. 5.8a–e independent of the feedback strength. The amount of RIN enhancement is also relatively unaffected because of weak intermodal coupling and relative independent operation of the two modes. However, mode-partition noise occurs at all frequencies (up to 20 GHz) under strong feedback conditions as shown in Fig. 5.8f.

Strong-Coupling Case

We next consider the strong-coupling case of two-mode operation realized with a ring contact, which

excites the LP_{11} and LP_{21} modes simultaneously. The temporal evolution for the LP_{11} and LP_{21} mode powers at various feedback levels are shown in Fig. 5.9, and the corresponding RIN spectra for the total power are shown in Fig. 5.10. Figs. 5.9 and 5.10 should be compared with Figs. 5.7 and 5.8 (weak-coupling case) and Figs. 5.5 and 5.6 (single-mode case) to see the effect of intermodal coupling. It is found that the onset of self-pulsations and the associated RIN enhancement are delayed to higher feedback values (about 5 times larger) compared with the case of single-mode operation (see Figs. 5.9c and 5.10c). The laser enters the chaotic region at $F_{ext} = 8 \times 10^{-4}$ following a period-doubling route as seen in Fig. 5.9d. However, the RIN enhancement due to the onset of deterministic chaos under strong feedback is reduced by about 10 dB compared with the case of single-mode operation. This reduction in sensitivity towards feedback is attributed to strong intermodal coupling effects. Since the two modes overlap strongly, spatial hole-burning results in strong intermodal coupling such that higher feedback levels are required to destabilize the CW operation of both modes simultaneously. Similar results were obtained in our study of optically injected VCSELs in Chapter 6 indicating that strong intermodal coupling can also reduce the sensitivity of VCSEL towards external injection, in terms of both locking and non-locking aspects.

To investigate mode-partition noise, the RIN spectra for the LP_{11} and LP_{21} modes are also shown in Fig. 5.10 as short-dashed and long-dashed lines, respectively. Under feedback conditions, Figs. 5.10b–f show that the RIN of the LP_{11} mode is larger than that of the total power over a wider frequency range (up to 20 GHz) compared with the case of solitary operation, for which mode-partition noise occurs at relatively low frequencies (< 5 GHz) as seen in Fig. 5.10a. Because of strong mode competition, the power increase of the LP_{21} mode under feedback conditions results in the power decrease of the LP_{11} mode. Consequently, the LP_{11} mode exhibits a much higher RIN due to its lower power. In particular, Fig. 5.10d shows that the power fluctuations in the LP_{11} mode are so strong that both the harmonic and subharmonic components of the dominant 4-GHz component are present in the RIN spectrum.

To summarize the change of feedback dynamics over a wide range of feedback levels, we have constructed the bifurcation diagrams. For each value of F_{ext} , after integrating the rate equations (5.1) and (2.67) over a temporal window of 10 ns to eliminate the transients, the maximum and minimum powers in a subsequent 6-ns temporal window are sampled and plotted. A single point in the bifurcation diagram represents CW operation, two points represent period-one oscillations, and so on. The bifurcation diagrams for single-mode operation and two-mode operation with a disc and ring contact are shown in

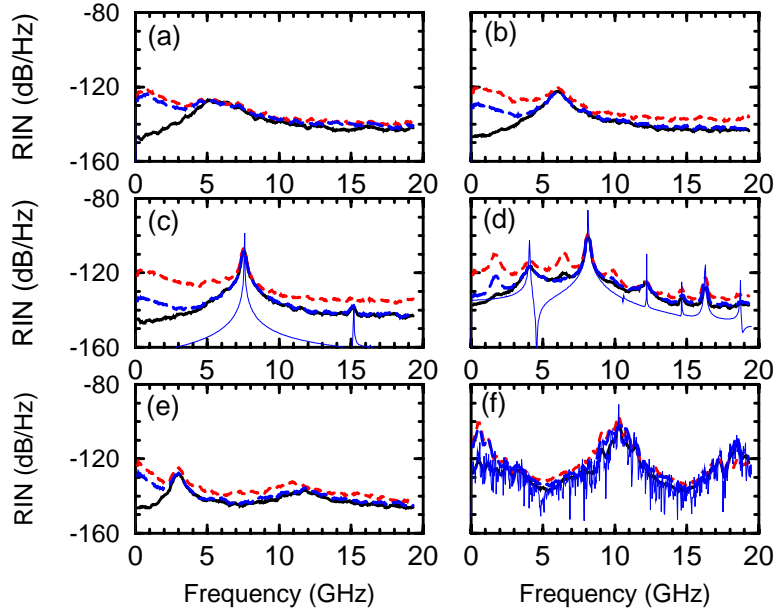


Figure 5.10: RIN spectra for the total power (bold lines), the LP_{11} (short-dashed), and the LP_{21} (long-dashed) under two-mode operation with a ring contact. The light solid lines show the relative power spectra corresponding to the temporal traces shown in Fig. 5.9 when spontaneous emission is neglected. (a) $F_{ext} = 0$, (b) $F_{ext} = 1.6 \times 10^{-4}$, (c) $F_{ext} = 5 \times 10^{-4}$, (d) $F_{ext} = 8.9 \times 10^{-4}$, (e) $F_{ext} = 1.6 \times 10^{-3}$, and (f) $F_{ext} = 2.8 \times 10^{-3}$.

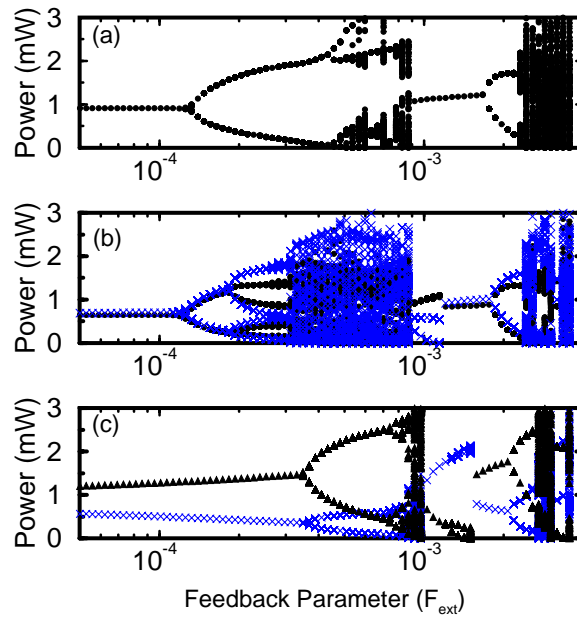


Figure 5.11: Bifurcation diagrams with respect to the feedback parameter F_{ext} for $L_{ext} = 1$ cm. (a) Single-mode operation; two-mode operation with a (b) disc and (c) ring contact. Dots, crosses and triangles correspond to the LP_{01} , LP_{11} and LP_{21} modes, respectively.

Figs. 5.11a–c, with the dots, crosses and triangles representing the LP_{01} , LP_{11} and LP_{21} modes, respectively. Figs. 5.11a–c show clearly the change in dynamics with feedback strength in each case, such as the onset of self-pulsations, the first period-doubling route to chaos, the exit route from the chaotic region, the existence of a CW window, and a second quasi-periodic route to chaos. Although the three cases show qualitatively similar results, the details of the dynamics can be quite different. For example, the VCSEL exhibits richer dynamics under two-mode operation compared with single-mode operation. The strength of intermodal coupling also significantly affects the feedback sensitivity of the laser. Fig. 5.11b shows that weak-intermodal coupling gives rise to an earlier onset of chaos as well as a wider chaotic window compared with Fig. 5.11a, which are attributed to the relatively independent operation of the two weakly-coupled modes. Fig. 5.11c shows that strong intermodal coupling reduces the destabilizing effects of feedback and delays the onset of self-pulsations and chaos. The width of the chaotic window is also much narrower. These results suggest that if feedback insensitivity is the most critical design issue, a ring contact is better than a disc contact.

Chapter 6

Optical Injection

Injection locking of lasers has been a subject of interest for many years. In particular, injection locking of semiconductor lasers remains an important research topic because of its potential for producing compact coherent sources. It is well known that the frequency of a semiconductor laser can be locked to that of the injected signal depending on the power and frequency detuning of the injected signal [23]. Outside this locking regime, interesting nonlinear phenomena such as four-wave mixing [69], period-doubling route to chaos [70], and polarization bistability [71] have been studied.

In this chapter we investigate theoretically the injection dynamics of VCSELs under both single-mode and two-mode operations. Section 6.1 discusses the rate equations in the presence of optical injection. Section 6.2 presents the locking regions obtained from an analytical solution of the spatially independent single-mode rate equations. Section 6.3 discusses the effects of spatial hole-burning and two-mode operation on the locking regimes by comparing the numerical results with the analytical results obtained in Section 6.2 and investigates the possibility of complete suppression of a higher-order transverse mode by injecting the external field into the fundamental mode only. The remainder of Section 6.3 presents the injection dynamics outside the locking range and discusses the change in dynamics associated with two-mode operation due to spatial hole-burning effects.

6.1 Rate Equations with Optical Injection

Optical injection can be taken into account by including an additional term on the right side of Eq. (2.64) [72]. Assuming that the VCSEL can operate in two orthogonally polarized transverse modes, Eqs. (2.64) and (2.67) become

$$\frac{dE_1}{dt} = \frac{1}{2}(1 - i\alpha)[G_1(t) - \gamma]E_1 + \kappa\sqrt{P_{inj}}\exp(-i\Delta\omega t), \quad (6.1)$$

$$\frac{dE_2}{dt} = \frac{1}{2}(1 - i\alpha)[G_2(t) - \gamma]E_2, \quad (6.2)$$

$$\frac{\partial N}{\partial t} = D\nabla_T^2 N + \frac{J}{qd} - \frac{N}{\tau_e} - BN^2 - \frac{1}{d} \sum_{i=1}^2 \Gamma_L v_g g(r, \phi, t) |E_i \psi_i|^2. \quad (6.3)$$

The last term on the right side of Eq. (6.1) accounts for optical injection [23]. P_{inj} is the injected power (in units of photon number), and $\Delta\omega = \omega_{inj} - \omega_0$ is the frequency detuning of the injected signal from the frequency ω_0 of the VCSEL mode under free-running conditions. κ is the injection parameter, which is given by [72]

$$\kappa = \frac{1}{\tau_L} \left(\frac{1}{r_2} - r_2 \right) \sqrt{\eta_{inj}}, \quad (6.4)$$

where $r_2 = \sqrt{R_2}$ is the output-mirror reflectivity, τ_L is the VCSEL round-trip time, and η_{inj} is the coupling efficiency of the injected light to the optical field in the laser. The injection parameter corresponding to the device parameters in Table 2.1 is $\kappa = 1.1 \times 10^{11} \text{ s}^{-1}$. Note that in Eqs. (6.1)-(6.2), the injected field is chosen to be linearly polarized in such a way that it couples only into one of the two modes.

Since no analytical solutions could be found for Eqs. (6.1)–(6.3), we first briefly discuss the analytical theory of injection locking developed for a single-mode semiconductor laser using spatially independent rate equations to gain a basic understanding of VCSEL operation under injection conditions [72].

6.2 Spatially Independent Single-Mode Model

In this section we use a set of spatially independent single-mode rate equations to obtain the range of injection powers and frequency detunings which results in injection locking under single-mode operation. The spatially independent single-mode rate equations presented in Section 2.4 can be modified to include the effects of injection by adding an additional term. The resulting equations are

$$\frac{dE}{dt} = \frac{1}{2}(1 - i\alpha)[G_N(N - N_T) - \gamma]E + \kappa\sqrt{P_{inj}} \exp(-i\Delta\omega t), \quad (6.5)$$

$$\frac{dN}{dt} = \frac{J}{qd} - \frac{N}{T_1} - \frac{1}{V_m}[G_N(N - N_T)]|E|^2, \quad (6.6)$$

We recall that $E(t)$ is the complex field and $|E|^2$ is the photon number, $N(t)$ is the spatially uniform carrier density, and V_m is the mode volume. The locked solutions are obtained by setting the time derivatives to zero in Eqs. (6.5) and (6.6). By writing $E(t)$ as

$$E(t) = \sqrt{P_L} \exp(-i\Delta\omega t - i\varphi_L), \quad (6.7)$$

the locked photon number P_L , the locked phase φ_L , and the corresponding excess carrier density $\Delta N_L = N_L - N_{th}$, where N_{th} is the threshold carrier density [Eq. (2.74)], are given by

$$\begin{aligned} \kappa^2 P_{inj}(\gamma + G_N \Delta N_L) &= [\Delta\omega^2 - \alpha\Delta\omega G_N \Delta N_L + \frac{1}{4}(1 + \alpha^2)G_N^2 \Delta N_L^2] \\ &\quad \times (\gamma P_0 - \Delta N_L/T_1), \end{aligned} \quad (6.8)$$

$$P_L = \frac{\gamma P_0 - \Delta N_L/T_1}{\gamma + G_N \Delta N_L}, \quad (6.9)$$

$$\sin(\varphi_L + \tan^{-1} \alpha) = \frac{-\Delta\omega}{\kappa\sqrt{1 + \alpha^2}} \sqrt{\frac{P_L}{P_{inj}}}, \quad (6.10)$$

where P_0 is the photon number for the free-running laser given by Eq. (2.79). Note that Eq. (6.8) in principle allows for three solutions for each injection condition. Which of these three solutions, if any, are stable is determined by performing a stability analysis. Before doing that, it is useful to note that for a solution for the locked phase φ_L to exist, the absolute value of the right side of Eq. (6.10) must be smaller than one. This criterion provides a necessary condition for locking:

$$|\Delta\omega| \leq \kappa \sqrt{1 + \alpha^2} \sqrt{\frac{P_{inj}}{P_L}}. \quad (6.11)$$

This is also known as the locking range as it indicates the range of frequency detunings for which $(P_{inj}, \Delta\omega)$ -space where injection locking is possible.

A linear stability analysis of the locked solution [Eqs. (6.8)–(6.10)] shows that small perturbations from the steady state change with time as $\exp(z t)$, where z is a solution of the following equation involving a third-order polynomial:

$$z^3 + d_2 z^2 + d_1 z + d_0 = 0 \quad (6.12)$$

with the coefficients:

$$d_2 = \frac{1}{T_1} + G_N (P_L - \Delta N_L), \quad (6.13)$$

$$\begin{aligned} d_1 &= G_N P_L (\gamma + G_N \Delta N_L) + \frac{1}{4}(1 + \alpha^2)G_N^2 \Delta N_L^2 \\ &\quad + \Delta\omega(\Delta\omega - \alpha G_N \Delta N_L) - \left(\frac{1}{T_1} + G_N P_L\right) G_N \Delta N_L, \end{aligned} \quad (6.14)$$

$$\begin{aligned} d_0 &= G_N P_L (\gamma + G_N \Delta N_L) \left[\alpha \Delta\omega - \frac{1}{2}(1 + \alpha^2)G_N \Delta N_L \right] \\ &\quad + \left(\frac{1}{T_1} + G_N P_L\right) \left[\frac{1}{4}(1 + \alpha^2)G_N^2 \Delta N_L^2 + \Delta\omega(\Delta\omega - \alpha G_N \Delta N_L) \right]. \end{aligned} \quad (6.15)$$

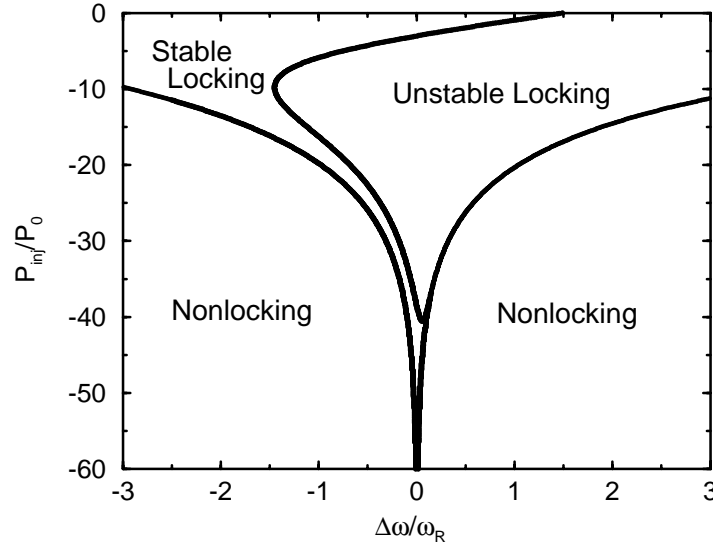


Figure 6.1: Locking regime and stability boundaries in $(P_{inj}, \Delta\omega)$ -space for an optically injected single-mode VCSEL. The relaxation-oscillation frequency of the free running laser is $\omega_R/2\pi = 5$ GHz. Parameters are given in Table 2.1.

According to the Routh-Hurwitz criterion, the following three conditions have to be fulfilled simultaneously in order for a locked solution to be stable [73]:

$$d_2 > 0, \quad d_2 d_1 > d_0, \quad d_0 > 0. \quad (6.16)$$

The Routh-Hurwitz criterion is equivalent to the condition that the real parts of the three roots of Eq. (6.12) are negative for a given possible locked solution to be stable. It turns out that among the three possible locked solutions given by Eqs. (6.8)–(6.10) at most one is stable. One of the solutions represents the “anti-laser” state with a photon number close to zero, and is found to be unstable according to the Routh-Hurwitz condition (6.16). The two other solutions have similar photon numbers, but differ in phase φ_L . One of them is a saddle point with one of the three roots of Eq. (6.12) being real and positive, and this solution should thus be ignored. The remaining solution may or may not be stable depending on the values of P_{inj} and $\Delta\omega$. The three roots of Eq. (6.12) corresponding to this locked solution consist of a complex-conjugate pair (z_1, z_1^*) and a negative real root (z_2) . Upon crossing the boundary between the stable and unstable locking region in the $(P_{inj}, \Delta\omega)$ space, this locked solution exhibits a Hopf bifurcation, i.e. the real part of the complex-conjugate pair becomes positive, and the laser exhibits undamped relaxation oscillations at the frequency given by the magnitude of the imaginary part of z_1 . In Fig. 6.1 we summarize in the parameter space $(P_{inj}, \Delta\omega)$ the various dynamical regions for typical VCSEL pa-

rameters. The two outer curves, almost symmetrically placed with respect to zero detuning, indicate the boundary of the locking regime given by Eq. (6.11), i.e., the region where locked solutions exist. The (asymmetric) inner curve is the stability boundary given by Eq. (6.16). The asymmetry is caused by the linewidth enhancement factor α , which introduces a preference for negative detuning at higher injection powers [23]. In the stable locking region, only one locked solution is stable.

6.3 Numerical Results

Having studied the simple case of single-mode operation without taking into account spatial effects, we now return to the complete model presented in Section 6.1. For two-mode operation, the two transverse modes are assumed to be orthogonally polarized, as often observed experimentally [26]. The bias current is fixed at two times above threshold throughout this study.

6.3.1 Stable Locking Region

We first determine the stable locking region as a function of the injected power P_{inj} and frequency detuning $\Delta\nu = \Delta\omega/2\pi$ by numerically integrating Eqs. (6.1)–(6.3). Stable locking occurs when the operating frequency of the VCSEL is locked to that of the injected signal and the output power becomes constant. In computer simulations, the output power exhibits some fluctuations because of the inherent numerical noise, and we consider stable locking to occur when the time-averaged power fluctuations are smaller than 1% of the average power. Since we are interested in the possibility of turning a two-mode VCSEL into single-mode VCSEL, we choose the injected field to be linearly polarized in such a way that it couples only into one of the two modes. The optically injected mode is chosen to be the fundamental LP_{01} mode for the disc-contact case (LP_{01} and LP_{11}), and the LP_{11} mode for the ring-contact case (LP_{11} and LP_{21}). By comparing the results obtained from numerical simulations and analytical solutions (discussed in the previous section), the effects of spatial hole-burning and intermodal coupling can be analyzed.

Fig. 6.2 presents the results for the three cases of (a) single-mode operation, (b) two-mode operation with two weakly coupled modes (disc contact), and (c) two strongly coupled modes (ring contact). The solid circles show the region of injection locking determined numerically and solid lines show the locking boundaries obtained from the analytical solution of the spatially independent single-mode model discussed in Section 6.2. The injected powers P_{inj} are given in decibels (dB) relative to the free-running

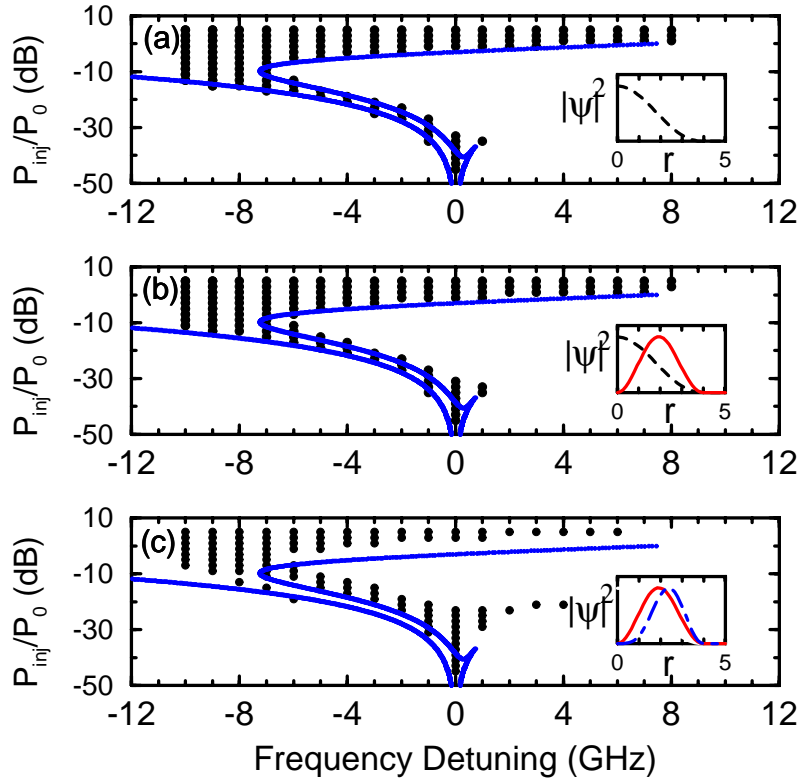


Figure 6.2: *Stable locking regions under injection conditions. Solid circles represent the locking regions obtained numerically, and solid lines show for comparison the stability boundaries of Fig. 6.1. (a) Single-mode operation; two-mode operation with a (b) disc and (c) ring contact. The insets show the radial intensity profiles of the modes in each case, with dashed, solid and dot-dashed traces representing the LP_{01} , LP_{11} , and LP_{21} modes, respectively.*

power P_0 (in units of photon number) of the optically injected mode. Within the range of parameters investigated, it is found that when the optically injected mode is locked to the injected signal, the other mode also shows CW operation due to intermodal coupling introduced by spatial hole-burning. Numerical and analytical results show good quantitative agreement for both single-mode operation (Fig. 6.2a) and two-mode operations with the disc-contact geometry (Fig. 6.2b). The agreement for the single-mode case suggests that carrier diffusion and spatial hole-burning have negligible effects on the injection-locking behavior in single-mode VCSELs. The agreement for two-mode operation with the disc contact is surprising at first sight, but can be understood by noting that the spatial overlap between the LP_{01} and LP_{11} modes is relatively small (see the inset), and hence the intermodal coupling induced by spatial hole-burning is relatively weak. In contrast, for the case of a ring-contact geometry, Fig. 6.2c shows that the locking region is lifted to higher injected powers. This difference can be understood in view of the strong coupling between the LP_{11} and LP_{21} induced by spatial hole-burning (see the inset). Strong coupling is

also responsible for extending the locking regime to the positive-frequency side at relatively low injection powers (< -20 dB).

To answer the question whether injection locking can turn a two-mode VCSEL into a single-mode device, the mode powers are calculated for different values of injection power and frequency detuning while staying inside the locking region. For the weak-coupling case (disc contact), it is found that as the injected power is increased, the power increase in the optically injected LP_{01} mode is accompanied by a simultaneous power reduction of the LP_{11} mode, eventually leading to its complete suppression. For the case of strong intermodal coupling (ring contact), the transition from two-mode to single-mode operation is more abrupt, and occurs right at the lower boundary of the locking region. In both cases, calculations show that under relatively strong injection (> -10 dB), the power carried by the single injection-locked mode is larger than the total power carried by the two modes under free-running conditions plus the additional power supplied by injection. This increase in power is attributed to the decrease in power of the suppressed mode, since the carriers that were used by that mode are available for the dominant mode. Furthermore, the additional increase in single-mode power suggests that in the injection-locked state, the pump is used more efficiently. The main point to note is that, although only one mode is directly coupled to the injected field, the power in the other mode is also significantly affected due to intermodal coupling through the carrier density.

Fig. 6.3 shows the dependence of the quenching power (beyond which one of the two modes is turned off) on frequency detuning. The exact value at which single-mode operation occurs is dependent on the frequency detuning mainly because of the change in the location of boundary of the locking region with detuning. For the weak-coupling case (disc contact), relatively high quenching powers (> -10 dB) are required, and quenching occurs only in the upper stretch of the locking region (Fig. 6.2b). As the frequency detuning is changed from -8 to 0 GHz, the quenching power increases due to the change in location of the upper boundary. In contrast, for the strong-coupling case (ring contact), much lower quenching powers (< -10 dB) are required (Fig. 6.3). Therefore, quenching can occur in both the lower and the upper parts of the locking region (Fig. 6.2c). As the injection-laser frequency approaches the frequency of the free-running mode, the quenching power decreases due to the change in location of the lower boundary. The quantitative difference between the magnitudes of the quenching power for two-mode operations with different contact geometries can be explained intuitively. Since the spatial distributions of LP_{11} and LP_{21} modes overlap much more significantly, spatial hole-burning effects are

stronger, leading to stronger mode competition. Therefore, a relatively small increase in the power of the optically injected mode is adequate to turn off the other mode completely. However, for $|\Delta\nu| < 1$ GHz, quenching is no longer possible in the lower locking region (< -20 dB), and the quenching power increases significantly (> 2 dB) since quenching has to occur in the upper region of Fig. 6.2c.

The above analysis can be extended to the multimode case, and a similar behavior is expected. In essence, injection increases the power in the optically injected mode, which simultaneously suppresses the power in the other modes due to mode competition induced by spatial hole-burning. The amount of suppression depends critically on the strength of spatial hole-burning, injected power, and frequency detuning.

6.3.2 Non-locking Region

Besides considering the practical importance of injection locking, it is also interesting to investigate the dynamics outside the locking region. We first study the dynamics inside the non-locking region where no locked solution exists (Fig. 6.1). The injection power is chosen to be -27 dB and the temporal traces are obtained for different frequency detunings. At a relatively large detuning ($|\Delta\nu| > 7$ GHz), oscillations are close to being purely sinusoidal. For the case of two-mode operation, the two modes

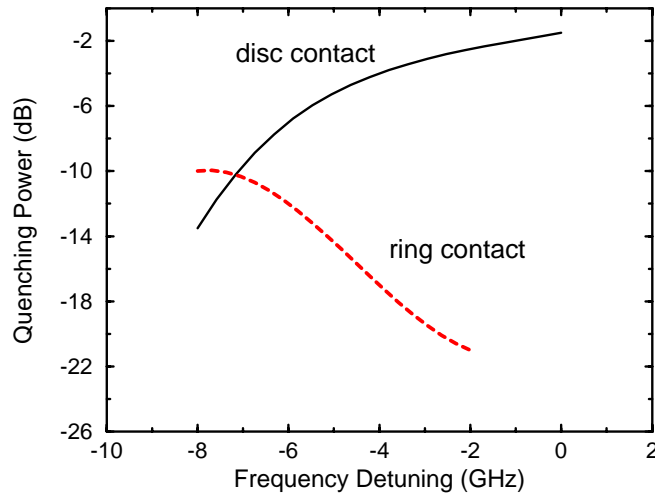


Figure 6.3: Change in quenching power with frequency detuning inside the stable locking region for the disc-contact and ring-contact geometries, respectively.

oscillate in phase sinusoidally. Figs. 6.4 and 6.5 show the temporal traces at an injected power of -27 dB and frequency detunings of -5 and -3 GHz, respectively. Results for single-mode operation and two-mode operations with a disc and a ring contact are presented in a–c respectively of Figs. 6.4 and 6.5. In Figs. 6.4 and 6.5, as the magnitude of the frequency detuning is decreased, generation of new frequency components through wave-mixing processes become more efficient, resulting in harmonic distortions. Moreover, the oscillation amplitude is enhanced when the frequency detuning approaches the relaxation-oscillation frequency (5 GHz under free-running conditions). However, for two-mode operations, the behaviors of individual modes are quite different. As the frequency detuning is changed from -5 to -3 GHz, harmonic distortions are accompanied by an increasing phase shift between the two modes because of more efficient wave mixing and stronger mode competition (Figs. 6.4b-c and 6.5b-c). For the strong-coupling case (ring contact), mode competition is so intense that the power oscillations in the two modes are almost anti-correlated (Fig. 6.5c). Further, the peak-to-peak power variations as well as the amount of harmonic distortions are small compared with the disc-contact case. Evidently, strong spatial hole-burning between the two highly overlapping modes results in significant intermodal coupling so that the effective strength of the injected field seen by the VCSEL is reduced, resulting in reduced harmonic distortions.

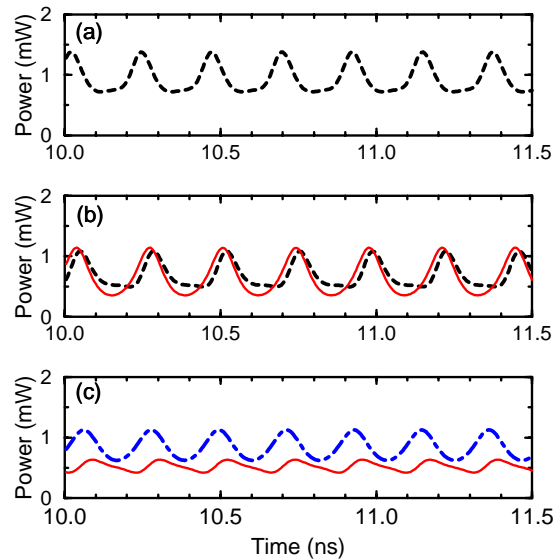


Figure 6.4: VCSEL dynamics in the non-locking region. Temporal traces in a 1.5-ns temporal window at an injected power of -27 dB and a frequency detuning of -5 GHz. (a) Single-mode operation; two-mode operation with a (b) disc and (c) ring contact. Dashed, solid, and dot-dashed traces represent the LP_{01} , LP_{11} , and LP_{21} modes, respectively.

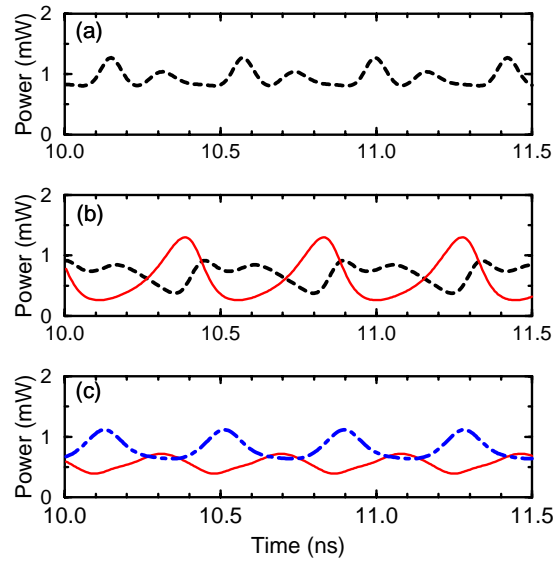


Figure 6.5: Operation conditions same as those of Fig. 6.4 except for a -3 GHz frequency detuning.

6.3.3 Unstable Locking Region

Since qualitatively different dynamical behaviors are possible inside the non-locking and unstable locking regions [69], we also studied the dynamics inside the unstable locking region (Fig. 6.1). To investigate the change in dynamics as one approaches the boundary between the unstable locking region and the non-locking region (Fig. 6.1), temporal traces are computed for injection powers of -5 , -10 , -15 and

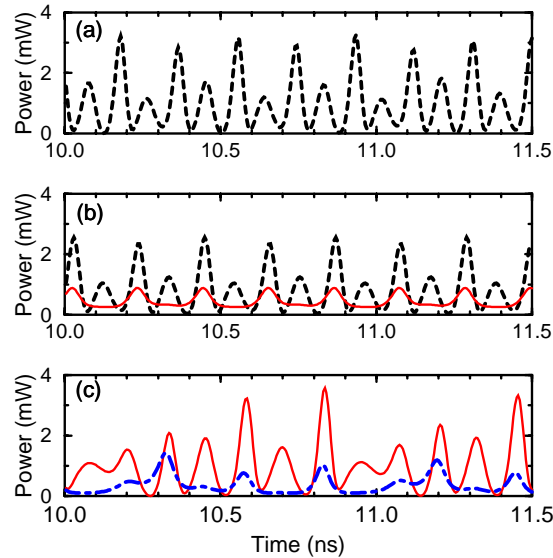


Figure 6.6: VCSEL dynamics in the unstable locking region. Temporal traces in a 1.5-ns temporal window at an injected power of -10 dB and a frequency detuning of 5 GHz. (a) Single-mode operation; two-mode operation with a (b) disc and (c) ring contact. Dashed, solid and dot-dashed traces represent the LP_{01} , LP_{11} , and LP_{21} modes, respectively.

–20 dB at a fixed frequency detuning of 5 GHz. For the single-mode case, it is found that the device exhibits sinusoidal oscillations well inside the unstable locking region ($P_{inj}/P_0 = -5$ dB). However, as one approaches the boundary between the unstable locking and non-locking regions, period-four oscillations ($P_{inj}/P_0 = -10$ dB) and quasi-periodic behaviors ($P_{inj}/P_0 = -15$ dB) are observed. When one crosses the boundary, the quasi-periodic behavior disappears, and period-one and sinusoidal oscillations are observed ($P_{inj}/P_0 = -20$ dB). Qualitatively similar results are obtained for two-mode operations. However, for the strong-coupling case (ring contact), chaos occur at a higher injection power of ~ -10 dB. Fig. 6.6 illustrates one set of the temporal traces inside the unstable locking region at a frequency detuning of 5 GHz and an injected power of -10 dB. The device exhibits period-four oscillations under single-mode operation (Fig. 6.6a) and the weak-coupling case (Fig. 6.6b), whereas a quasi-periodic behavior is observed for the strong-coupling case (Fig. 6.6c). These results again suggest that strong intermodal coupling makes the VCSEL less sensitive to external injection.

We have repeated our calculations with the inclusion of nonlinear-gain effects by choosing $\epsilon_{NL} = 1 \times 10^{-17}$ cm³. It is found that the stable locking regions become slightly wider compared to the case when nonlinear-gain effects are neglected. However, nonlinear-gain effects do not change the qualitative nature of the VCSEL dynamics obtained above.

Chapter 7

Experimental Results

In this chapter we present the experimental results obtained in our laboratory. The objective is to explore the effects of multiple-transverse-mode operation on VCSEL performance. Section 7.1 describes our experimental setup used for studying VCSEL emission characteristics. Our study is divided into two parts. Section 7.2 focuses on the study of CW operation without feedback and investigates the emission characteristics used to characterize the performance of a VCSEL: (i) L-I, (ii) spectral, (iii) spatial, and (iv) RIN characteristics. Section 7.3 explores these characteristics under optical feedback conditions. The device investigated is a high-speed fiber-optic VCSEL packaged in a metal can with a flat window, and is provided by Honeywell.

7.1 Experimental Setup

The experimental setup for studying VCSEL characteristics under optical feedback conditions is shown in Fig. 7.1. For studying CW operation without feedback, light in the feedback arm was blocked. Light from the VCSEL was collimated by a lens (focal length $f_1 = 4$ mm) and focused by another lens (focal length $f_2 = 6.29$ cm) onto a mirror. The output facet of the VCSEL and the external mirror constituted the external cavity, whose length was about 29 cm. This point-focus configuration had the advantage that the effect of beam walk-off introduced by an unintentional tilt of the mirror was relatively small, since the external mirror was placed at the focus. By carefully adjusting the tilt of the mirror and the position of the focusing lens, the reflected light was coupled back into the laser cavity. To minimize unintentional reflections introduced by the collimating lens in front of the VCSEL, the collimating lens was oriented such that the face with a smaller radius of curvature faced the laser. A 50/50 non-polarizing beam splitter was inserted in the beam as shown to divert 50% of the light out of the external cavity

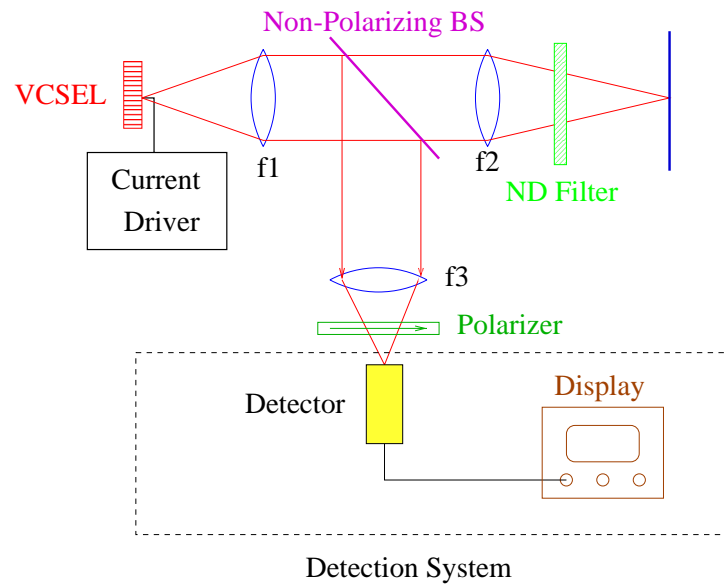


Figure 7.1: *Experimental setup for measuring VCSEL emission characteristics.*

for detection purposes. A non-polarizing beam splitter was used to avoid introducing mode-dependent losses into the system, since different modes were generally linearly polarized in different directions. A polarizer was inserted before the detector to select the power at orthogonal polarizations. The two different polarization angles were selected such that one polarization state corresponded to maximum transmission of the polarizer near threshold. The other orthogonally polarized state was selected by rotating the polarizer by 90° . Different detection systems were used to measure the static, spectral, spatial, and noise characteristics, as detailed below along with the results of the corresponding measurements.

Since temperature control was critical for stable performance, the VCSEL was mounted on a heat sink (metal base with fins) with thermo-electric coolers sandwiched in between. A thermally conductive gel was used to ensure good thermal contact between the interfaces. A thermistor was physically attached to the heat sink and electrically connected to a Lightwave LDT 5412 temperature controller, which provided an electrical feedback signal to the coolers to achieve stable temperature control. The operating temperature in this study was chosen to be 20°C .

7.2 CW Operation without Feedback

7.2.1 L-I Characteristics

A power meter (Liconix model 45PM) was used for measuring the L-I characteristics. The current was modulated sinusoidally at 5 Hz, and the L-I curve was obtained by displaying the detected power (Y-axis)

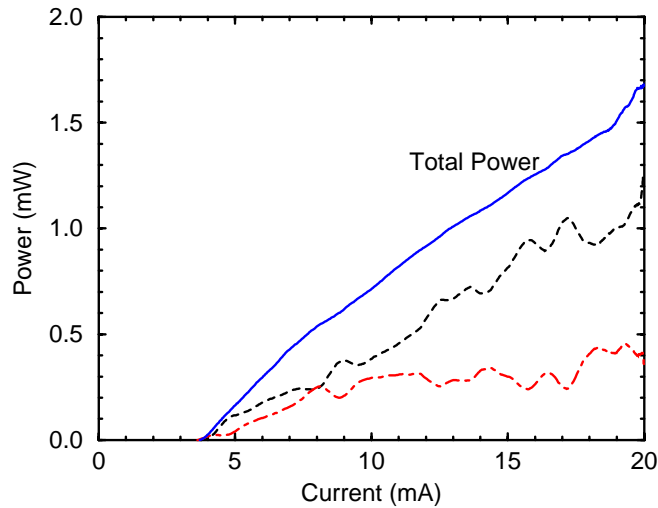


Figure 7.2: *L-I characteristics for the total power (solid line) and for the two orthogonally polarized components selected by rotating the polarizer to 300° (dashed) and 210° (dot-dashed).*

and the current (X-axis) simultaneously on an oscilloscope (LeCroy model 9410, 150MHz). Fig. 7.2 shows the L-I curves for the total power and powers carried by the two orthogonally polarized components at polarization angles of 300° and 210° . Although the L-I curve for the total power was found to be nearly linear with a threshold of 4 mA, the L-I curves for the orthogonally polarized components showed significant oscillations. A possible cause for these oscillations or kinks is multiple-transverse-mode operation of the VCSEL [36]. Studies have also shown that interference effects caused by the reflection at the interface between the substrate and the air can lead to resonances of the L-I curves [41]. The absence of such oscillations in the L-I curve for the total power rules out this possibility. To further investigate the characteristics of the transverse modes, measurements were performed in both the spatial and frequency domains. Since different transverse modes have different spatial distributions as well as different optical frequencies, useful information can be extracted by looking at the near-field characteristics and the optical spectra.

7.2.2 Spectral Characteristics

A Hewlett-Packard optical spectrum analyzer was used to measure the spectral characteristics. Light was focused by a microscope objective onto the fiber (typical coupling efficiency was about 20%). The fiber, which was connectarized at the other end, was connected directly to the input of the optical spectrum analyzer to obtain the optical spectrum. The optical spectra for the total power at four values of the injection

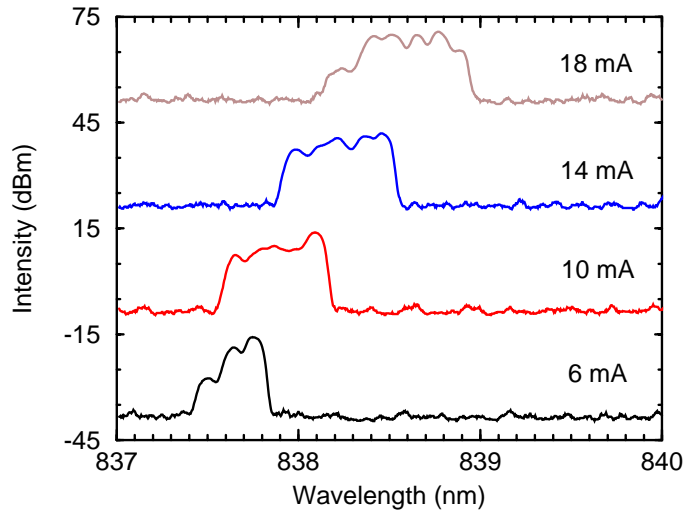


Figure 7.3: Measured optical spectra for the total power for several values of the injection current.

current are shown in Fig. 7.3. Successive traces are displaced by +30 dBm for clarity. The resolution of the optical spectrum analyzer used for obtaining these traces was 0.1 nm (a frequency resolution of about 40 GHz for $\lambda \approx 840$ nm). Since the typical linewidth of a transverse mode is < 1 GHz, individual modes could not be resolved, resulting in a continuous, broad optical spectrum shown in Fig. 7.3. The broadening of the optical spectrum with increasing current indicated the onset of higher-order transverse modes. Since the typical frequency separation between neighboring transverse modes is about 100 GHz (~ 0.2 nm), the optical spectra indicates that the VCSEL operates in about 2–5 transverse modes depending on the injection current. The optical spectra of the orthogonally polarized components were found to be quantitatively similar. With a limited resolution of 0.1 nm, it was not possible to identify the polarization of individual transverse modes.

Fig. 7.3 also shows a red shift of the spectra with increasing current at an average rate of ~ 0.08 nm/mA because of the change in refractive index associated with heating. Since the longitudinal-mode frequency ν depends on the refractive index n according to Eq. (2.24), the optical spectrum shifts as the device heats up and the refractive index increases.

7.2.3 Near-Field Characteristics

A Panasonic video camera was used to observe the two-dimensional near-field characteristics. Light was focused by a lens onto a piece of white card and its image displayed on a monitor using the video camera. We observed that the two-dimensional near-field profile consisted of a number of mixed modes depending

on the current, and it was not perfectly radially or azimuthally symmetric. Two typical two-dimensional profiles taken with a Tektronix camera are shown in Fig. 7.4 for the two orthogonally polarized components at a current of 14 mA. Clearly, both profiles are close to circular, which is a characteristic of VCSELs. However, qualitatively different spatial patterns were observed at orthogonal polarizations. The top figure shows a central bright spot at 300° whereas the bottom figure shows a dim doughnut-shaped profile at 210° . The brightness reflects the relative amount of power carried by each mode. Because of the limited resolution of both the monitor and the video camera, the intensity variations across the beam were not easily discernible.

In order to better quantify our results, a CCD array was also used to measure the near-field profile along one transverse (horizontal) dimension. A slit was put in front of the CCD array to obtain a narrow slice of the near-field profile. Since the VCSEL aperture was quite small (diameter of $\sim 12 \mu\text{m}$), its image was magnified such that its dimension was much larger than the dimension of a single detector cell in the CCD array ($25.4 \mu\text{m}$). A magnification of about 250 was achieved by using two lens with focal lengths $f_1 = 4 \text{ mm}$ and $f_3 = 1 \text{ m}$ respectively, and the image of the laser output spanned about 120 CCD cells.

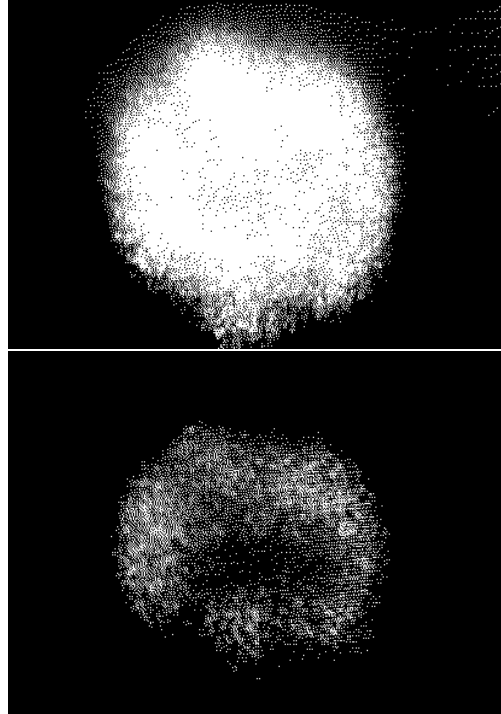


Figure 7.4: Two-dimensional near-field profiles for the orthogonally polarized components at 300° (top) and 210° (bottom).

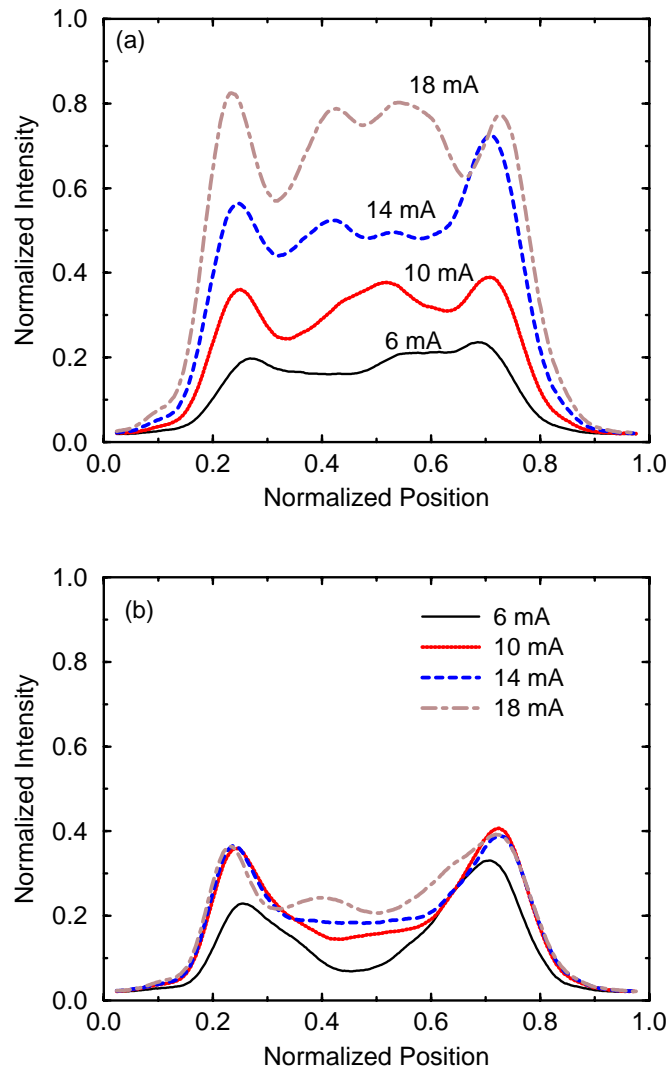


Figure 7.5: One-dimensional near-field profiles at several values of the injection current for the orthogonally polarized components at (a) 300° and (b) 210° .

A series of one-dimensional near-field profiles taken at different injection currents are presented in Fig. 7.5 for the orthogonally polarized components. The two sets of traces were normalized with identical scaling factors to allow the comparison of relative powers. At 6 mA, a doughnut-shaped pattern (possibly LP_{11}) was observed at a polarization angle of 210° , whereas a central bright spot (LP_{01}) was observed at a polarization angle of 300° . As the current was increased, an outer ring appeared at 300° due to the onset of another higher-order transverse mode. This higher-order ring mode appeared in a polarization direction of 300° in order to minimize the overlap with the other ring mode at 210° , so that the gain was better utilized. The appearance of this higher-order ring mode is also responsible for the first kink

observed in the L-I curve. In Fig. 7.2, the L-I curves of the orthogonally polarized components show an approximately linear relation until the current reaches about 8 mA, when the first kink occurs. More kinks are present at higher currents because of the onset of other higher-order transverse modes.

7.2.4 RIN Characteristics

A high-speed photoreceiver (New Focus model 1537) was used to measure the intensity-noise characteristics. The photoreceiver consisted of a built-in amplifier (amplifier gain 128 mV/mW at 1 GHz and 1.06 μm) and a high-speed detector (bandwidth 6 GHz). The output signal was displayed on a spectrum analyzer (Hewlett Packard model 8593E, bandwidth 9 kHz–22 GHz). Similar to the case of multiple-longitudinal-mode operation in edge-emitters, one other consequence of multiple-transverse-mode operation is the RIN enhancement of individual modes because of mode partition [59]. Numerical results presented in Section 3.2 show that the mode-partition noise characteristics can be quite different from that of edge-emitting lasers depending on the spatial distributions of the transverse modes. To investigate mode-partition noise, we measured the low-frequency RIN spectrum of the orthogonally polarized components. The intensity-noise spectra obtained from the spectrum analyzer were normalized with respect to the output power to obtain the RIN defined in Eq. (3.6). Since mode-partition noise occurred at low frequencies, we focused on measuring the low-frequency RIN.

The RIN spectra in the frequency range 0–600 MHz are presented in Fig. 7.6 for the polarization

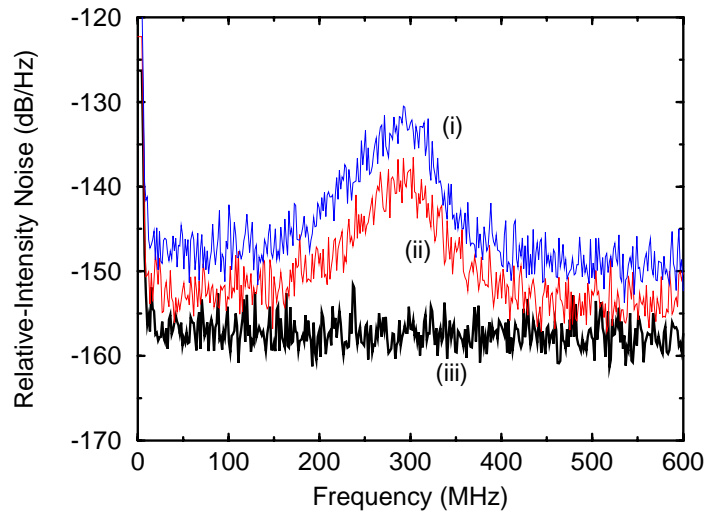


Figure 7.6: RIN spectra at 11 mA for the orthogonally polarized components at (i) 210°, (ii) 300°, and (iii) for the total power.

component at (i) 210° , (ii) 300° , and (iii) for the total power. At the chosen injection current of 11 mA, the output powers for the three cases were: (i) 0.3 mW, (ii) 0.5 mW, and (iii) 0.8 mW, and the resolution bandwidth was set at 3 MHz. The DC peak was introduced by the local oscillator in the spectrum analyzer and was unrelated to the laser output. Clearly, Fig. 7.6 shows that the RIN of either orthogonally polarized component is higher than the RIN of the total power, and the enhancement of the RIN peak is about 25 dB, which agrees quantitatively with the numerical results presented in Section 5.6. The polarization component at 210° shows a higher RIN because of its lower power, and the peak value of -130 dB also shows good quantitative agreement with theory. It should be noted that the RIN of the total power was limited by the sensitivity of the detector used, i.e., it corresponded to the noise floor of the detector.

Qualitatively similar noise characteristics were observed over a wide current range when several transverse modes were present, and the location of the peak near 290 MHz seen in Fig. 7.6 remained relatively unchanged. However, no peak was seen for currents smaller than 8 mA. It appears that the presence of two highly overlapping doughnut modes in both polarization components leads to strong carrier competition (see Fig. 7.5) and results in the RIN enhancement seen in Fig. 7.6.

7.3 Effects of Optical Feedback

Next, we studied the effect of optical feedback on the low-frequency RIN spectrum of the orthogonally polarized modes. The maximum attainable feedback power ratio before light entered the laser facet is estimated to be 25% (-6 dB) due to double pass through the 50/50 beam splitter. Additional attenuation of the feedback power was introduced by inserting neutral-density filters in the feedback path.

Under strong feedback conditions (-10 to -6 dB), the RIN spectrum was found to change with time (roughly on a sub-second scale), and no steady-state was reached. This observation suggests that the laser output exhibits temporal instability under optical feedback conditions. A representative snapshot of the RIN spectrum is shown in Fig. 7.7. Interestingly, three distinct peaks are present near 35 MHz, 440 MHz, and 510 MHz, and a weak peak is present at 475 MHz. Clearly, the peak at 510 MHz corresponds to the external-cavity round-trip frequency for an external-cavity length of 29 cm. The appearance of other frequency components which are not harmonics of each other is an evidence of a quasi-periodic route to chaos, for which chaos arise from the beating and mixing of different frequency components in the system. For example, the 440 MHz component results from the mixing of the second harmonics of the 510 MHz and 290 MHz components, and the 35 MHz peak arises from the mixing of the 440 MHz and

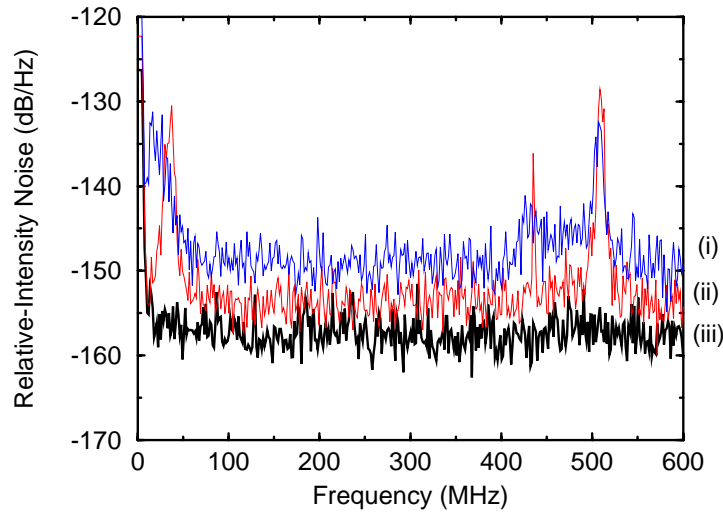


Figure 7.7: RIN spectra at 11 mA with optical feedback (-6 dB). (i) The orthogonally polarized components at 210° , (ii) 300° , and (iii) the total power.

475 MHz components. The frequency-mixing process generates new frequency components and leads to chaos. Note that these components are absent in the RIN spectrum for the total power [curve (iii) in Fig. 7.7]. Fig. 7.7 showed only the dominant frequency components present in the system, and many more weak components are expected to be present. However, such components were too weak to be identified on the spectrum analyzer.

At moderate feedback levels (-60 to -10 dB), it was found that the RIN spectrum exhibited a dominant peak near 280 MHz. Similar to the behavior observed under strong feedback conditions, the spectrum was found to be temporally unstable. Under very weak feedback conditions (< -60 dB), optical feedback had no observable effects on the RIN spectrum. We did not observe any significant rise in the noise floor for all feedback levels investigated (-80 to -6 dB).

The effects of optical feedback on the L-I curves and the spatial and spectral characteristics were also investigated. It was found that the change in mode powers was quite small ($< 10\%$) for all feedback levels explored, and the spatial and spectral characteristics remained largely unaffected.

In summary, our experimental results demonstrate that multiple-transverse-mode operation affects VCSEL emission characteristics significantly. Specifically, it leads to the distortion of L-I curves of the orthogonally polarized components, degradation of spatial beam quality, increase of the spectral width, and modification of the mode-partition noise. It is also found that optical feedback leads to quasi-periodic oscillations and a corresponding change in the RIN spectrum.

Chapter 8

Summary

We have performed a detailed numerical study of the operation characteristics of VCSELs using the computer model described in Chapter 2 which incorporates spatial dependence of both the optical field and the carrier density. VCSEL characteristics are investigated under a variety of conditions including CW operation, gain-switched operation, optical feedback, and optical injection conditions. Both single-mode and two-mode operations have been studied, and the roles of carrier diffusion, spatial hole-burning, and multimode operation are assessed under different operating conditions.

In Chapter 3, we have studied the static and noise characteristics under solitary operation. We find that contact geometry, spatial hole-burning, and diffusion affect CW operation significantly, since transverse-mode characteristics depends critically on the overlap between the spatial distributions of the carrier density and the transverse modes. It is found that multimode operation can be somewhat controlled by choosing an appropriate contact geometry, since the contact shape and size determines the location where the carriers are injected. Spatial hole-burning at locations where different modes overlap leads to intermodal coupling and mode competition, which affect the L-I characteristics significantly. On the other hand, diffusion reduces strong mode competition by partly refilling the spatial holes. We have also investigated the effects of different transverse modes on the mode-partition noise in VCSELs by using different contact geometries. For a ring contact, mode-partition noise similar to that of edge-emitting lasers is observed. In contrast, for a wide disc contact, mode-partition noise is significantly reduced because of reduced carrier competition resulting from a smaller spatial overlap of the two transverse modes excited.

In Chapter 4, we have studied VCSEL performance under gain-switched operation. The effects investigated include modulation current and frequency, carrier diffusion, contact geometry, and multimode

operation. It is found that output pulse characteristics depend critically on the modulation conditions. In particular, there exists an optimal modulation index J_m/J_{th} for which the pulse width is minimum. Typical pulse widths are about 6 ps for the device parameters shown in Table 2.1. The optimal modulation condition is found to be affected by the modulation frequency and contact geometry. Specifically, the disc-contact area is shown to have a significant effect on gain-switching characteristics. Spatial holes in the carrier profile are responsible for the deterioration of device performance. With a disc-contact radius of smaller than $2\ \mu\text{m}$, spatial holes are eliminated. However, we find that the shortest pulses are obtained for disc-contact radii of $1\text{--}2\ \mu\text{m}$, the range that corresponds to maximum overlap between the spatial distributions of the lasing mode and the carrier density. We have also investigated two-mode gain-switching operation with a disc contact of $4\text{-}\mu\text{m}$ radius. Anti-correlated periodic oscillations are observed for all values of J_m/J_{th} investigated, and mode competition induced through spatial hole-burning leads to quite interesting nonlinear dynamics. This behavior is a consequence of spatio-temporal coupling.

In Chapter 5, we have investigated the effect of optical feedback on static and dynamic characteristics of VCSELs under both single-mode and two-mode operations. For a short external cavity, the mode power varies with the external-cavity length on a wavelength scale due to constructive and destructive interference effects introduced by the feedback field. For single-mode operation, the direction of power change is completely determined by the feedback phase. However, for the two-mode case, optical feedback enhances the effects of transverse-mode competition so that the magnitude and direction of power variations are significantly affected. In particular, the magnitude of the change in power can be so large that one transverse mode is completely suppressed. For a long external cavity, we have explored the change in the laser dynamics and RIN associated with feedback. It is found that feedback dynamics for two-mode operation is dependent on the strength of mode competition induced by spatial hole-burning. For two modes whose spatial profiles overlap partially, the two modes maintain some degree of independence, and weak mode competition leads to period-doubling behavior and an earlier onset of chaos. In contrast, for two modes whose spatial profiles overlap significantly, strong coupling between the two modes results in reduced sensitivity towards feedback together with a delay in the onset of chaos. We also find that the onset of self-pulsations and chaos are responsible for the RIN enhancement observed.

In Chapter 6, we have studied the static and dynamic characteristics of an optically injected VCSEL over a wide range of frequency detunings and injection powers. Operation characteristics are found to be affected considerably by the strength of intermodal coupling. Our results show that strong intermodal

coupling reduces the sensitivity of VCSELs towards external injection, in terms of both static (locking) and dynamic (non-locking) behaviors. Specifically, it is found that strong intermodal coupling shifts the locking region up to higher injection powers. Inside the locking region, power enhancement of one mode due to injection effects results in simultaneous power reduction of the other mode. In particular, one mode can be completely suppressed depending on the strength of spatial hole-burning and the injected power. Much lower quenching powers (< -10 dB) are required for the strong coupling case due to mode competition. Outside the locking region, the results show that the dynamics of different modes are correlated through intermodal coupling. Qualitatively different dynamics are observed inside the non-locking region and unstable locking region.

In Chapter 7, we have reported results which are obtained from experiments performed on a VCSEL. Our results show that multiple-transverse-mode operation affects device characteristics significantly. Specifically, it results in the distortion of L-I characteristics of the orthogonally polarized components, degradation of spatial beam quality, increase of the spectral width, and modification of the mode-partition noise. Results also indicate that optical feedback leads to quasi-periodic oscillations and a change in the RIN spectrum.

Bibliography

- [1] H. Soda, K. Iga, C. Kitahara, and Y. Suematsu, "GaInAsP/InP surface emitting injection lasers," *Jpn. J. Appl. Phys.* **18**, 2329-2330 (1979)
- [2] J.L. Jewell, A. Scherer, S.L. McCall, Y.H. Lee, S. Walker, J.P. Harbison, and L.T. Florez, "Low-threshold, electrically pumped vertical-cavity surface-emitting microlasers," *Electron. Lett.* **25**, 1123-1124 (1989)
- [3] C.J. Chang-Hasnain, J.P. Harbison, C.E. Zah, M.W. Maeda, L.T. Florez, N.G. Stoffel, and T.P. Lee, "Multiple wavelength tunable surface-emitting laser arrays," *IEEE J. Quantum Electron.* **27**, 1386-1376 (1991)
- [4] D.B. Young, J.W. Scott, F.H. Peters, M.G. Peters, M.L. Majewski, B.J. Thibeault, S.W. Corzine, and L.A. Coldren, "Enhanced performance of offset-gain high-barrier vertical-cavity surface-emitting lasers," *IEEE J. Quantum Electron.* **29**, 2013-2022 (1993)
- [5] K.L. Lear, S.P. Kilcoyne, and S.A. Chalmers, "High power conversion efficiencies and scaling issues for multimode vertical-cavity top-surface-emitting lasers," *Photon. Technol. Lett.* **6**, 778-781 (1994)
- [6] Y.J. Yang, T.G. Dziura, T. Bardin, S.C. Wang, and R. Fernandez, "Continuous wave single transverse mode vertical-cavity surface-emitting lasers fabricated by helium implantation and zinc diffusion," *Electron. Lett.* **28**, 274-276 (1992)
- [7] K.L. Lear, K.D. Choquette, R.P. Schneider, S.P. Kilcoyne, and K.M. Geib, "Selectively oxidized vertical-cavity surface-emitting lasers with 50% power conversion efficiency," *Electron. Lett.* **31**, 208-209 (1995)

- [8] Y. Hayashi, T. Mukaiharu, N. Hatori, N. Ohnoli, A. Matsutani, F. Koyama, and K. Iga, "A record low threshold index-confined InGaAs/AlGaAs vertical-cavity surface-emitting laser with a native oxide confinement structure," *Electron. Lett.* **31**, 560-561 (1995)
- [9] T.E. Sale, J.S. Roberts, J. Woodhead, J.P.R. David, and P.N. Robson, "Room-temperature visible (613–713 nm) all-AlGaAs vertical-cavity surface-emitting lasers," *Photon. Technol. Lett.* **8**, 473-475 (1996)
- [10] S. Uchiyama, N. Yokouchi, and T. Ninomiya, "Continuous-wave operation up to 36 degrees Celsius of 1.3- μ m GaInAsP-IP vertical-cavity surface-emitting lasers," *Photon. Technol. Lett.* **9**, 141-142 (1997)
- [11] D.I. Babic, K. Streubel, R.P. Mirin, N.M. Margalit, J.E. Bowers, E.L. Hu, D.E. Mars, Long Yang, and K. Carey, "Room-temperature continuous operation of 1.54- μ m vertical-cavity lasers," *Photon. Technol. Lett.* **7**, 1225-1227 (1995)
- [12] C.J. Chang-Hasnain, in *Semiconductor lasers: past, present and future*, G.P. Agrawal, Ed., AIP Press, Woodbury, New York, 1995, Chapter 5
- [13] D.M. Kuchta, J. Gamelin, J.D. Walker, J. Lin, K.Y. Lau and J.S. Smith, "Relative intensity noise of vertical cavity surface emitting lasers," *Appl. Phys. Lett.* **62**, 1194-1196 (1993)
- [14] F. Koyama, "Intensity noise and polarization stability of GaAlAs-GaAs surface-emitting lasers," *IEEE J. Quantum Electron.* **27**, 1410-1416 (1991)
- [15] L. Raddatz, I.H. White, K.H. Hahn, M.R. Tan and S.Y. Wang, "Noise performance of multimode vertical cavity surface emitting lasers," *Electron. Lett.* **30**, 1991-1992 (1994)
- [16] M.S. Wu, L.A. Buckman, G.S. Li, K.Y. Lau and C.J. Chang-Hasnain, "Polarization induced enhancement of relative intensity noise and modulation distortion in vertical cavity surface emitting lasers," *IEEE 14th Int. Semiconductor Laser Conf.*, 145-146 (1994)
- [17] J.L. Jewell, Y.H. Lee, A. Scherer, S.L. McCall, N.A. Olsson, J. Harbison, and L.T. Florez. "Surface-emitting microlasers for photonic switching and interchip connections," *Opt. Eng.* **29**, 210-214 (1990)

- [18] D. Tauber, G. Wang, R.S. Geels, J.E. Bowers, and L.A. Coldren, "Large and small signal dynamics of vertical-cavity surface-emitting lasers," *Appl. Phys. Lett.* **62**, 325-327 (1993)
- [19] U. Fiedler, G. Reiner, P. Schnitzer, and K.J. Ebeling, "Top surface-emitting laser diodes for 10-Gb/s data transmission," *Photon. Technol. Lett.* **8**, 746-748 (1996)
- [20] L.G. Melcer, J.R. Karin, R. Nagarajan, and J.E. Bowers, "Picosecond dynamics of optical gain switching in vertical-cavity surface emitting lasers," *IEEE J. Quantum Electron.* **27**, 1417-1425 (1991)
- [21] J.M. Wiesenfeld, G. Hasnain, J.S. Perino, J.D. Wynn, R.E. Leibenguth, and Y.H. Wang, "Gain-switched GaAs vertical-cavity surface-emitting lasers," *IEEE J. Quantum Electron.* **29**, 1996-2005 (1993)
- [22] P. Pepeljugoski, J. Lin, J. Gamelin, M. Hong, and K.Y. Lau, "Ultralow timing jitter in electrically gain-switched vertical cavity surface emitting lasers," *Appl. Phys. Lett.* **62**, 1588-1590 (1993)
- [23] R. Lang, "Injection locking properties of a semiconductor laser," *IEEE J. Quantum Electron.* **18**, 976-983 (1982)
- [24] H. Li, T.L. Lucas, J.G. McInerney, M.W. Wright and R.A. Morgan, "Injection locking dynamics of vertical cavity semiconductor lasers under conventional and phase conjugate injection," *IEEE J. Quantum Electron.* **32**, 227-235 (1996)
- [25] Z.G. Pan, S. Jiang and M. Dagenais, "Optical injection induced polarization bistability in vertical-cavity surface-emitting lasers," *Appl. Phys. Lett.* **63**, 2999-3001 (1993)
- [26] C.J. Chang-Hasnain, J.P. Harbison, G. Hasnain, A.C. Von Lehmen, L.T. Florez and N.G. Stoffel, "Dynamic, polarization and transverse mode characteristics of vertical-cavity surface-emitting lasers," *IEEE J. Quantum Electron.* **27**, 1402-1408 (1991)
- [27] C.J. Chang-Hasnain, M. Orenstein, A. Von Lehmen, L.T. Florez, J.P. Harbison and N.G. Stoffel, "Transverse Mode Characteristics of vertical-cavity surface-emitting lasers," *Appl. Phys. Lett.* **67**, 218-220 (1990)

- [28] J.M. Catchmark, L.E. Rogers, R.A. Morgan, M.T. Asom, G.D. Guth, and D.N. Christodoulides, "Optical characteristics of multitransverse-mode vertical-cavity top surface-emitting laser arrays," *IEEE J. Quantum Electron.* **32**, 986-995 (1996)
- [29] G.C. Wilson, D.M. Kuchta, J.D. Walker, and J.S. Smith, "Spatial hole-burning and self-focusing in vertical-cavity surface-emitting laser diodes," *Appl. Phys. Lett.* **64**, 542-544 (1994)
- [30] D. Vakhshoori, J.D. Wynn and G.J. Zyzik, "Top-surface emitting lasers with 1.9V threshold voltage and the effect of spatial hole burning on their transverse mode operation and efficiencies," *Appl. Phys. Lett.* **62**, 1448-1450 (1993)
- [31] A. Valle, J. Sarma and K.A. Shore, "Spatial holeburning effects on the dynamics of vertical cavity surface-emitting laser diodes," *IEEE J. Quantum Electron.* **31**, 1423-1431 (1995)
- [32] C.H. Chong and J. Sarma, "Lasing mode selection in vertical-cavity surface-emitting laser diodes," *IEEE Photon. Tech. Lett.* **5**, 761-764 (1993)
- [33] A. Valle, J. Sarma and K. Shore, "Dynamics of transverse mode competition in vertical-cavity surface-emitting laser diodes," *Opt. Comm.* **115**, 297-302 (1995)
- [34] O. Buccafusca, J.L.A. Chilla, J.J. Rocca, C. Wilmsen and S. Feld, "Ultrahigh frequency oscillations and multimode dynamics in vertical cavity surface emitting lasers," *Appl. Phys. Lett.* **67**, 185-187 (1995)
- [35] O. Buccafusca, J.L.A. Chilla, J.J. Rocca, S. Feld, and C. Wilmsen, "Transverse mode dynamics in vertical cavity surface emitting lasers excited by fast electrical pulses," *Appl. Phys. Lett.* **68** 590-592, (1996)
- [36] R.A. Morgan, G.D. Guth, M.W. Focht, M.T. Asom, K. Kojima, L.E. Rogers, and S.E. Callis, "Transverse mode control of vertical-cavity top-surface-emitting lasers," *IEEE Photon. Technol. Lett.* **4**, 374-377 (1993)
- [37] Y.A. Wu, G.S. Li, R.F. Nabiev, K.D. Choquette, C. Caneau, and C.J. Chang-Hasnain, "Single-mode, passive antiguide vertical cavity surface emitting laser," *IEEE J. on Selected Topics in Quantum Electron.* **1**, 629-637 (1995)

- [38] Y.G. Zhao and J.G. McInerney, "Transverse mode control of vertical-cavity surface-emitting lasers," *IEEE J. Quantum Electron.* **32**, 1950-1958 (1996)
- [39] Y. Kaneko, T. Tamanuki, M. Katoh, H. Maekawa, F. Koyama, and K. Iga, "Transverse-mode characteristics of InGaAs/GaAs vertical-cavity surface-emitting lasers considering gain offset," *Jpn. J. Appl. Phys.* **32**, 1612-1614 (1993)
- [40] S.F. Yu and C.W. Lo, "Influence of transverse modes on dynamic response of vertical-cavity surface-emitting lasers," *IEE Proc-Optoelectron.* **143**, 189-194 (1996)
- [41] T.E. Sale, *Vertical-cavity Surface-emitting Lasers*, Wiley, New York, 1995
- [42] T. Mukaihara, F. Koyama, and K. Iga, "Stress effect for polarization control of surface emitting lasers," *Electron. Lett.* **28**, 555-556 (1992)
- [43] D. Sun, E. Towe, P.H. Ostdiek, J.W. Grantham, and G.J. Vansuch, "Polarization control of vertical-cavity surface-emitting lasers through use of an anisotropic gain distribution in (110)-oriented strained quantum-well structures," *IEEE J. on Selected Topics in Quantum Electron.* **1**, 674-680 (1995)
- [44] K.D. Choquette, R.P. Schneider, K.L. Lear, and R.E. Leibenguth, "Gain-dependent polarization properties of vertical-cavity lasers," *J. Selected Topics in Quantum Electron.* **1**, 661-666 (1995)
- [45] H.M. Chen, K. Tai, K.F. Huang, Y.H. Kao and J.D. Wynn, "Instability in SEL due to external optical feedback," *J. Appl. Phys.* **73**, 16-20 (1993)
- [46] J.P. Zhang, "Numerical simulation for vertical-cavity surface-emitting laser with external optical feedback," *Microwave Opt. Tech. Lett.* **7**, 359-361 (1994)
- [47] Y.C. Chong and Y.H. Lee, "Spectral characteristics of vertical-cavity surface-emitting laser with external optical feedback," *IEEE Photon. Tech. Lett.* **3**, 597-599 (1991)
- [48] M.A. Hadley, G.C. Wilson, K.Y. Lau and J.S. Smith, "High single-transverse-mode output from external-cavity surface-emitting laser diodes," *Appl. Phys. Lett.* **63**, 1607-1609 (1993)
- [49] G.C. Wilson, M.A. Hadley and K.Y. Lau, "High single-mode output power from compact external cavity microcavity surface-emitting laser diodes," *Appl. Phys. Lett.* **63**, 3265-3267 (1993)

- [50] J. Dellunde, A. Valle, and K.A. Shore, "Transverse-mode selection in external-cavity vertical-cavity surface-emitting laser diodes," *J. Opt. Soc. Am. B* **13**, 2477-2483 (1997)
- [51] U. Fiedler, "Design of VCSEL's for feedback insensitive data transmission and external cavity active mode-locking," *IEEE J. Selected Topics in Quantum Electron.* **1**, 442-449 (1995)
- [52] K.P. Ho, J.D. Walker and J.M. Kahn, "External optical feedback effects on intensity noise of vertical-cavity surface-emitting lasers," *IEEE J. Quantum Electron.* **5**, 892-895 (1993)
- [53] J.W. Scott, S.W. Corzine, D.B. Young, and L.A. Coldren, "Modeling the current to light characteristics of index-guided vertical-cavity surface-emitting lasers," *Appl. Phys. Lett.* **62**, 1050-1052 (1993)
- [54] G.R. Hadley, K.L. Lear, M.E. Warren, K.D. Choquette, J.W. Scott, and S.W. Corzine, "Comprehensive numerical modeling of vertical-cavity surface-emitting lasers," *IEEE J. Quantum Electron.* **32**, 607-616 (1996)
- [55] L. Thode, G. Csanak, R. Hotchkiss, C. Snell, and M. Campbell, "Time-dependent model for vertical-cavity surface-emitting laser," *Proceedings of the SPIE* **2399**, 328-359 (1995)
- [56] S.F. Yu, "Dynamic behavior of vertical-cavity surface-emitting lasers," *IEEE J. Quantum Electron.* **32**, 1168-1179 (1996)
- [57] S.F. Yu, W.N. Wong, P. Shum, and E.H. Li, "Theoretical analysis of modulation response and second-harmonic distortion in vertical-cavity surface-emitting lasers," *IEEE J. Quantum Electron.* **32**, 2139-2147 (1996)
- [58] S. Ramo, J. Whinnery, and T. Van Duzer, *Fields and waves in communication electronics*, 3rd edition, New York, Wiley (1994)
- [59] G.P. Agrawal and N.K. Dutta, *Semiconductor lasers*, 2nd edition, Van Nostrand Reinhold (1993), Chap. 6
- [60] J.A. Buck, *Fundamentals of Optical Fibers*, Wiley, New York, 1995
- [61] M. Yamada, "Transverse and longitudinal mode control in semiconductor injection lasers," *IEEE J. Quantum Electron.* **15**, 1365-1379 (1983)

- [62] M. Lax, and W.H. Louisell, "Quantum noise XII density-operator treatment of field and population fluctuations," *Phys. Rev.* **185**, 568-591 (1969)
- [63] N.G. van Kampen, *Stochastic processes in physics and chemistry* (Amsterdam: North-Holland) (1981)
- [64] K.Y. Lau, "Gain switching of semiconductor injection lasers," *Appl. Phys. Lett.* **52**, 257-259 (1988)
- [65] W. F. Ngai and H.F. Liu, "Observation of period doubling, and period quadrupling in a directly modulated 1.55 μm InGaP distributed feedback laser diode," *Appl. Phys. Lett.* **62**, 2611-2613 (1993)
- [66] G.P. Agrawal, "Effect of gain nonlinearities on period doubling and chaos in directly modulated semiconductor lasers," *Appl. Phys. Lett.* **49**, 1013-1015 (1986)
- [67] R. Lang and K. Kobayashi, "External optical feedback effects on semiconductor injection laser properties," *IEEE J. Quantum Electron.* **16**, 347-355 (1980)
- [68] A.T. Ryan, G.P. Agrawal, G.R. Gray and E.C. Cage, "Optical-feedback-induced chaos and its control in multimode semiconductor lasers," *IEEE J. Quantum Electron.* **30**, 668-679 (1994)
- [69] G.H.M. van Tartwijk, G. Muijres, D. Lenstra, M.P. van Exter, and J.P. Woerdman, "Semiconductor laser beyond the locking range of optical injection," *Electron. Lett.* **29**, 137-138 (1993)
- [70] T.B. Simpson, J.M. Liu, A. Gavrielides, V. Kovanis, and P.M. Alsing, "Period-doubling cascades and chaos in semiconductor lasers subject to optical injection," *Phys. Rev. A* **51**, 4181-4185 (1995)
- [71] Y. Mori, J. Shibata and T. Kajiwar, "Optical polarization bistability in TM wave injected semiconductor lasers," *IEEE J. Quantum Electron.* **25**, 265-272 (1989)
- [72] G.H.M. van Tartwijk and D. Lenstra, "Semiconductor lasers with optical injection and feedback," *Quantum Semiclass. Opt.* **7**, 87-143 (1995)
- [73] A.B. Pippard, "Response and stability: an introduction to the physical theory," Cambridge University Press, Cambridge, 25-30 (1985)